

2

AD-A236 743

REPORT



Form Approved
OMB No. 0704-0188

Public reporting burden for this collection of information is estimated to average 1 hour per response, including the time for reviewing instructions, searching existing data sources, gathering and maintaining the data needed, reviewing the collection of information, and completing and reviewing the collection of information. Send comments regarding this burden estimate or any other aspect of this collection of information, including suggestions for reducing this burden, to Washington Headquarters Services, Directorate for Information Operations and Reports, 1215 Jefferson Davis Highway, Suite 1204, Arlington, VA 22202-4302, and to the Office of Management and Budget, Paperwork Reduction Project (0704-0188), Washington, DC 20503.

1. AGENCY USE ONLY (Leave blank)		2. REPORT DATE June 1, 1991	3. REPORT TYPE AND DATES COVERED Final 8/1/84 - 3/31/89
4. TITLE AND SUBTITLE Physics and Chemistry of Small Scale Structures for Modern Devices.			5. FUNDING NUMBERS Contract N00014-84-K-0501
6. AUTHOR(S) T. C. McGill			8. PERFORMING ORGANIZATION REPORT NUMBER N/A
7. PERFORMING ORGANIZATION NAME(S) AND ADDRESS(ES) Dept. of Applied Physics 128-95 California Institute of Technology Pasadena, CA 91125			
9. SPONSORING / MONITORING AGENCY NAME(S) AND ADDRESS(ES) Office of Naval Research			10. SPONSORING / MONITORING AGENCY REPORT NUMBER
11. SUPPLEMENTARY NOTES N/A			
12a. DISTRIBUTION / AVAILABILITY STATEMENT Available to public			12b. DISTRIBUTION CODE
13. ABSTRACT (Maximum 200 words) Under the support of this contract a number of major contributions were made to the development of nanostructures for microelectronics. Fundamental studies of growth have led to a better understanding of the role of strain in epitaxial layers grown on semiconductor substrates. The possibilities for growing superconductors on semiconductors and vice-versa have taken a major step forward with the successful growth of vanadium III silicon on silicon. The basic theory of tunnel devices including the role of phonons and self-consistency have been explored. New device structures based on the combination of III-V and II-VI semiconductors have also been examined.			
14. SUBJECT TERMS Growth of epitaxial layers, MBE, MOCVD, high-speed tunnel devices, electronic wave function, gallium arsenide/gallium aluminum arsenide, vanadium III silicon.			15. NUMBER OF PAGES 55
			16. PRICE CODE
17. SECURITY CLASSIFICATION OF REPORT Unclassified	18. SECURITY CLASSIFICATION OF THIS PAGE Unclassified	19. SECURITY CLASSIFICATION OF ABSTRACT Unclassified	20. LIMITATION OF ABSTRACT SAR

Accession For	
Final Report	<input checked="" type="checkbox"/>
Disc For	<input type="checkbox"/>
Unpublished	<input type="checkbox"/>
Justification	
by	
Distribution	
Availability Code	
Special	



A-1

FINAL REPORT

THE OFFICE OF NAVAL RESEARCH
 CONTRACT NO. N00014-84-K-0501

PHYSICS AND CHEMISTRY OF SMALL SCALE STRUCTURES FOR MODERN DEVICES

by

T.C. McGILL

THOMAS J. WATSON SR. LABORATORY OF APPLIED PHYSICS
 CALIFORNIA INSTITUTE OF TECHNOLOGY
 PASADENA, CALIFORNIA 91125
 (818) 356-4849

91-01894



INTRODUCTION

The development of new materials preparation techniques including molecular beam epitaxy and metal-organic chemical vapor deposition have made possible the design of materials at the atomic scale. These technological developments are making possible a whole new set of electronic concepts that are likely to be the key technologies for the 1990's and beyond. Research supported under this contract was aimed at addressing some of the key questions in this field.

One of the major applications of these new device preparation technologies is the production of electronic devices that are likely to be replacements for the standard transistors now employed in the period well beyond the turn of the century. One version of these is resonant tunneling devices in which electron waves incident on a double barrier structure are resonantly transmitted through a central quantum well. This phenomena leads to a negative resistance and is capable of producing bi-state electronic devices. Part of the research program here has been aimed at achieving that subject.

A second major issue that is addressed in this research program is the possibility for growing various materials combinations in molecular beam epitaxy or metal-organic chemical vapor deposition. Notably in this work we attack two major problems. One of them was a study of the role of strain in determining the quality of epitaxial layers grown in standard semiconductor systems. Historically, one of the major issues has been the role of strain in determining the compositional clustering of atoms in thin films grown by MBE or MOCVD. Other areas of intense interest in growth are the possibilities of growing heterostructures involving materials with very dissimilar electronic properties. One of the major efforts of this program was to attempt to combine superconductors and semiconductors.

Finally, one of the major applications for tunnel structures is in high speed. Hence one of the principal activities of any research program in this area is to attempt to make measurements of the high speed transient behavior of tunnel devices.

The major contributions in each one of these areas is outlined in the following sections. For completeness, copies of the publications are included in the appendices. One of the major outputs of any research program is the training of graduate students. A list of the graduate students trained into this program is included in a section just prior to the major concluding section.

MAJOR CONTRIBUTIONS

Tunnel Devices

Three major contributions were made under this program in the area of tunnel devices. We made the first self-consistent calculation of the electronic wave functions in gallium arsenide/gallium aluminum arsenide interfaces with relevance to tunnel devices. The major issue addressed in this effort was to obtain the proper wave functions at the interface for developing a better understanding of the potential profile and the character of the wave function just prior to tunneling in the tunneling device. None of the previous workers had actually carried out self-consistent calculations. We find that there are major modifications in the electronic wave function and in the potential due to self-consistency. The results of this research are presented in the paper included in Appendix 1.

One of the major issues in the theory of tunnel devices is proper prediction of the peak-to-valley ratio. Much of the theory to date predicts peak currents correctly but has great difficulty in predicting valley currents. Under the support of this program we carried out a study of the role of inelastic phonon scattering in determining valley currents. Basically, phonon scattering processes can effectively broaden the resonance in the tunnel structure and lead to an increase in the valley current. Theoretical studies based on the inclusion of optical phonons as well as acoustic phonons in this process have indicated that the phonon scattering mechanism can change the valley current by literally many orders of magnitude. The

details of this research are contained in the publication included as Appendix 2.

Another major issue in the development of tunnel devices is to come up with new materials combinations which can lead to better tunnel device performance. One possibility explored under the support of this program is the combination of III-V/II-VI heterojunctions. Notably systems such as gallium arsenide/zinc selenide and indium arsenide/zinc telluride are attractive for application in tunnel devices. In these systems the wide bandgap II-VI semiconductor zinc telluride or zinc selenide acts as a barrier layer replacing the III-V semiconductor that has been historically used as the barrier. The results of this theoretical study are contained in detail in the paper included as Appendix 3.

One of the major issues in the determination of the performance of tunnel devices and many other heterojunction-based electronic device structures is the value of the band offsets. Under the support of this program we carried out some of the first measurements in our new MBE esca system of the band offsets for the extremely well-studied gallium arsenide/gallium aluminum arsenide system. Because of the unique features of having an MBE connected to an esca facility we were able to study the commutivity of the band offset for the (100) structure which is the one that is predominantly used in making devices. The results of this effort are included in the publication in Appendix 4.

Another area of intense importance in the development of small device structures is the role of fluctuations. The atomistic nature of all the materials used in making these devices plus the importance of doping leads to an inherent role of fluctuations in all electronic devices of this type. One of the problems being treated under the support of this research activity has been the role of fluctuations. Notably we were interested in treating the percolation problem under finite size considerations. The results of this research effort are included in Appendix 5.

Yet another of the other major areas of interest in tunnel devices is their high-speed performance. Tunneling times are thought to be measured

in the picosecond range for these device structures. Under the support of this program we carried out some of the first measurements of the tunneling times for the high-speed tunnel devices. Using a novel photoluminescence technique which measures the tunneling of electrons and holes out of the central well, we were able to explore the transient behavior of tunnel devices. The major results of this study are included in a publication which has been attached as Appendix 6.

Growth

Under the support provided by this contract we carried out two major studies of growth. First, we carried out a theoretical study of the role of strain in producing phase separation in epitaxial layers. In this pioneering effort on our part which has now grown into a full blown activity by a number of key investigators, we examined the possibilities for strain induced phase separation in alloy layers grown by the modern growth techniques. While we found that such a driving mechanism would not be important in the gallium arsenide/gallium aluminum arsenide system, for other systems it could lead to substantial phase separation. The details of this theoretical work are included in Appendix 7, which includes the published paper.

One of the major areas of intense interest is the possibility for growing superconducting materials on semiconductors and then growing semiconductor materials back. Successful development of this materials technology could lead to a whole host of new device possibilities. For example, highly controlled Josephson junctions could be grown in this method. The possibility of exploring semiconductor-enhanced transition temperatures in superconductors would also be explorable with this method. The incorporation of superconductors in a natural epitaxial way with semiconductors could lead to a whole new set of device concepts combining the importance of semiconductor electronic properties with some of the novel aspects of superconductors. One of the most attractive possibilities for this is the growth of vanadium III silicon on silicon. Theoretical studies previously supported by the Office of Naval Research have indicated that this particular system has a good lattice match between vanadium III silicon and the silicon substrates. Hence one might hope to be able to grow this

system in an epitaxial fashion. However, there are some inherent difficulties. Notably the desire to grow a metal-rich, that is vanadium-rich, phase on top of a semiconductor or vice-versa in a very thin layer suggests some difficulties.

Under research provided by this contract we were able to demonstrate the growth of vanadium III silicon on silicon substrates. During this study we were able to obtain thin layers of vanadium III silicon on silicon substrates for superconducting transition temperatures close to those of bulk vanadium III silicon. The various parameters governing the growth of these superconducting layers on semiconductors were explored. While the materials to date have not been single crystal but have consisted of relatively small grain polycrystal in vanadium III silicon, the success of growing a superconducting metal-rich on top of a semiconductor is a major step in the right direction. This set of experimental results is included in the papers in Appendices 8 and 9.

GRADUATE STUDENTS TRAINED INTO THIS RESEARCH PROGRAM

The support provided by this program made substantial contributions to the training of five Ph.D. students. Their names are Alice Bonnefoi, Wesley Boudeville, Matthew Johnson, Yasantha Rajakarunanayake and George Wu. Each of these students is continuing to make contributions in their own scientific environment.

CONCLUSIONS

Under the support of this contract a number of major contributions were made to the development of nanostructures for microelectronics. Fundamental studies of growth have led to a better understanding of the role of strain in epitaxial layers grown on semiconductor substrates. The possibilities for growing superconductors on semiconductors and vice-versa have taken a major step forward with the successful growth of vanadium III silicon on silicon. The basic theory of tunnel devices including the role of phonons and self-consistency has been explored. New device structures

based on the combination of III-V and II-VI semiconductors have also been examined.

Research provided under the support of this contract has made a substantial contribution to the development of microelectronics into the turn of the next century.

APPENDIX 1

Self-consistent solutions of electronic wave functions at GaAs-Al_xGa_{1-x}As interfaces

Y. Rajakarunanayake and T. C. McGill

California Institute of Technology, Pasadena, California 91125

(Received 23 March 1987; accepted 23 April 1987)

We report the first study of the self-consistent electronic wave functions at a heavily doped GaAs-Al_xGa_{1-x}As interface. The doping densities in the GaAs are between 10^{17} and 10^{19} cm⁻³. These doping densities are characteristic of tunnel structure devices. The Schrödinger equation is solved self-consistently in the Hartree approximation. Some of the more important results of our calculations include the fact that there is only a single subband level in the well for a wide range of biases. This level is also fairly loosely bound (bound by a few meV) in spite of the fact that the notch at the interface is on the order of a 100 meV. In accumulation layers, the potential at the interface is somewhat similar to the non-self-consistent one. However, in depletion layers the self-consistent potential can be substantially different from the one obtained in the Thomas-Fermi approximation.

I. INTRODUCTION

In this paper we have studied the self-consistent potential, and the associated electronic wave functions that exist at heavily doped GaAs-Al_xGa_{1-x}As interfaces. These interfaces occur very commonly in single-barrier, and double-barrier heterostructures made of GaAs and Al_xGa_{1-x}As.¹⁻³ For example, let us consider a single barrier structure which consists of GaAs electrodes and a Al_xGa_{1-x}As barrier. To describe the tunneling of electrons through this barrier, we have to study the response of GaAs electrons to an applied voltage bias. When the applied electric field is perpendicular to the interface, accumulation and depletion layers are formed at the interfaces of the barrier on either side. With the self-consistent theory developed here, we are able to account for band bending and the details of the screening charge near the interfaces. These self-consistent solutions given here are of major interest because band bending plays a major role in determining the tunneling current and other device properties.^{3-6,13}

The first part of this paper discusses the details of the Hartree model, and the important elements of self-consistent calculations. In the next part we discuss the results obtained for accumulation layers, and depletion layers separately. Two representative accumulation layers, and two depletion layers are studied in detail to explain the general features of the solutions. For each of these cases, the corresponding wave functions, carrier densities, and the potentials are included in the figures. One of the aims of this paper is to compare the merits of the Thomas-Fermi theory versus the self-consistent theory. Thus the corresponding Thomas-Fermi results are also discussed along with those of the self-consistent theory. The last section of this paper constitutes a brief summary of the major results.

II. DESCRIPTION OF THE MODEL

In our investigations, we have used the self-consistent Hartree model⁷⁻⁹ to treat the accumulation and depletion layers that are formed in GaAs-Al_xGa_{1-x}As heterostruc-

tures when a potential bias is applied. Right from the beginning, we can isolate the two interfaces of the barrier and study each side separately, since the coupling between the two sides is exponentially small as far as the electrostatics of the problem is concerned. Here the conduction band electrons of the heavily doped GaAs at the Γ point are allowed to rearrange themselves to provide the screening of the external electric field. The motion of these electrons are assumed to be described by a simple effective mass Schrödinger Hamiltonian. Since the Γ point of GaAs is isotropic, we can characterize the effective mass m^* by a simple scalar quantity.

In the Hartree approximation, each electron moves in the average electrostatic potential produced by all the other conduction electrons, and the uniform positive background due to the ionized donors. However, the forces acting on the electrons can be separated into two categories. The first category is the coulombic electrostatic forces that are accounted correctly by the Hartree term. The other category is the exchange and correlation forces that arise due to the statistics of spin $\frac{1}{2}$ Fermions. In principle these exchange terms have to be included in the Hamiltonian to correctly describe the motion of the electrons. However inclusion of these terms usually constitutes a many-body problem, and cannot be adequately described by an independent electron picture. The strength of the exchange-correlation force compared to the electrostatic force depends on the parameter r_s of the medium. Here r_s is the interelectronic spacing expressed in the units of the effective Bohr radius. Thus for heavily doped materials with high dielectric constants and low effective masses, we can argue that the exchange terms are subdominant. Fortunately, heavily doped GaAs has a small effective mass and a large dielectric constant, and thus we can be contented with only including the Hartree term of the potential in the Hamiltonian. The various approximate methods available for estimating these exchange and correlation potentials as functionals of the local-electron density, that go under the name of "density functional methods" will not be discussed here.¹² We have also ignored the electrostatic image forces that arise near the interface due to the difference in

the dielectric constants of the two materials.

In our model the $\text{GaAs-Al}_x\text{Ga}_{1-x}\text{As}$ interface is assumed to be sharp. This enables us to treat the potential seen by the conduction band electrons of GaAs near the interface as a simple potential step with the appropriate magnitude of the conduction-band offset. The band offsets that occur in our structures are usually about 200 meV. This corresponds to an $\text{Al}_x\text{Ga}_{1-x}\text{As}$ layer with a value of $x \approx 0.3$. We have also limited our attention to degenerately doped n -type GaAs electrons, at zero temperature. However a similar analysis can be performed on p -type semiconductors, and other direct gap materials, with only minor modifications to account for the finite temperatures. The effective mass of GaAs used is $m^* \approx 0.065m_e$, where m_e is the bare electronic mass. The effective mass of $\text{Al}_x\text{Ga}_{1-x}\text{As}$ used is $m^* \approx 0.092m_e$. The background material (filled-valence electrons and ion cores) is assumed to be passive except to provide the uniform dielectric constant of the medium. In GaAs $\epsilon \approx 13.1\epsilon_0$, where ϵ_0 is the permittivity of the vacuum. In $\text{Al}_x\text{Ga}_{1-x}\text{As}$ $\epsilon \approx 12.2\epsilon_0$.

The potential V is chosen to be zero far away from the interface, on the GaAs side. When the GaAs is attached to the negative electrode, electrons see an attractive potential, near the barrier. Thus an accumulation layer forms, and the potential is lowered below zero at the interface. However, when the GaAs is attached to the positive electrode, then a repulsive potential is formed at the barrier. In this case a depletion layer is formed and the potential is raised above zero near the barrier. We have chosen the z axis to be perpendicular to the interface. Thus, taking into account that there is no variation of the potential in the x - y plane, one can readily reduce this problem into a one-dimensional one. However, in matching the boundary conditions at the interface, the parallel component of the wave vector of each electron k_{\parallel} is assumed to be conserved across the interface. When solving the self-consistent problem in the accumulation region, one also has to consider the bound states that can occur in the potential well.

In a typical self-consistent iteration scheme, we start with a guess for the form of the potential, and solve the one-dimensional Schrödinger equation. From these solutions, we then compute the charge density due to all the other conduction electrons, and the positive background. Using the charge density computed in the last step, we next solve the Poisson equation to obtain a new potential. The details of the various schemes used to achieve the convergence will not be discussed here.¹⁰ A simple-minded scheme that works with considerable success is to modify the input potential by feeding back a fraction of the difference between the output and the input potentials of the last iteration.⁸ We have found that an exponentially decaying potential with the appropriate Thomas-Fermi decay length works as a very good initial guess for starting the self-consistent iteration scheme.

In this section, we illustrate the solution of the Schrödinger equation in the effective mass approximation, for a guess Hartree potential $V(z)$. With the above assumptions, we can write the wave functions for this problem as $\psi(z)e^{ik_x x}e^{ik_y y}$. The resulting solutions, $\psi(z)$ are the set of envelope wave functions, in the z direction. The actual wave

functions are a product of these envelope functions, and the appropriate microscopic Bloch functions. We have measured the energy E_k of the electron also with respect to the zero of the potential. If we introduce $q = k_z$ to simplify the formulas, then we can write

$$E_k = \frac{\hbar^2}{2m^*} (k_x^2 + k_y^2) + \epsilon_q,$$

where

$$\epsilon_q = \frac{\hbar^2 q^2}{2m^*} = \frac{\hbar^2 k_z^2}{2m^*}.$$

Substituting these relations into the three-dimensional Schrödinger equation gives us the familiar one-dimensional Schrödinger equation

$$-\frac{\hbar^2}{2m^*} \frac{d^2}{dz^2} \psi_q(z) + V(z)\psi_q(z) = \epsilon_q \psi_q(z).$$

When we solve this equation for positive energy by the above-described method, we consider incident waves impinging on the barrier from infinity, that reflect back from the barrier with only a negligible transmitted component. The boundary conditions are such that the exponentially increasing solution in the barrier is discarded. At the interface, we have also matched the boundary conditions that the current and the amplitude of each wave function be the same on both sides of the interface. The incident and the reflected waves interact to give solutions of the form which have the asymptotic forms, $\psi_q \sim \sin^2(qz - \eta)$, far from the barrier. The normalization of these continuum states have to be done with considerable care. Thus we introduce a macroscopic normalization length L , and a cross-sectional area A for the bulk of GaAs in the tunnel structure, and let $L \rightarrow \infty$ at a later point of the calculation. Then we choose

$$\psi_q(z) \sim \sqrt{2/L} \sin(qz - \eta)$$

as $z \rightarrow \infty$. Each state $\psi_q(z)$ we obtain is the only allowed linear combination of $+q$ and $-q$ states. So we have to sum only over one-half of the Fermi sphere with $q > 0$ to obtain the charge distribution. When there are bound states, we also normalize their wave functions $\psi_b(z)$ by the condition

$$\int_0^\infty \psi_b^*(z)\psi_b(z)dz = 1$$

for each bound state. Defining

$$\psi_q(z) = \sqrt{1/L} \varphi_q(z)$$

we can write the contribution to the charge density from the mobile states as

$$\rho_{\text{mob}}(z) = -\frac{2e}{(2\pi)^3} \int_0^{k_F} \pi(k_F^2 - q^2) \varphi_q^*(z) \varphi_q(z) dq$$

after dividing out by the factor A (cross-sectional area). Introducing $u = q/k_F$, we can write this expression as

$$\rho_{\text{mob}}(z) = -\frac{ek_F^3}{2\pi^2} \int_0^1 (1 - u^2) \varphi_u^*(z) \varphi_u(z) du.$$

Thus in the large z limit since the average value $\langle \varphi_u^*(z) \varphi_u(z) \rangle = 1$, we immediately recover the negative of the background doping density ρ_{bac} , giving a net charge density of zero at large distances away from the barrier. Here

$$\rho_{\text{bac}}(z) = \frac{ek_F^3}{3\pi^2}$$

for uniform doping. Similarly for bound states,

$$\rho_{\text{bou}}(z) = \frac{-ek_F^2}{2\pi} \sum_{i=1}^n \left(1 - \frac{E_i}{E_F}\right) \psi_b^*(z) \psi_b(z),$$

where n is the number of bound states in the well. Here E_i is the energy of the i th bound state, measured with respect to the zero of the potential. Thus the total charge on one side per unit area is

$$Q = \int_0^{L-\infty} [\rho_{\text{bou}}(z) + \rho_{\text{mob}}(z) + \rho_{\text{bac}}(z)] dz \\ = \int_0^{\infty} \rho_{\text{tot}}(z) dz.$$

Notice that it is proper to let $L \rightarrow \infty$ here because at this point of the calculation all our formulas are expressed in terms of quantities independent of L . This excess charge Q per unit area is negative in accumulation layers, and positive in depletion regions, and is in fact a boundary condition of the problem. Now in order to find the potential, the total charge density $\rho_{\text{tot}}(z)$ is plugged into the Poisson equation and integrated,

$$\frac{d^2}{dz^2} v(z) = \frac{e}{\epsilon} \rho_{\text{tot}}(z).$$

Using $v(z)$ is different from $V(z)$ if a self-consistent solution is not found. Thus we iterate this scheme with different guesses $V(z)$, until the self-consistency condition $V(z) \equiv v(z)$ is satisfied to the desired numerical accuracy.

III. RESULTS

A. Accumulation regions

One important feature that we discovered in our calculations was that there is only a single-bound state in the GaAs-Al_xGa_{1-x}As accumulation well for a wide range of applied biases. This observation was confirmed for doping densities ranging from 10^{17} to 10^{19} cm^{-3} , when the applied potential drop in the layer was between 50–100 meV. We have also found that this bound state is very loosely bound. The typical binding energies that we observed usually amounted to < 20 meV, and were about 5%–15% of the well depth. In retrospect, the evidence that there is only a single-bound state makes the application of the semiclassical theory to this problem invalid. The Thomas–Fermi semiclassical theory of screening is valid only in a regime where there are a large number of bound states in the well. This is the assumption that enables one to incorporate the extra bound electrons into the Fermi sea. The Wentzel–Kramers–Brillouin (WKB) approximation for eigenvalues predicts that the number of bound states n in a semiclassical well is given by

$$n \approx \int_0^{\infty} \sqrt{\frac{-2m^*V(z)}{\hbar^2}} dz.$$

Thus we see that the number of bound states $n \sim \sqrt{m^*}$. We could then argue that, in the GaAs system with a very small effective mass, one has to use a self-consistent model instead of the Thomas–Fermi model since the number of expected

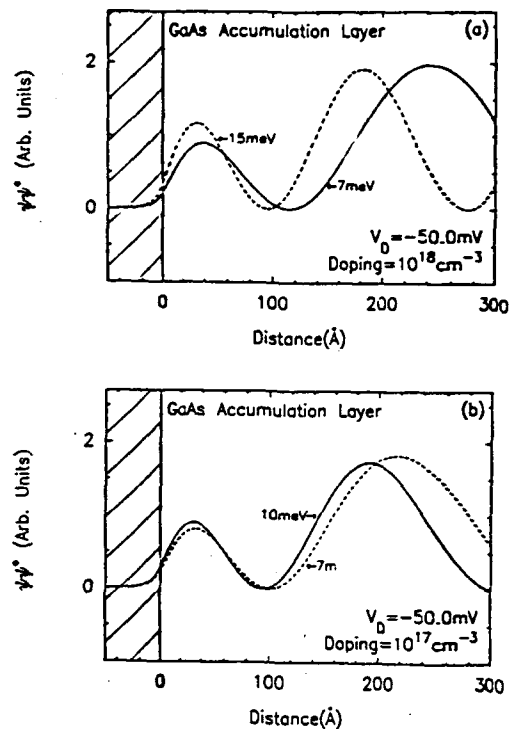


FIG. 1. Representative wave functions of accumulation layers. V_D is the potential drop in the GaAs layer. Note the decrease in the amplitude of $\psi\psi^*$ near the barrier. The respective energies of the electrons are indicated in meV. These curves are normalized to have an asymptotic form of $2 \sin^2(qz - \eta)$ far away from the barrier. The energies are measured with respect to the conduction band edge at infinity.

bound states in the well would be small. The discovery that $n = 1$ verifies this hypothesis and further indicates the importance of using a self-consistent model.

In Figs. 1(a) and 1(b), we have shown the accumulation layer self-consistent wave functions of two typical unbound states. The doping density is 10^{18} cm^{-3} in Fig. 1(a) and 10^{17} cm^{-3} in Fig. 1(b). These are the wave functions of the mobile states when a potential difference of V_D is allowed to drop in the GaAs layer. In the graphs, the normalization of these states is done in such a way that far away from the barrier the value of $\psi\psi^*$ approaches $2 \sin^2(qz - \eta)$. This normalization scheme allows us to compare the relative distortions that occur in each wave function as a function of energy and distance. In all these graphs, we definitely see a lack of negative charge near the barrier. The decaying exponential tail of these states gives rise to the tunneling current on the other side of the barrier. Thus it is very important to know the amplitude of these wave functions at the interface to accurately account for the tunneling current. We also see that, as the energy of the electrons is increased, their distortions from plane wave states is reduced. Thus the low lying conduction-band electronic states are the ones that are most distorted by the potential. Each solution here is constructed with an incoming wave and a reflected wave that is almost exactly in anti-phase with each other. (The phase difference would be exactly π if the barrier was infinite.) The definite phase difference between these two waves plays an important role in giving rise to a self-consistent charge density that

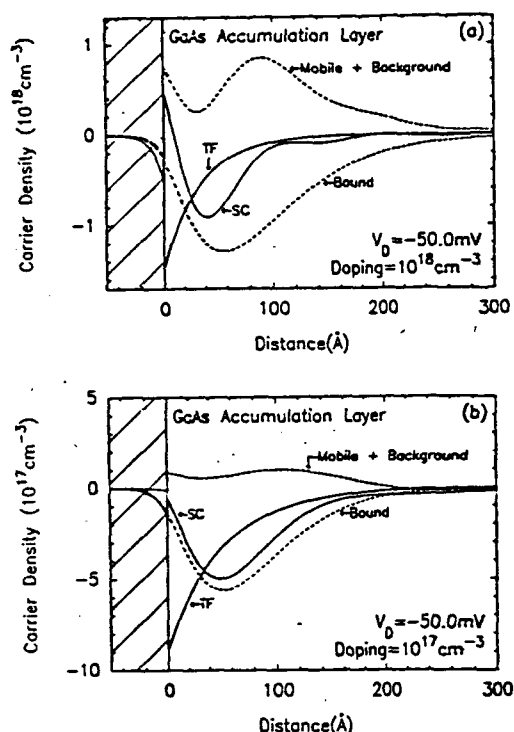


FIG. 2. Corresponding carrier densities obtained from the wave functions of Fig. 1. The self-consistent (SC) carrier density is the sum of the two curves mobile + background, and bound carrier densities. Notice that the self-consistent curve is very different from the Thomas-Fermi prediction. There is an excess of negative carriers, $5.7 \times 10^{11} \text{ cm}^{-2}$ in case (a) and $4.9 \times 10^{11} \text{ cm}^{-2}$ in case (b).

has Friedel type oscillations. However, when a scattering event occurs, the phase difference between these two waves would be randomized. Thus scattering would lead to an exponential decay in the Friedel oscillations of charge density. The length scale of this phenomenon can be estimated by assuming that scattering at low temperatures is predominantly charged impurity scattering. Realistically we can represent $\psi_i \psi_j^* \approx 1 - \cos(2qz - 2\eta)e^{-z/\lambda}$ in this case. Thus the definite phase relationship due to the reflection from the barrier would decay beyond a typical scattering length λ away from the barrier. A calculation we did with a crude model suggests that $\lambda \approx 1/k_F$. As these figures also illustrate, higher energy electrons penetrate more into the barrier, and thus would play a more important role in current conduction.

In Figs. 2(a) and 2(b) the dashed curves denoted by "bound" shows the bound state contribution to the charge density. All curves shown here correspond to the wave functions of Fig. 1. This bound charge arises from the two-dimensional subband of electrons that is bound in the GaAs accumulation well. This curve also resembles the shape of the wave function $\psi_i \psi_j^*$ of the bound state, since these two quantities are proportional to each other. The average spatial extent of these bound states is about 200–300 Å, and the peak of the bound state charge density occurs around 50–100 Å. These states show the expected trend that smaller binding energies results in states that have a larger spatial extent. The mobile state charge density plus the positive background

charge density is shown as the dashed curve denoted "mobile + background." Thus when we are sufficiently far away from the barrier, the mobile state charge density and the positive background cancels each other out to give a neutral medium. One noticeable feature of the mobile state charge density is that it is depleted near the interface. Thus the dashed curve has a net positive charge density due to the dominant positive background near the interface. The reason for this lack of charge very near the barrier can be understood in terms of the boundary conditions that dictate exponential decay of the wave function inside the barrier. Thus, in accumulation layers as well as in depletion layers, the interference of the incoming and the reflected waves produced only a small amplitude of the wave function at the barrier. This is one of the major contrasts to the Thomas-Fermi theory of screening which predicts a charge density that also dips down to a maximum negative value at the interface. Figures 2(a) and 2(b) clearly show this difference between the charge densities of the Thomas-Fermi and self-consistent models. However, another reason for the lack of charge is that the mobile states have to be orthogonal to the bound state in this region. Thus, the presence of the bound state in the well expels the mobile state electrons further away from the well, causing a lack of charge (a hole-like state) in the vicinity of the bound state. This is purely an effect due to the orthonormalization of the mobile states with respect to the bound state. Both these effects gives rise to depletion of the mobile electrons away from the well region even in the accumulation layer. These curves also undergo abrupt jumps as they cross the barrier and enter the undoped AlAs side. This is merely an artifact of the disappearance of the background positive charge as we go from the doped-GaAs side to the undoped-Al_xGa_{1-x}As side. We are also able to observe the fraction of the electron charge density that has penetrated inside the barrier in these curves.

The solid curve denoted SC (self-consistent) is the sum of the charge densities due to the positive background, bound electrons, and the mobile electrons, and is proportional to $\rho_{\text{tot}}(z)$. This is the charge density that is used in the Poisson equation to determine the self-consistent potential. Another interesting feature of the self-consistent charge density curve in Fig. 2(a) is that there is a dipole layer at the interface that has an extent of about 20 Å on each side. However, in the low doping case of Fig. 2(b), we do not see the formation of such a dipole layer. The excess negative charge that produces the dip in the potential mainly comes from the bound state. The bound state charge density in this region is 2–5 times the magnitude of the background doping in Fig. 2(b). By comparing Figs. 2(a) and 2(b) we also see that the relative importance of the bound state in accounting for the charge density is greater in the low density 10^{17} cm^{-3} case than in the high density 10^{18} cm^{-3} case.

In Figs. 3(a) and 3(b) we see the potentials corresponding to the wave functions of Fig. 1, and charge densities of Fig. 2. The exceptional closeness of the self-consistent potential and the Thomas-Fermi potential is indeed surprising, considering that the resulting charge densities are quite different. One way of understanding this is to say that, the presence of the bound state in the well alters the unbound states

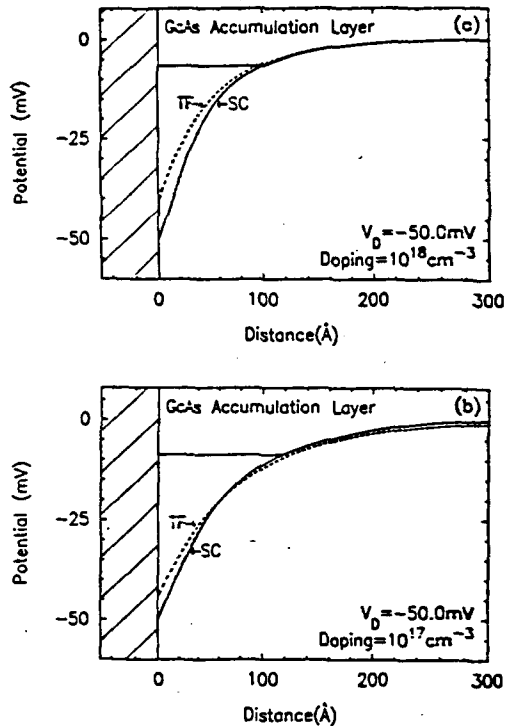


FIG. 3. Corresponding potential for Figs. 1 and 2 above. Notice the similarities between the Thomas-Fermi (TF) and self-consistent (SC) potentials, in the accumulation layers. The bound states are very loosely bound, with binding energies of 5.8 meV in (a) and 11.6 meV in (b). The applied potential drop is 50 mV in (a) and (b).

wave functions so as to produce an orthonormalization hole in the conduction band.^{7,11} This orthonormal hole-like state that exists in the conduction band moves in correlation with the bound state in response to external biases so as to make the total charge in the layer a continuous function of the applied bias. An analogous result has been proved by Kohn and Majumdar even in the event when the number of bound states in the well is variable. Thus, if a bound state vanishes at a certain strength of the applied bias, the significant fraction of charge that vanishes with it reappears in the conduction band as unbound charge. This corresponds to the rearrangement of charge that takes place due to the vanishing of the orthonormal hole. This enables one to lump the behavior of the bound state and the orthonormal holelike state from the continuum as a simple excess of charge that monotonically increases with the applied bias. This reduces to the same type of behavior that the Thomas-Fermi theory exhibits. This form of behavior, added to the constraint that the derivatives of the self-consistent and Thomas-Fermi potentials be equal at the interface (condition of same excess charge), would explain why the potentials look very similar. The position of the bound state that occurs in these wells is shown as the horizontal line segment in the figure.

B. Depletion regions

In Figs. 4(a) and 4(b) we see the wave functions of typical depletion layers. These are also normalized in the same way as in Figs. 1(a) and 1(b), to obtain their asymptotic forms of $2 \sin^2(qz - \eta)$ to the far left-hand side of the barrier. Results

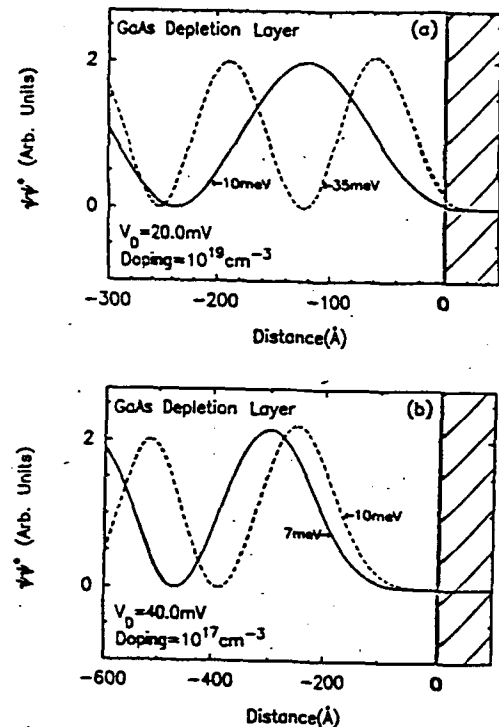


FIG. 4. Representative wave functions of depletion layers. V_D is the potential drop in the GaAs layer. Note that these states resemble plane waves in the depletion region, unlike in the accumulation region of Fig. 1. The respective energies of the electrons are indicated in meV. These curves are normalized to have an asymptotic form of $2 \sin^2(qz - \eta)$, far away from the barrier. The energies are measured with respect to the conduction band edge at infinity.

are presented for a doping density of 10^{19} cm^{-3} in Fig. 4(a) and 10^{17} cm^{-3} in Fig. 4(b). These electrons are reflected before they hit the barrier due to the repulsive self-consistent potential, that bends upwards in these layers. Thus the component of their wave functions that penetrate into the barrier is vastly reduced from those in the accumulation layers. We also see that these solutions are much less distorted from plane waves than in the case of the accumulation layers. This lack of distortion can be attributed to the lack of the bound state on this side of the barrier. Thus there is no distortion due to the orthonormalization requirement. One other noticeable result is that these waves actually undergo a slight accumulation in the first half wavelength away from the barrier. Again this leads to Friedel oscillations in the charge density.

Figures 5(a) and 5(b) show the corresponding charge densities of the wave functions of Fig. 4. The solid line SC is the self-consistent charge density which is the sum of the mobile electron contribution and the background positive ion contribution. In Fig. 5(a) a very small potential drop (20 meV) is applied with a deficient charge density of $9.0 \times 10^{11} \text{ cm}^{-2}$. On the other hand, in Fig. 5(b) a larger potential drop (40 meV) compared to the Fermi energy ($E_F = 12 \text{ meV}$) is applied with a deficient charge density of $2.2 \times 10^{11} \text{ cm}^{-2}$. Here we clearly see the long-range Friedel oscillations in the charge density that are characteristic of self-consistent calculations. They do not decay with an expo-

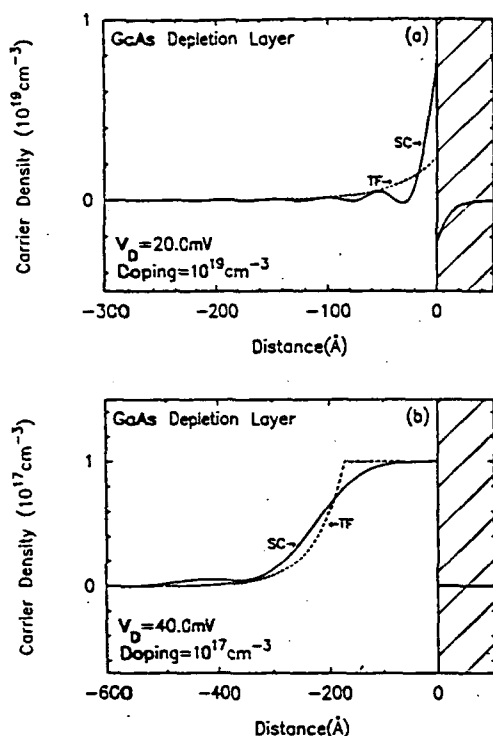


FIG. 5. Corresponding carrier densities obtained from the wave functions of Fig. 4. The self-consistent (SC) carrier density, and the Thomas-Fermi (TF) carrier density are quite different. Notice also the character of the long range oscillations of the self-consistent charge density. There is a deficiency of negative carriers, $9.0 \times 10^{11} \text{ cm}^{-2}$ in case (a) and $2.2 \times 10^{12} \text{ cm}^{-2}$ in case (b).

nential decay envelope although their amplitudes are small. These oscillations are dominant at high-doping density, small applied positive bias, and low temperatures. From a physical point of view the long-range oscillations in the screening charge arises from a sharp Fermi surface. The reason is that it is not possible to construct a smooth function free of oscillations with the restricted set of waves $q < k_F$. Thus, the screening charge will always exhibit oscillations approximately at $2k_F$, twice the cutoff frequency. The self-consistent screening charge also has a decay envelope that dies as an inverse power law, in contrast to the Thomas-Fermi result that predicts an exponential decay rate. However, at finite temperatures, these Friedel oscillations die out with an exponential factor proportional to $k_B T$. Thus, in real systems at finite temperature, the significance of these oscillations is negligible. The figures compare the self-consistent charge density with the Thomas-Fermi charge density. In the fully depleted region which occurs in Fig. 5(b), these two charge densities resemble one another. However, in the region beyond this, the difference is significant. This is mainly due to the difference in the long-range screening properties predicted by the two theories. There is also no apparent dipole layer on this side of the barrier unlike in the accumulation layers.

In Figs. 6(a) and 6(b) the self-consistent potential corresponding to the wave functions of Fig. 4, and the charge density of Fig. 5 is shown. The self-consistent potential and the Thomas-Fermi potential for the depletion layers can be significantly different from each other. The agreement

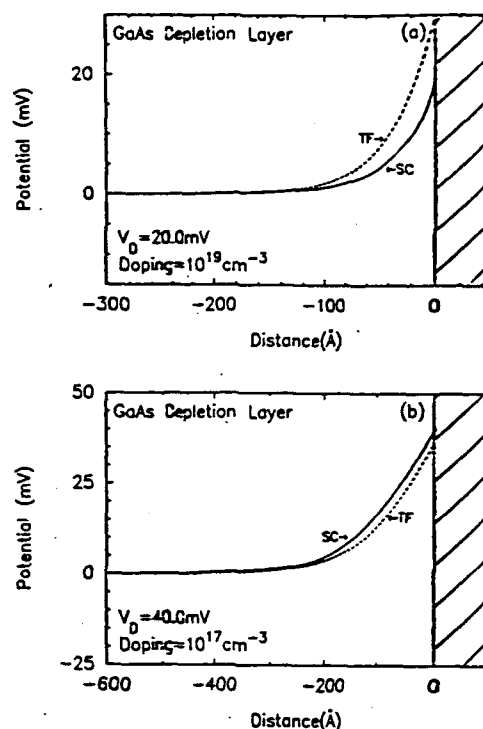


FIG. 6. Corresponding potential for Figs. 4 and 5 above. Note that in depletion layers, the self-consistent and Thomas-Fermi potentials can look very different from each other, as illustrated in case (a). The applied potential drop is 20 mV in (a) and 40 mV in (b).

between these two curves is worse in depletion layers than in accumulation layers. The reason for this difference is the assumption that the charge gets depleted in an exponential manner with a Thomas-Fermi decay length is not a valid one. In fact, the screening charge decays in the Hartree case with an envelope function of an inverse power law as discussed above. We also discovered that the Thomas-Fermi solution lies above the self-consistent solution in highly doped cases, and below the self-consistent solution in lightly doped cases.

IV. CONCLUSION

In conclusion, we see that the Thomas-Fermi theory is quite good at describing the potential in accumulation layers although it does a poor job at describing the charge densities. Our results indicate that by assuming the actual potential to be given by the Thomas-Fermi form, and solving for its eigenstates and eigenvalues one can obtain answers that are very close to the self-consistent ones. Thus, calculating the charge density from the wave functions of the Thomas-Fermi potential is quite adequate for describing the current through the device, and calculating the positions of the bound levels. Hence, one does not have to go through a full-blown numerical self-consistent calculation to obtain reasonable results for the accumulation layers. On the other hand, the potential and charge density of the depletion layers can be quite different from the self-consistent one, and has to be treated more carefully. The results of this study also indicates that there are no other electron levels in the well of the accumulation region, except for a single loosely bound level.

This implies that we can theoretically expect the turning off of the negative resistance in double barrier structures to be quite sharp. The reason for this is that the only level in the accumulation layer below the band edge lies very close to the band edge. We expect the self-consistent solutions given here to play an important role in the understanding of tunneling of electrons in double and single barrier heterostructures.

ACKNOWLEDGMENTS

We would like to acknowledge G. Y. Wu, T. K. Woodward, and D. H. Chow for valuable discussions. Parts of this work was supported by ONR under Contract No. N00014-84-K-0501.

¹R. Tsu and L. Esaki, *Appl. Phys. Lett.* **22**, 562 (1973).

²L. L. Chang, L. Esaki, and R. Tsu, *Appl. Phys. Lett.* **24**, 593 (1974).

³A. R. Bonnefoi, D. H. Chow, T. C. McGill, R. D. Burnham, and F. A. Ponce, *J. Vac. Sci. Technol. B* **4**, 988 (1986).

⁴A. R. Bonnefoi, D. H. Chow, and T. C. McGill, *J. Appl. Phys.* (to be published).

⁵H. Ohnishi, T. Inata, S. Muto, N. Yokoyama, and A. Sihbatomi, *Appl. Phys. Lett.* **49**, 1248 (1986).

⁶B. Ricco and M. Ya. Azbel, *Phys. Rev. B* **29**, 1970 (1984).

⁷G. A. Baraff and J. A. Appelbaum, *Phys. Rev. B* **5**, 475 (1972).

⁸T. Ando, A. B. Fowler, and F. Stern, *Rev. Mod. Phys.* **54**, 459 (1982).

⁹F. Stern and W. E. Howard, *Phys. Rev.* **163**, 816 (1967).

¹⁰F. Stern, *J. Comput. Phys.* **6**, 56 (1970).

¹¹W. Kohn and C. Majumdar, *Phys. Rev. A* **138**, 1617 (1965).

¹²T. Ando, *Phys. Rev. B* **13**, 3468 (1976).

¹³T. Ando, *J. Phys. Soc. Jpn.* **51**, 3893 (1982).

APPENDIX 2

Effects of barrier phonons on the tunneling current in a double-barrier structure

G. Y. Wu and T. C. McGill

T. J. Watson, Sr. Laboratory of Applied Physics, California Institute of Technology, Pasadena, California 91125

(Received 27 August 1987; revised manuscript received 20 May 1988)

The effects of AlAs acoustical and optical phonons on the tunneling current in an ideal GaAs-AlAs-GaAs-AlAs-GaAs structure are discussed. The transfer Hamiltonian method was extended to inelastic tunneling current in a double-barrier structure. It is found that the current off resonance in the Tsu-Esaki model could be enhanced by orders of magnitude by inelastic tunneling due to the coupling of electrons to barrier optical phonons. The contribution to the current due to the deformation-potential coupling of electrons to barrier acoustical phonons is found to be much less important.

Semiconductor heterostructures involving GaAs and AlAs have been the subject of both theoretical and experimental studies.¹⁻⁸ In GaAs-AlAs-GaAs-AlAs-GaAs structures, AlAs layers act as energy barriers while the middle GaAs layer acts as a well. Of particular interest are GaAs-AlAs-GaAs-AlAs-GaAs double-barrier structures which are specifically doped as *n-i-i-i-n*. Observations of resonant tunneling of electrons through double-barrier structures have been reported.¹ Tsu and Esaki² have theoretically treated the general case of electronic tunneling through multiple barriers. In the double-barrier case, resonant tunneling was shown by them to give rise to a current maximum (J_{peak}) at the voltage bias (V_q) where the Fermi sea of an electrode is aligned in energy with one of the quasibound states in the GaAs well. The current drops very rapidly at other voltages. Subsequent works have refined the theory for calculating the barrier transmission (T) and current-voltage (J - V_q) characteristics.³⁻⁶ Typically, the peak current they calculated agrees with the measured value. However, the measured valley current is greater than the theoretical value by at least 1 order of magnitude. Recently, Frensley has employed a transport theory approach which includes losses.⁷ However, all of these theories only consider elastic tunneling. On the other hand, Tsu and Dohler⁸ have considered inelastic tunneling assisted by the well phonons. In a recent study of GaAs-AlAs-GaAs structures, Collins, Lambe, and McGill⁹ reported the observation of inelastic tunneling of electrons. In such tunneling, the excitation of AlAs phonons could take away finite amount of energy and momentum from the tunneling electron. Hence, the total energy and the transverse momentum of the tunneling electron are no longer conserved. As we shall show, they could enhance the current off resonance by orders of magnitude in the Tsu-Esaki model. This suggests the importance of the inclusion of inelastic tunneling assisted by barrier phonons in calculations such as the self-consistent analysis of Onishi *et al.*⁶

Here, we present the first theoretical study of the effects on the tunneling current in a double-barrier structure due to the electron interaction with barrier phonons. The transfer Hamiltonian method proposed by Bardeen¹⁰ originally for the treatment of the tunneling of electrons through a single-barrier structure is extended to calculate

phonon-induced inelastic tunneling in a double-barrier structure. For illustration, we shall consider the zero temperature case where only phonon emission is possible. In this case with proper approximations, we obtain analytical expressions which shed some light on the important effects of inelastic tunneling. These effects change I - V characteristics for a double-barrier structure.

We treat a standard double barrier structure consisting of a layer of GaAs followed by a barrier of $\text{Ga}_{1-x}\text{Al}_x\text{As}$ followed by a well of GaAs followed by a second barrier of $\text{Ga}_{1-x}\text{Al}_x\text{As}$ followed by the contact layer of GaAs. The interfaces between the layers are at x_1 , x_2 , x_3 , and x_4 , respectively. The barrier height (the conduction-band offset) is taken to be 55% of $E_g^{\text{AlAs}} - E_g^{\text{GaAs}}$, the band-gap difference.¹¹ The cross-section area is A . Each electrode has the thickness L . The effective mass of the electron is taken to be m^* whether in GaAs or AlAs. The left barrier and the right barrier are taken to be equally thick: $d_1 = d_2 = d$. w is the width of the well. The voltage bias V_q is such that the lowest quasibound level E_1 is lower in energy than the conduction-band edge of the left electrode.

We use the transfer Hamiltonian method proposed by Bardeen¹⁰ and extend the method to treat the inelastic tunneling of an electron through the excitation of an AlAs phonon. We choose the states ψ_r and ψ_l so that ψ_r is matched to the correct solution for $x \geq x_2$ but decays in the region $x \leq x_1$ instead of satisfying the wave equation, and, similarly, ψ_l continues to decay for $x \geq x_2$. Then ψ_r is a correct solution for the Hamiltonian H for $x \geq x_1$ and ψ_l is correct for $x \leq x_2$. With WKB approximation, we have

$$\begin{aligned} \psi_l(x) &= \left[\frac{2}{AL} \right]^{1/2} e^{ik_l x_1} \sin(k_l x + \gamma_l), \quad x \leq x_1 \\ \psi_l(x) &= \left[\frac{k_l}{\kappa_l} \right]^{1/2} \frac{e^{ik_l x_1} e^{-\kappa_l(x-x_1)}}{\sqrt{2AL}} \\ &= \frac{e^{ik_l x_1}}{\sqrt{AL}} \chi_l(x), \quad x \geq x_1 \end{aligned} \quad (1)$$

where k_l is the wave vector of the electron in the left electrode, $i\kappa_l$ is the imaginary wave vector in the left barrier, and $\chi_l(x)$ is defined in the equation. Similarly,

$$\begin{aligned}\psi_r(x) &= \left[\frac{2}{AL} \right]^{1/2} e^{ik_1 x} \sin(k_r x + \gamma_r), \quad x \geq x_4 \\ \psi_r(x) &= \left[\frac{2}{AL} \right]^{1/2} \left[\frac{k_r}{\kappa_r} \right]^{1/2} \frac{e^{ik_1 x} e^{-\kappa_r(x-x_1)}}{\{[\sin(k_w w)]^2 e^{-2\kappa_2 d_2} + [4 \cos(k_w w)]^2 e^{2\kappa_2 d_2}\}^{1/2}} \\ &= \left[\frac{1}{AL} \right]^{1/2} e^{ik_1 x} \chi_r, \quad x \leq x_2\end{aligned}\quad (2)$$

where k_r is the wave vector in the right electrode, ik_1 is the imaginary wave vector in the left barrier, k_w is the wave vector in the well, ik_2 is the imaginary wave vector in the right barrier, and $\chi_r(x)$ is defined in the equation. The electron-phonon coupling in the left AlAs barrier gives rise to the interaction Hamiltonian

$$H_{e-ph}^a = iD_\Gamma \left[\frac{\hbar q}{2\rho v_s V_{AlAs}} \right] (a_{q\lambda}^\dagger e^{iq\tau} + a_{q\lambda} e^{-iq\tau}) \quad (3)$$

for the deformation-potential (DP) coupling due to the longitudinal-acoustic (LA) phonon mode $q\lambda$, where q is the phonon wave vector and λ specifies the polarization.¹² Here, D_Γ is the deformation potential for Γ -valley electrons, ρ is the density, v_s is the sound velocity in AlAs, and V_{AlAs} is the volume of the left barrier. On the other hand,

$$\begin{aligned}H_{e-ph}^o &= \frac{4\pi i}{q} \left[\frac{\hbar\omega}{8\pi V_{AlAs}} \left(\frac{1}{\epsilon_\infty} - \frac{1}{\epsilon_0} \right) \right]^{1/2} \\ &\times (a_{q\lambda}^\dagger e^{-iq\tau} - a_{q\lambda} e^{iq\tau})\end{aligned}\quad (4)$$

for the polar-optical (PO) coupling due to the longitudinal-optical (LO) phonon mode $q\lambda$.¹² ϵ_0 and ϵ_∞ are the dielectric constants at zero and optical frequen-

cies, respectively. Other kinds of electron-phonon coupling, piezoelectric coupling for example, are much weaker and much less important.¹² They are not considered here. The transition rate can be calculated easily by the application of Fermi's golden rule. The temperature is taken to be zero to simplify our analysis; hence, only phonon emission needs to be considered. The inelastic tunneling current is

$$\begin{aligned}J_{inel} &= \frac{4\pi e}{\hbar} \sum_{q,\lambda} \sum_{\mathbf{k}} \sum_{\mathbf{k}'} |M|^2 f(\epsilon_k) \\ &\times [1 - f(\epsilon_{k'})] \delta(\epsilon_k + eV_a - \epsilon_{k'} - \hbar\omega),\end{aligned}\quad (5)$$

where $\hbar\omega$ is the phonon energy, ϵ_k and $\epsilon_{k'}$ are the kinetic energies of the electrons in the left and right electrode, respectively, and M is the matrix element. Here, \mathbf{k} and \mathbf{k}' are wave vectors of the electron at left and right electrodes, respectively, and $f(\epsilon)$ is the Fermi distribution function. The general expression for J_{inel} at a finite temperature may be derived with the use of many-body theory. Bennett *et al.*¹² have given the derivation of the formula for the single-barrier case. We do not attempt to treat finite temperature case, however. Replacing \sum with \int , we have

$$\begin{aligned}J_{inel} &= \frac{4\pi e}{\hbar} A \sum_{\lambda} \int d^3 q \frac{1}{(2\pi)^3} |U_q|^2 \int d^3 k \frac{1}{(2\pi)^3} \int d^3 k' \frac{1}{(2\pi)^3} |T(q_1; k_1, k'_1)|^2 f(\epsilon_k) [1 - f(\epsilon_{k'})] \\ &\times \delta(\mathbf{k}_1 - \mathbf{k}'_1 - \mathbf{q}_1) (2\pi)^2 \delta(\epsilon_k + eV_a - \epsilon_{k'} - \hbar\omega).\end{aligned}\quad (6)$$

Here, we have

$$U_q = 4\pi e [\hbar\omega(1/\epsilon_0 - 1/\epsilon_\infty)/8\pi]^{1/2} / q \quad (7)$$

for PO coupling, and

$$U_q = D_\Gamma (\hbar q / 2\rho v_s)^{1/2} \quad (8)$$

for DP coupling. T is the overlap integral

$$T(q_1; k_1, k'_1) = \int_{x_1}^{x_2} e^{iq_1 x} \chi_1^* \chi_1 dx. \quad (9)$$

Suppose now the electron is scattered into the quasi-bound level, then ψ_r in the left barrier would be enhanced by the exponential factor $e^{\kappa_2 d_2}$. This can be verified by setting $\cos(k_w w)$ to zero in Eq. (2) when near resonance. This would in turn increase T by the same factor. Therefore, the contribution to the inelastic current due to such

a process would be dominant. It turns out that for PO coupling, we have

$$\begin{aligned}J_{inel} &\geq \frac{2Aem^* d_1^2}{(2\pi)^3 \hbar^3 \kappa_0^2} e^{-2\kappa_0 d_1} e^{E_1/V_b} \frac{E_1}{2} \\ &\times \frac{2}{\pi} e^2 \hbar\omega \frac{k_F^4}{q_0} (1/\epsilon_0 - 1/\epsilon_\infty) \tan^{-1}(1/q_0 d_1),\end{aligned}\quad (10)$$

For DP coupling, we have

$$\begin{aligned}J_{inel} &\geq \frac{2Aem^* d_1^2}{(2\pi)^3 \hbar^3 \kappa_0^2} e^{-2\kappa_0 d_1} e^{E_1/V_b} \frac{E_1}{2} \frac{\pi k_F^4}{2\pi^2} \frac{D_\Gamma^2 \hbar}{2\rho v_s} \\ &\times \{d_1^{-1} (d_1^{-2} + q_0^2)^{1/2} + q_0^2 \sinh^{-1}[(q_0 d_1)^{-1}]\}.\end{aligned}\quad (11)$$

Here, E_b is the zero-bias barrier height, $\kappa_0 = (2m^*E_b/\hbar^2)^{1/2}$, $V_b = 2E_b/\kappa_0 d_1$, and q_0 satisfies $\hbar^2 q_0^2/2m^* = eV_a/2 - \hbar\omega - E_1$.

We now compare contributions to the current from the elastic and the inelastic process. We consider only the inelastic process induced by PO coupling or DP coupling. Inelastic processes induced by other couplings will further increase the inelastic current. Therefore, the inelastic current we consider here is a lower bound of the actual value. However, even without a complete knowledge of the inelastic current, we can still demonstrate the dramatic change in order of magnitude of the current which is due to the inelastic processes.

In Fig. 1, we plot the lower limit of $J_{\text{inel}}/J_{\text{el}}$, the ratio of inelastic current to elastic current, versus barrier thickness for biased symmetric structures with $w = 50$ Å, $E_f = 50$ meV, and $V_a = 0.4$ V. Both LO and LA phonon-induced effects are shown. For thin barrier cases where $d = 20$ Å, polar coupling induces an inelastic current comparable to the elastic current. As can be seen, deformation-potential coupling has much smaller effects than polar coupling. The reason is that the PO coupling is much stronger than the DP coupling. We may neglect the contribution from DP coupling in comparison to that from PO coupling. Effects of both coupling increase as the barrier becomes wider, due to the exponential enhancement in the right wave function ψ_r . For the thick barrier case where $d = 40$ Å, polar coupling even gives rise to an inelastic current which is a thousand

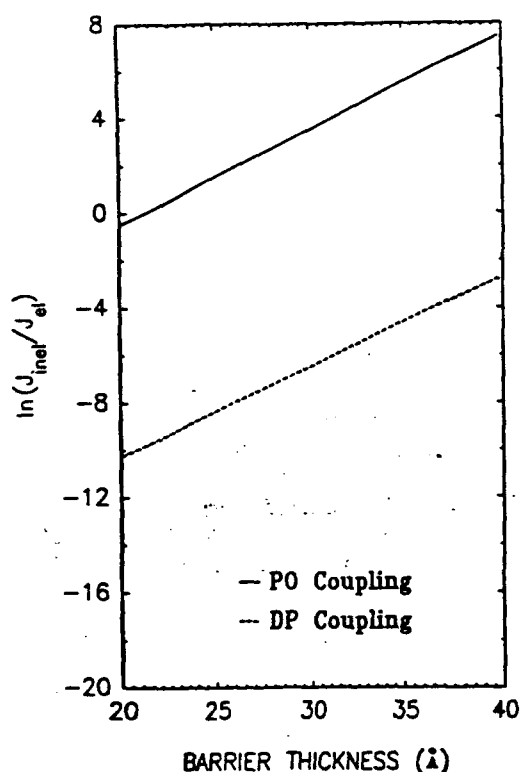


FIG. 1. The lower limit of $J_{\text{inel}}/J_{\text{el}}$; $E_1 \approx 150$ meV with respect to the conduction-band edge of the GaAs well.

times as large as the elastic one.

In Fig. 2, we plot the upper limit of the ratio of the resonant current, which occurs at $V_a = 0.3$ V, to the current at $V_a = 0.4$ V, which occurs off resonance, versus barrier thickness. The dotted line is obtained with Tsu-Esaki model,¹² which includes only elastic process. In that case, the ratio shown here is equal to the peak-to-valley ratio of the J - V curve. The solid line is obtained with inelastic tunneling included. The peak current is mostly due to the elastic tunneling, since, at resonance, the elastic current is much larger than the inelastic current. The current off resonance is largely due to the inelastic tunneling, since the inelastic current is much larger than the elastic current, as shown in Fig. 2. The ratios shown by the two curves are comparable for thin barrier cases. However, as the barrier becomes thicker, the solid curve only varies slowly, since both J_{peak} and J_{valley} have same exponential dependence. For barrier thickness equal to 40 Å, magnitudes of the two ratios differ by 7 in the natural log scale. The theory with the inelastic process included predicts a much smaller value of ratio for thick barrier cases.

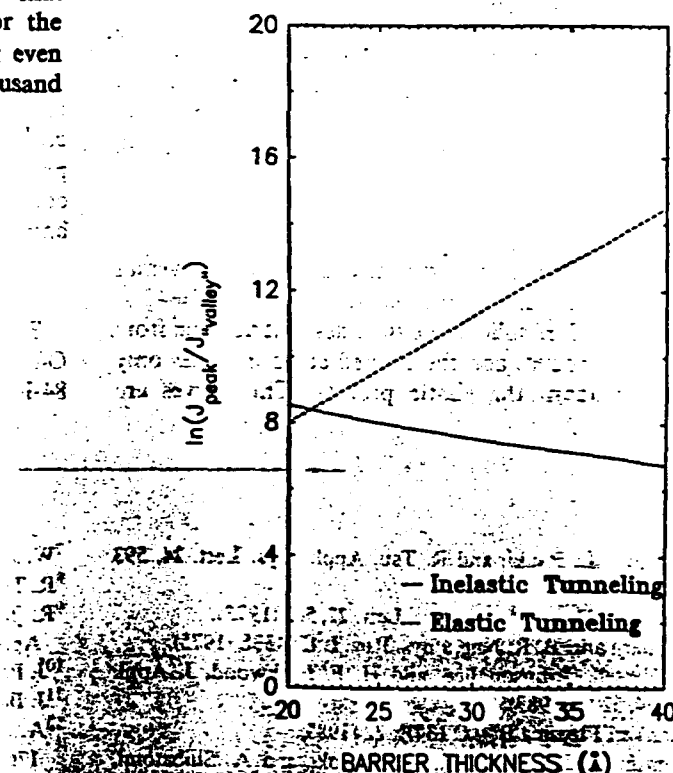


FIG. 2. The upper bound of $J_{\text{peak}}/J_{\text{valley}}$, the ratio of the peak current at $V_a = 0.3$ V (at resonance, the peak in the current-voltage curve) to the current at $V_a = 0.4$ V (off resonance, the valley in the case of elastic transport but not necessarily in the case with inelastic processes) vs barrier thickness with and without the inelastic part of the current included for biased symmetric structures with a well width of 50 Å, and $E_f = 50$ meV.

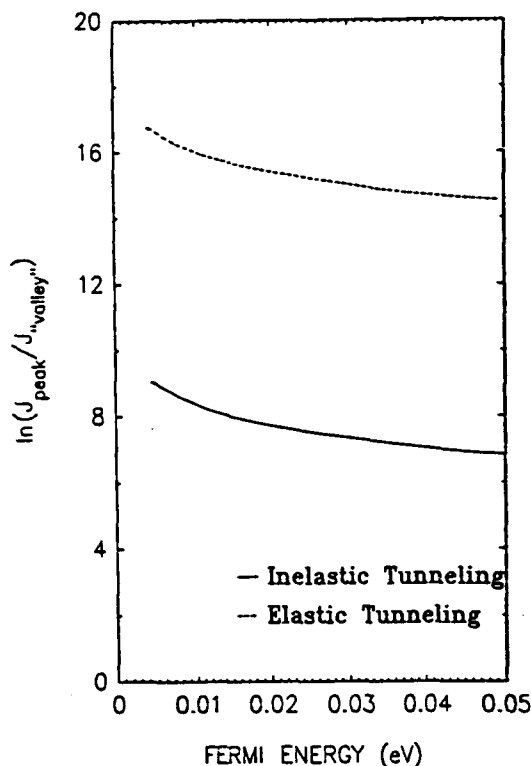


FIG. 3. The upper bound of $J_{\text{peak}}/J_{\text{valley}}$, the ratio of the peak current at $V_a=0.3$ V (at resonance, the peak in the current-voltage case) to the current at $V_a=0.4$ V (off resonance, the valley in the case of elastic transport but not necessarily in the case with inelastic processes) vs Fermi energy for the symmetric structure with a barrier thickness of 40 Å and a well width of 50 Å.

In Fig. 3, the upper bound of the ratio is shown versus Fermi energy for the symmetric structure with $d=40$ Å and $w=50$ Å. The solid curve includes contribution from the inelastic process and the dashed curve includes only contribution from the elastic process. The curves are

shown for the region from $E_f=5$ meV to $E_f=50$ meV corresponding to dopant density from $10^{17}/\text{cm}^3$ to $10^{18}/\text{cm}^3$ currently used in the tunneling experiments. We see that both curves behave similarly as the Fermi energy changes. The difference between them is maintained through the Fermi energy range of interest. This shows the importance of the inelastic process for both low and high doping cases.

In summary, the inclusion of the inelastic tunneling in the theory for double-barrier structures is very important. We have studied specifically the inelastic tunneling induced by phonons. Two types of coupling have been considered. The PO coupling is much stronger than the deformation-potential coupling, and hence the current induced by PO coupling is much larger than that by DP coupling. Because of similar reasons, we expect the effect of piezoelectric (PE) coupling also to be negligible in comparison to that of PO coupling.

The electron-phonon interaction induces a channel through which the electron can tunnel much more readily than through the elastic channel. With the excitation of a barrier phonon, the electron can utilize the quasi-bound level to tunnel through the barrier. The *inelastic resonant tunneling* enhances the current off resonance by orders of magnitude. The effects are best reflected in the big difference between the magnitudes of current ratios which are predicted, with and without inclusion of electron-phonon coupling, in the simple model of Tsu and Esaki.² We expect the inclusion of inelastic processes to be important in any refined theory such as the self-consistent analysis of Ohnishi⁵ or Frensky's transport approach.⁷ Other mechanisms such as impurity scattering could also be critical to current transport in a double-barrier structure.

The authors gratefully acknowledge the support of the Office of Naval Research under Contract No. N00014-84-K-0501.

¹L. L. Chang, L. Esaki, and R. Tsu, Appl. Phys. Lett. 24, 593 (1974).

²R. Tsu and L. Esaki, Appl. Phys. Lett. 22, 562 (1973).

³D. Mukherji and B. R. Nag, Phys. Rev. B 12, 4338 (1975).

⁴M. O. Vessell, Johnson Lee, and H. F. Lockwood, J. Appl. Phys. 54, 5206 (1983).

⁵J. R. Barker, Physica B + C 134B, 22 (1985).

⁶H. Ohnishi, T. Inata, S. Muto, N. Naoki, and A. Shibatomi, Appl. Phys. Lett. 49, 1248 (1986).

⁷W. J. Frensky, Appl. Phys. Lett. 51, 448 (1987).

⁸R. Tsu and G. Dohler, Phys. Rev. B 12, 680 (1975).

⁹R. T. Collins, J. Lambe, T. C. McGill, and R. D. Burnham, Appl. Phys. Lett. 44, 532 (1984).

¹⁰J. Bardeen, Phys. Rev. Lett. 6, 57 (1961).

¹¹J. Batey and S. L. Wright, J. Appl. Phys. 59, 200 (1986).

¹²A. J. Bennett, C. B. Duke, and S. D. Silverstein, Phys. Rev. 176, 969 (1968).

APPENDIX 3

III-V/II-VI double-barrier resonant tunneling structures

E. T. Yu and T. C. McGill

*T. J. Watson, Sr., Laboratory of Applied Physics, California Institute of Technology,
Pasadena, California 91125*

(Received 7 March 1988; accepted for publication 29 April 1988)

GaAs-ZnSe and InAs-ZnTe double-barrier resonant tunneling devices are proposed and analyzed theoretically. These structures would provide a novel way to study mixed III-V/II-VI materials systems and growth techniques, and may also yield devices that are faster and have greater peak-to-valley current ratios than GaAs-AlGaAs tunnel structures. In the GaAs-ZnSe system, the increase in speed is due to the smaller dielectric constant in ZnSe, compared to that in AlGaAs. In the InAs-ZnTe system, the increase in speed is due to the small dielectric constant in ZnTe and the high mobility in InAs, and the larger peak-to-valley ratio is due to the large conduction-band offset that is expected. We calculate current-voltage curves for these devices and show that their negative differential resistance current-voltage characteristics should be comparable or superior to those of GaAs-AlGaAs devices. The effects of band bending and the general method used to calculate current as a function of voltage are briefly discussed.

Over the past several years, much of the study of device physics and technology has focused on III-V materials systems. However, many of the device concepts developed and demonstrated in III-V systems can be applied to other materials as well. One device that has been the subject of considerable interest recently, both for studying very thin semiconductor heterostructures and as a possible high-speed device, is the double-barrier resonant tunneling structure. In this letter, we discuss theoretically some properties of GaAs-ZnSe and InAs-ZnTe double-barrier resonant tunneling structures; this is the first time mixed III-V/II-VI tunneling structures have been proposed. ZnSe in particular is a potentially important II-VI material because its lattice parameter is very close to that of GaAs ($\sim 0.27\%$ mismatch), and because its band gap is very wide (2.67 eV at 300 K), which makes visible light emission possible. Furthermore, the successful growth of ZnSe/GaAs double heterostructures¹ would seem to indicate that GaAs-ZnSe double-barrier structures can be grown by the same techniques. GaAs-ZnSe and InAs-ZnTe tunnel structures would in fact provide a novel way to study mixed III-V/II-VI materials systems and growth techniques.

For actual device applications, one advantage that a GaAs-ZnSe structure may have over a GaAs-AlGaAs device is speed. The time for an electron to tunnel across the device will typically be on the order of 10^{-13} – 10^{-15} s, and therefore will not be the limiting factor in the speed of the device.² A parameter that may be more relevant to the device speed is the RC time constant for charging the capacitor formed by the barriers. This parameter can be estimated as $\tau = \hbar/\Delta E$, where ΔE is the width of the transmission resonance of the barrier-well structure; typically, τ is on the order of 1 ps. Since the capacitance is proportional to the dielectric constant in the barrier, and since ZnSe has a lower dielectric constant than AlGaAs (9.1 vs 12.0), the capacitance, and therefore the RC time constant, should be reduced by replacing AlGaAs with ZnSe.

InAs-ZnTe tunnel structures should exhibit an even greater advantage in speed. The dielectric constant for ZnTe is 10.4, which again is smaller than that in AlGaAs. More

important, InAs has a much higher mobility than GaAs [$33\,000$ vs 8500 $\text{cm}^2/(\text{V s})$ at 300 K]. The resistivity in InAs will therefore be much lower than in GaAs, leading to a large reduction in the RC time constant. The low resistivity in InAs will also permit a greater fraction of the voltage drop across the device to occur in the barrier-well region, so that a smaller bias voltage will be required to achieve the maximum tunneling current.

The material parameter that is most important in determining the electrical properties of the double barrier is the conduction-band offset. The valence-band offset for the (110)ZnSe-GaAs heterojunction has been measured by x-ray photoelectron spectroscopy³ and found to be, depending on growth conditions, between 0.96 and 1.10 eV at 300 K. The value of 0.96 eV was obtained for a heterojunction in which ZnSe was deposited on GaAs at $\sim 300^\circ\text{C}$, while the value of 1.10 eV was for a sample in which ZnSe was deposited on GaAs at 23°C , and annealed at $\sim 300^\circ\text{C}$. The corresponding conduction-band offset is between 0.15 and 0.29 eV, which is comparable to the direct-band offset in the GaAs- $\text{Al}_x\text{Ga}_{1-x}\text{As}$ system (0.25 eV for $x = 0.33$). As has been seen in the GaAs-AlGaAs system, band offset values in this range make the fabrication of high quality high electron mobility transistor structures difficult, but are sufficient for achieving negative differential resistance in tunnel structures.

In the InAs-ZnTe system, the conduction-band offset is probably very large, which is another advantage of this system over GaAs-AlGaAs. The value of the band offset has not been measured directly, but we can obtain some idea of its value if we assume that band offsets are transitive. For GaAs-ZnSe, the valence-band offset is $\Delta E_v = 1.1$ eV; for InAs-GaAs, $\Delta E_v = 0.17$ eV (Ref. 4), and for ZnTe-ZnSe, $\Delta E_v = 0.98$ eV.⁵ Using these values, we obtain $\Delta E_v \approx 0.30$ eV or $\Delta E_c \approx 1.6$ eV for InAs-ZnTe. The large conduction-band offset will reduce thermionic currents through higher resonances and over the barrier, facilitating device operation at room temperature.

We have calculated current-voltage characteristics for these structures, and for a comparable GaAs-AlGaAs de-

vice as well. For the GaAs-ZnSe system, we have assumed that the double-barrier structure consists of a 50 Å GaAs well sandwiched between two 50 Å ZnSe barriers. The well and barrier are assumed to be undoped, and the contact layers are assumed to be degenerately doped (10^{18} cm^{-3}) GaAs. For the InAs-ZnTe system, the structure consists of an undoped 50 Å InAs well sandwiched between two undoped 20 Å ZnTe barriers. The contact layers are degenerately doped (10^{18} cm^{-3}) InAs. Our calculations assume the following material parameters (for $T = 300 \text{ K}$): for GaAs, $m^* = 0.066m_e$, $E_g = 1.42 \text{ eV}$, $\epsilon = 12.9\epsilon_0$; for ZnSe, $m^* = 0.16m_e$, $E_g = 2.67 \text{ eV}$, $\epsilon = 9.1\epsilon_0$; for InAs, $m^* = 0.028m_e$, $E_g = 0.36 \text{ eV}$, $\epsilon = 14.6\epsilon_0$; for ZnTe, $m^* = 0.11m_e$, $E_g = 2.26 \text{ eV}$, $\epsilon = 10.4\epsilon_0$. These parameters change slightly at $T = 77 \text{ K}$, but the changes are not sufficient to prevent the occurrence of negative differential resistance.

Energy-band diagrams are schematically illustrated in Fig. 1 for zero bias and for a voltage V applied across the contact layers. Band bending effects, as shown in Fig. 1 for nonzero bias voltage, have been included by solving for the conduction-band-edge energy, which acts as an electrostatic potential for electrons, using Poisson's equation. When solving for the conduction-band-edge energy, we do not include the effects of charge buildup in the quantum well during device operation, i.e., we do not solve for the electron wave function and the position of the conduction-band edge self-consistently. We assume that the barrier and well regions are fully depleted of carriers, and therefore obtain linear voltage drops across these layers. This assumption is included only as a matter of convenience and is not necessary for achieving negative differential resistance. We find that including band bending effects increases the peak current, since the barrier is effectively lowered by bending in the accumulation layer. However, peak-to-valley ratios are not significantly affected by band bending.

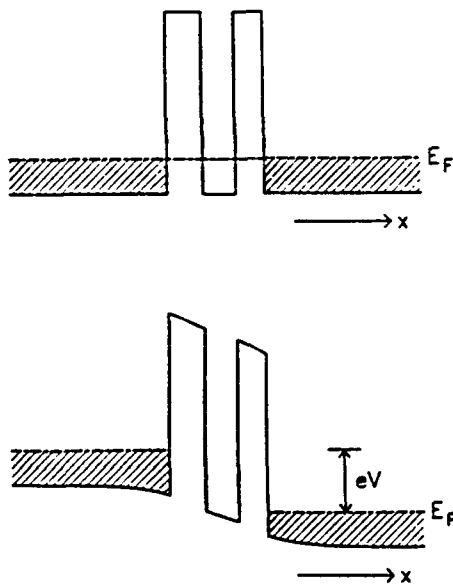


FIG. 1. Top: Conduction-band edge of the double-barrier structure as a function of position, with no applied voltage. Bottom: Conduction-band edge when a voltage V is applied to the device. Note the band bending in the contact layers.

The transmission coefficient is calculated as a function of energy using a transfer matrix technique⁶ in which the device is divided into small intervals, and the potential then assumed to be constant in each interval. For the purposes of calculating the transmission coefficient, we consider the device to include the well, the barriers, and electrode regions in which band bending effects are not negligible. We enforce the usual boundary conditions between intervals, i.e., that ψ and $(d\psi/dx)/m^*$ be continuous, where ψ is the envelope function of the electron wave function in the solid. We also assume that the transverse wave vector k_{\perp} is conserved in the tunneling process, and that the total energy of the electron is conserved. These two assumptions, combined with the fact that the effective masses in the barriers and the well are not equal, lead to a dependence of the transmission coefficient on k_{\perp} , but we found this effect to be small.

For electron energies above the conduction-band edge, we employ the effective mass approximation $E = \hbar^2 k^2 / 2m^*$. For electron energies below the conduction-band edge, the wave vector is imaginary; its value is calculated using Kane's eight-band model⁷ and the $k \cdot p$ theory outlined by Smith and Mailhot.⁸ To obtain the transmission coefficient, we assume plane wave solutions for ψ outside the device. For $x \rightarrow -\infty$, we have incident and reflected waves, and for $x \rightarrow +\infty$, we have a transmitted wave:

$$\psi = \begin{cases} e^{ik_1 x} + r e^{-ik_1 x}, & x \rightarrow -\infty, \\ t e^{ik_2 x}, & x \rightarrow +\infty. \end{cases}$$

The transmission coefficient is defined to be the ratio of transmitted to incident current, $T = k_2 |t|^2 / k_1$.

The current is then calculated by including the appropriate Fermi factors and electron velocities, and integrating over the incident electron energy distribution:

$$\begin{aligned} J &= \frac{e}{4\pi^3} \left(\int T(E_1) f(E) [1 - f(E + eV)] \frac{1}{\hbar} \frac{\partial E}{\partial k_{11}} d^3 k_1 \right. \\ &\quad \left. - \int T(E_1) f(E + eV) [1 - f(E)] \frac{1}{\hbar} \frac{\partial E}{\partial k_{21}} d^3 k_2 \right) \quad (1) \\ &= \frac{em^* k_B T}{2\pi^2 \hbar^3} \int_0^\infty dE_1 T(E_1) \\ &\quad \times \ln \left(\frac{1 + \exp[(E_F - E_1)/k_B T]}{1 + \exp[(E_F - E_1 - eV)/k_B T]} \right), \quad (2) \end{aligned}$$

where m^* is the effective mass in the electrodes, k_1 is the component of the wave vector normal to the barriers, and $E_1 = \hbar^2 k_1^2 / 2m^*$. In Eq. (1), the first integral corresponds to electron current in the $+x$ direction, and the second integral to current in the $-x$ direction. An integration over the transverse wave vector k_{\perp} has been carried out to obtain (2). From Eq. (1), we see that the integrals over the longitudinal wave vector k_1 both contain the factor $(\partial E / \partial k_1) dk_1 = dE_1$, i.e., the effects of the differing velocities on each side of the device are canceled by the effects of the different one-dimensional densities of states at a given energy. This cancellation occurs because we must calculate both the density of states and the electron group velocity $v_1 \equiv (\partial E / \partial k_1) / \hbar$ for the side of the device on which the current is incident, because of the fact that we have defined $T(E_1)$ as the ratio of the transmitted to incident current. As a result, the expres-

sion we obtain for J is identical to that obtained by Tsu and Esaki,⁹ except for the fact that we have defined $T(E_1)$ to be a transmission probability for the electron current, rather than for probability densities.

Figure 2 shows current-voltage curves for the GaAs/ZnSe tunnel structure at $T = 77$ and 300 K. The peak current is approximately the same at both temperatures, indicating that the resonant current is much larger than the thermionic currents over the barriers. However, the peak-to-valley ratios vary considerably with temperature, since the barriers formed by ZnSe are low enough to allow substantial thermionic currents at room temperature. At 77 K thermionic currents are negligible, and we have calculated a peak-to-valley ratio of ~ 1000 ; at 300 K, thermionic currents become important, and a peak-to-valley ratio of 23 is obtained.

Figure 3 shows current-voltage curves for InAs-ZnTe and GaAs-AlGaAs tunnel structures. The dashed curve in Fig. 3 is for a GaAs-AlGaAs tunnel structure consisting of undoped 40 Å $\text{Al}_{0.33}\text{Ga}_{0.67}\text{As}$ barriers and an undoped 50 Å GaAs well, with degenerately doped (10^{18} cm^{-3}) GaAs contact layers. The peak current for this structure is somewhat higher than that for the InAs-ZnTe structure, but the peak-to-valley ratio is much lower (92 vs ~ 1700), indicating that InAs-ZnTe devices would have current-voltage characteristics superior to those of GaAs-AlGaAs structures. Furthermore, the large peak-to-valley ratio obtained for the InAs-ZnTe structure would vary little with temperature, because of the height of the ZnTe barrier. Thus InAs-ZnTe tunnel structures would appear to be good candidates for devices capable of operating at room temperature.

In summary, we have studied theoretically GaAs-ZnSe and InAs-ZnTe double-barrier resonant tunneling structures. These structures are the first mixed III-V/II-VI tunneling devices that have been proposed and should provide novel ways to examine mixed III-V/II-VI materials systems

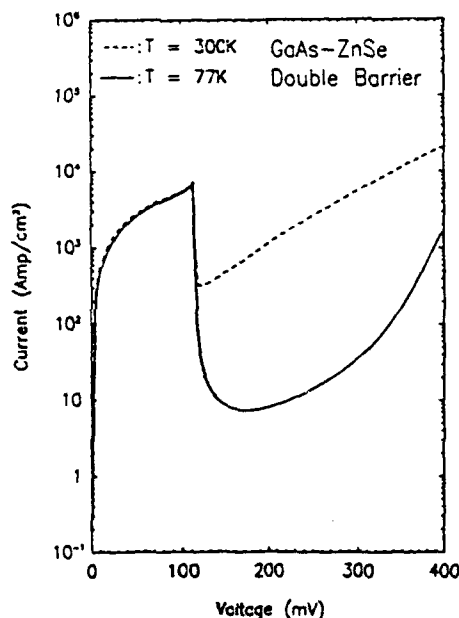


FIG. 2. Current-voltage characteristics for the GaAs-ZnSe tunnel structure calculated at $T = 77$ and 300 K. The peak currents are nearly equal for the two temperatures, but the peak-to-valley ratio is much smaller at 300 K (23 at 300 K vs ~ 1000 at 77 K).

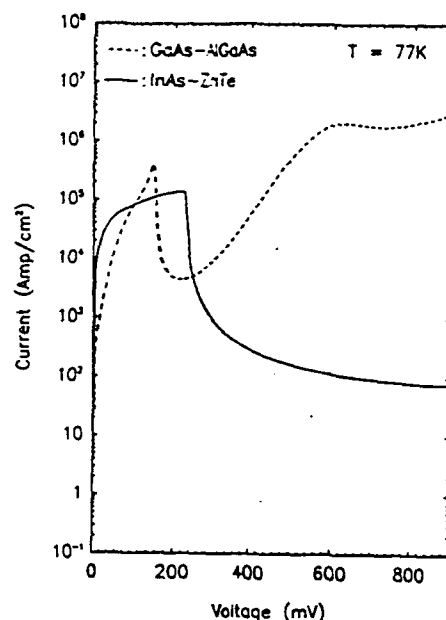


FIG. 3. Dashed line: Current-voltage characteristic for a GaAs- $\text{Al}_{0.33}\text{Ga}_{0.67}\text{As}$ tunnel structure. Solid line: Current-voltage characteristic for an InAs-ZnTe tunnel structure. Both curves are calculated at $T = 77$ K.

and growth techniques. Using the measured values for the band offset, we have shown that the GaAs-ZnSe double-barrier structure should produce negative differential resistance. We also note that the smaller dielectric constant in ZnSe, compared to that in AlGaAs, may lead to somewhat faster device operation. For the InAs-ZnTe structure, we calculate a conduction-band offset of approximately 1.6 eV by assuming that band offsets are transitive and using measured valence-band offsets for GaAs-ZnSe, ZnSe-ZnTe, and InAs-GaAs. We obtain very large peak-to-valley ratios for this device, and the size of the band offset indicates that this device should work well at room temperature. In addition, the small dielectric constant in ZnTe and the high mobility in InAs should lead to a substantial advantage in speed over GaAs-AlGaAs devices, and the high mobility in InAs should decrease the bias voltage required to achieve the maximum tunneling current.

We would like to acknowledge valuable discussions with Y. Rajakarunanyake, D. H. Chow, and T. K. Woodward. One of us (E.T.Y.) is grateful for financial support from a National Science Foundation Graduate Fellowship. This work was supported in part by the Office of Naval Research under contract No. 00014-84-K-0501.

¹M. C. Tamargo, J. L. de Miguel, B. J. Skromme, D. M. Hwang, M. H. Meynadier, and R. E. Nahory, in Eighth MBE Workshop, UCLA, Los Angeles, CA, 1987, paper FP4.

²B. Ricco and M. Ya. Azbel, Phys. Rev. B 29, 1970 (1984).

³S. P. Kowalczyk, E. A. Kraut, J. R. Waldrop, and R. W. Grant, J. Vac. Sci. Technol. 21, 481 (1982).

⁴S. P. Kowalczyk, W. J. Schaffer, E. A. Kraut, and R. W. Grant, J. Vac. Sci. Technol. 20, 705 (1982).

⁵Y. Rajakarunanyake, R. H. Miles, G. Y. Wu, and T. C. McGill, Phys. Rev. B 37, 15 June (1988).

⁶M. O. Vassell, J. Lee, and H. F. Lockwood, J. Appl. Phys. 54, 5206 (1983).

⁷E. O. Kane, J. Phys. Chem. Solids 1, 82 (1956).

⁸D. L. Smith and C. Mailhot, Phys. Rev. B 33, 8345 (1986).

⁹R. Tsu and L. Esaki, Appl. Phys. Lett. 22, 562 (1973).

APPENDIX 4

Commutativity of the GaAs/AlAs (100) band offset

E. T. Yu, D. H. Chow, and T. C. McGill,

T. J. Watson, Sr., Laboratory of Applied Physics, California Institute of Technology, Pasadena, California 91125

(Received 22 September 1988; accepted 22 September 1988)

X-ray photoelectron spectroscopy is used to measure the valence-band offset *in situ* for GaAs/AlAs (100) heterojunctions grown by molecular beam epitaxy. Ga 3*d* and Al 2*p* core level to valence-band edge binding energy differences are measured in GaAs (100) and AlAs (100) samples, respectively, and the Al 2*p* to Ga 3*d* core level binding energy difference is measured in GaAs-AlAs (100) and AlAs-GaAs (100) heterojunctions. Measurements of the Al 2*p* to Ga 3*d* core level energy separations indicate that the band offset for GaAs/AlAs (100) is commutative; the value we obtain is $\Delta E_v = 0.46 \pm 0.07$ eV. Our observation of commutativity is believed to be a consequence of the high quality of our GaAs/AlAs (100) heterojunctions, and of the inherent commutativity of the GaAs/AlAs (100) band offset.

I. INTRODUCTION

Band offsets at semiconductor heterojunctions are of great importance in solid-state physics, both from a fundamental point of view and for device applications. The GaAs/AlAs band offset in particular has been a subject of extensive study, due to the technological importance of the GaAs/Al_xGa_{1-x}As heterojunction system. An important but unresolved experimental issue in this system is that of commutativity (i.e., independence of growth sequence) of the band offset. Commutativity is consistent with current theoretical models and some experimental results^{1,2}; however, a dependence of the band offset on growth sequence has also been reported.^{3,4} Published experimental values^{1-4,8} for the GaAs/AlAs valence-band offset range from $\Delta E_v = 0.36$ eV to $\Delta E_v = 0.56$ eV.

In this paper we present the results of measurements of the band offset in GaAs-AlAs (100) and AlAs-GaAs (100) heterojunctions using x-ray photoelectron spectroscopy (XPS); we adopt the convention of listing the top layer in the heterojunction first, e.g., GaAs-AlAs indicates a heterojunction with GaAs grown on top of AlAs; GaAs/AlAs refers collectively to both growth sequences. We describe sample preparation and experimental techniques in Sec. II. In Sec. III we present and discuss the results of our experiments. Sec. IV concludes the paper.

II. EXPERIMENT

The samples studied in this experiment were grown by molecular beam epitaxy (MBE) in a PHI 430 growth chamber on Si-doped *n*⁺-GaAs (100) substrates. The substrate preparation consisted of a degrease followed by a 90-s etch in 5:1:1 H₂SO₄:H₂O₂:H₂O. The native oxide was desorbed in the growth chamber by heating the substrate to ~610 °C in an As flux. All of the samples were grown at 600 °C and were lightly doped *n*-type with Si ($n \approx 1 \times 10^{16}$ cm⁻³) to avoid both sample charging effects and excessive band bending due to Fermi-level pinning at the surface of the specimen.

Epitaxial GaAs layers > 1 μm in thickness were used to make the bulk GaAs XPS measurements. Electron mobilities in these films were comparable to those typically report-

ed for high-quality MBE growth,⁹ and the samples exhibited good photoluminescence at low temperatures. Two bulk AlAs samples were grown for this study; each consisted of a 2500-Å-thick epitaxial AlAs layer, with one grown on top of a 1.5-μm GaAs buffer layer and the other on top of a 1500-Å Al_{0.3}Ga_{0.7}As buffer.

Two types of heterojunction samples were grown, allowing the commutativity of the band offset to be checked. One type consisted of 25 Å of GaAs on top of either 500, 200, or 100 Å of AlAs, while the other consisted of 25 Å of AlAs on top of 1000 Å of GaAs; growth interruption was not used in fabricating the heterojunction samples. In both cases, the interfaces were believed to be fairly abrupt based upon results from quantum well photoluminescence (the quantum well luminescence peak width was 3.8 meV full width at half-maximum (FWHM) at 9 μW/cm² incident power) and double-barrier resonant tunneling experiments on samples with similarly grown interfaces.

XPS measurements were obtained using a Perkin-Elmer Model 5100 analysis system; samples were probed using a monochromatized Al Kα x-ray source ($h\nu = 1486.6$ eV), and electron energies were measured by a spherical capacitor analyzer. Au 4*f* core level peaks had full widths at half-maximum of ~0.73 eV. The base pressure in the XPS chamber is typically $\sim 5 \times 10^{-10}$ Torr, and the analysis chamber is connected to the MBE chamber via a UHV transfer tube, allowing samples to be grown and analyzed without being exposed to atmosphere. This arrangement eliminates experimental uncertainties associated with surface passivation, sputter cleaning, and annealing of samples that have been transferred through atmosphere. Measurements were obtained from three pure GaAs (100) and two pure AlAs (100) samples, and from three GaAs-AlAs (100) and two AlAs-GaAs (100) heterojunctions. Figure 1 shows a schematic energy-band diagram for the GaAs/AlAs interface. The core levels of interest in the band offset measurement are the Al 2*p* level and the Ga 3*d* level in AlAs and GaAs, respectively. From Figure 1, it can be seen that the valence-band offset is given by

$$\Delta E_v = (E_{\text{Al } 2p}^{\text{AlAs}} - E_{\text{Ga } 3d}^{\text{GaAs}}) + (E_{\text{Ga } 3d}^{\text{GaAs}} - E_v^{\text{GaAs}}) - (E_{\text{Al } 2p}^{\text{AlAs}} - E_v^{\text{AlAs}}). \quad (1)$$

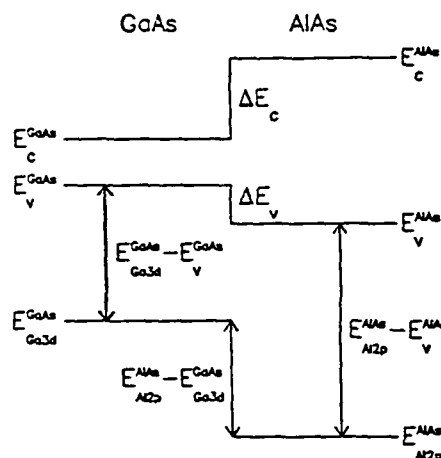


FIG. 1. Schematic energy band diagram for the GaAs/AlAs interface.

The core level to valence-band edge binding energy differences are obtained from measurements on pure GaAs and AlAs samples, and the Al 2*p* to Ga 3*d* core level binding energy differences are obtained from the heterojunction samples.

For each sample, a binding energy window that included all energy levels of interest was scanned repeatedly for ~15–20 h. Due to the low count rate for electrons near the valence-band edge, energies in that region were sampled for a longer time than energies in other parts of the spectrum. Spectra from pure GaAs and pure AlAs and from GaAs–

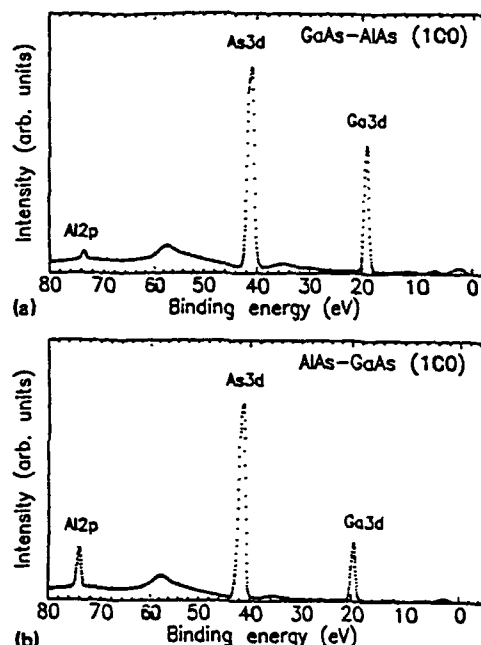


FIG. 3. Representative binding energy XPS spectra for (a) GaAs–AlAs (100) and (b) AlAs–GaAs (100) heterojunction samples. Core level to core level binding energy differences are obtained from these spectra.

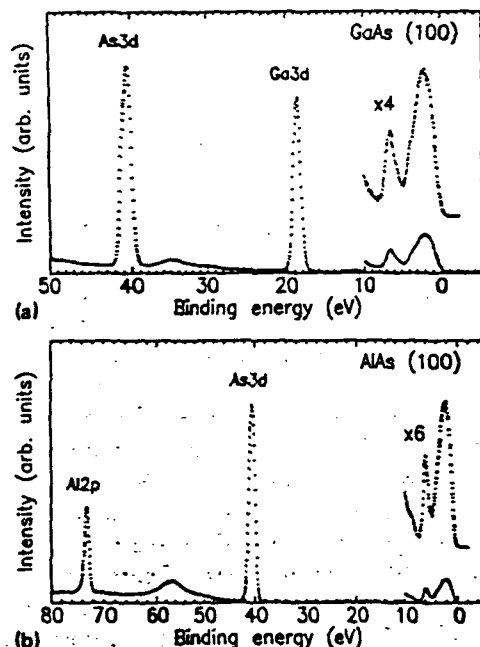


FIG. 2. Representative binding energy XPS spectra for (a) GaAs (100) and (b) AlAs (100) samples. Core level to valence-band edge binding energy differences are obtained from these spectra. The discontinuities in the spectra at 10 eV binding energy are due to the longer sampling times used during data acquisition near the valence-band edge; the valence-band spectra are also shown on enlarged intensity scales, as indicated in the figure.

AlAs and AlAs–GaAs heterojunctions are shown in Figs. 2 and 3, respectively. In Fig. 2, the discontinuities in the spectra at 10-eV binding energy are due to the longer sampling time near the valence-band edge; the valence-band spectra are also shown on enlarged scales, as indicated in the figure.

To obtain accurate core level to core level and core level to valence-band edge binding energy differences, it is necessary to determine peak positions and valence-band edge positions to a high degree of precision. To find core level peak positions, we subtracted from each core level peak a background function (arising from inelastic scattering in the sample) proportional to the integrated photoelectron intensity, and defined the peak energy to be the midpoint of the two energies at which the intensity was one-half the maximum intensity. The uncertainty in this determination of the peak position was taken to be ± 0.02 eV, and typically core level energy separations were reproducible to better than ± 0.01 eV for a given sample.

To locate the position of the valence-band edge in the XPS spectrum, we employed the precision analysis technique developed by Kraut *et al.*¹⁰ In this approach, the XPS spectrum near the valence-band edge is modeled as a convolution of a theoretical valence-band density of states with an experimentally determined XPS instrumental resolution function. This model function is then fitted to the experimental data to give the position of the valence-band edge. Due to the similarity in the valence-band spectra for GaAs and AlAs,⁴ we were able to use the GaAs nonlocal pseudopotential valence-band density of states¹¹ in analyzing data from both materials. For a given sample, core level to valence-band edge binding energy differences were reproducible to better than ± 0.04 eV.

When determining the position of a valence-band edge

using this method, complications can arise from the presence of surface states in the same energy region as the valence band.¹⁰ These surface states produce contributions to the XPS spectrum that are unaccounted for in the theoretical valence-band density of states, and can affect the calculated position of the valence-band edge by ~ 0.1 eV or more. No such effects were observed in our AlAs (100) samples, but a p_z -like surface state was detected in the GaAs (100) samples, in agreement with previous studies of the GaAs (100)-(2 \times 4) reconstructed surface.¹² Thus, the position of the GaAs valence-band edge was determined by analyzing the XPS valence-band spectrum only in an energy region in which no surface states were observed.

III. RESULTS AND DISCUSSION

The measured core level to valence-band edge binding energy differences are shown in Table I. For GaAs (100), the result in $(E_{\text{Ga}3d}^{\text{GaAs}} - E_{\text{v}}^{\text{GaAs}}) = 18.73 \pm 0.05$ eV, and for AlAs (100) we obtain $(E_{\text{Al}2p}^{\text{AlAs}} - E_{\text{v}}^{\text{AlAs}}) = 72.71 \pm 0.04$ eV. These values are in good agreement with those obtained by Waldrop, Grant, and Kraut.⁴ Table II lists the core level binding energy differences for the AlAs-GaAs (100) and GaAs-AlAs (100) heterojunctions. For the GaAs-AlAs interface, we find $(E_{\text{Al}2p}^{\text{AlAs}} - E_{\text{Ga}3d}^{\text{GaAs}}) = 54.45 \pm 0.02$ eV. Using Eq. (1), we see that this value corresponds to a valence-band offset of 0.47 ± 0.07 eV. The core level binding energy difference for the AlAs-GaAs (100) interface was found to be $(E_{\text{Al}2p}^{\text{AlAs}} - E_{\text{Ga}3d}^{\text{GaAs}}) = 54.43 \pm 0.02$ eV, corresponding to a valence-band offset of 0.45 ± 0.07 eV.

From these measurements we see that the valence-band offsets for the two different growth sequences are within 0.02 eV of each other, indicating that the GaAs/AlAs (100) band offset is commutative. The observation of commutativity for GaAs/AlAs (100) is in agreement with the result of Katnani and Bauer,¹ but disagrees with that of Waldrop *et al.*,⁴ who reported a dependence of the band offset on both growth sequence and crystal orientation. The fact that XPS band offset measurements are not consistently commutative or noncommutative would seem to indicate that growth conditions and interface quality can have a significant effect on the value of the band offset. If this were the case, one would expect that nearly ideal interfaces would exhibit commutativity, while nonideal interfaces would not.

The value obtained for the band offset, 0.46 eV, is well within the range of experimental values that have been reported. XPS measurements by Waldrop *et al.*⁴ yielded a valence-band offset of 0.46 eV for the AlAs-GaAs (100) heter-

TABLE I. Measured core level to valence-band edge binding energy differences for GaAs (100) and AlAs (100).

Semiconductor	Sample	$E_{\text{Ga}3d}^{\text{GaAs}} - E_{\text{v}}^{\text{GaAs}}$ (eV)	$E_{\text{Al}2p}^{\text{AlAs}} - E_{\text{v}}^{\text{AlAs}}$ (eV)
GaAs (100)	III024	18.75	
GaAs (100)	III031	18.72	
GaAs (100)	III054	18.73	
AlAs (100)	III027		72.70
AlAs (100)	III058		72.72

TABLE II. Measured Al 2p to Ga 3d core level binding energy differences for GaAs-AlAs (100) and AlAs-GaAs (100) heterojunctions.

Heterojunction	Sample	$E_{\text{Al}2p}^{\text{AlAs}} - E_{\text{Ga}3d}^{\text{GaAs}}$ (eV)
GaAs-AlAs (100)	III036	54.44
GaAs-AlAs (100)	III085	54.46
GaAs-AlAs (100)	III087	54.45
AlAs-GaAs (100)	III045	54.43
AlAs-GaAs (100)	III050	54.42

ojunction, in agreement with our result, but gave a value of 0.36 eV for the GaAs-AlAs (100) band offset. The latter result suggests that, for the GaAs-AlAs (100) system, differences in growth conditions between our samples and those of Waldrop *et al.* significantly influenced the quality of the interface.

Our measurement of the valence-band offset also gives results comparable to those obtained in electrical measurements. Using the charge transfer technique, Wang and Stern⁷ obtained a valence-band offset of 0.45 ± 0.05 eV, in excellent agreement with our results. Batey and Wright⁵ measured a valence-band offset of 0.55 eV by measuring the activation energy for thermionic emission of holes over an AlAs barrier; this value is somewhat higher than ours, but still approximately within the range of experimental error.

IV. CONCLUSIONS

We have measured the valence-band offset at the GaAs/AlAs (100) interface using XPS. Our measurements indicate that the band offset is commutative, and the value we obtain is $\Delta E_{\text{v}} = 0.46 \pm 0.07$ eV. This value is in good agreement with other XPS band offset measurements, as well as with electrical determinations of the GaAs/AlAs (100) valence-band offset. Our observation of commutativity is in agreement with some, but not all, published results for the GaAs/AlAs (100) interface. This indicates that we have been able to grow high-quality interfaces between GaAs and AlAs, since we expect commutativity in ideal interfaces, and suggests that commutativity of the band offset may safely be assumed in analyzing and designing quantum structures and devices.

ACKNOWLEDGMENTS

We would like to acknowledge useful discussions with T. K. Woodward, M. B. Johnson, J. O. McCaldin, and O. J. Marsh, and the valuable technical assistance of B. H. Cole. Discussions with R. W. Grant and J. R. Waldrop were especially helpful in the early phases of this work, particularly in assessing the influence of surface states on the analysis of the (100) GaAs valence-band spectra. One of us (E. T. Y.) is grateful for financial support from a National Science Foundation Graduate Fellowship. Part of this work was supported by the Office of Naval Research under Contract No. N00014-84-K-0501.

¹A. D. Katnani and R. S. Bauer, Phys. Rev. B 33, 1106 (1986).

²M. O. Watanabe, J. Yoshida, M. Mashita, T. Nakanishi, and A. Hojo, J. Appl. Phys. 57, 5340 (1985).

- ³J. R. Waldrop, S. P. Kowalczyk, R. W. Grant, E. A. Kraut, and D. L. Miller, *J. Vac. Sci. Technol.* **19**, 573 (1981).
⁴J. R. Waldrop, R. W. Grant, and E. A. Kraut, *J. Vac. Sci. Technol.* **B 5**, 1209 (1987).
⁵J. Batey and S. L. Wright, *J. Appl. Phys.* **59**, 200 (1986).
⁶G. Duggan, *J. Vac. Sci. Technol.* **B 3**, 1224 (1985).
⁷W. I. Wang and F. Stern, *J. Vac. Sci. Technol.* **B 3**, 1280 (1985).
⁸B. A. Wilson, P. Dawson, C. W. Tu, and R. C. Miller, *J. Vac. Sci. Technol.*

B 4, 1037 (1986).

- ⁹M. Hegema, in *The Technology and Physics of Molecular Beam Epitaxy*, edited by E. H. C. Parker (Plenum, New York, 1985), pp. 120-121.
¹⁰E. A. Kraut, R. W. Grant, J. R. Waldrop, and S. P. Kowalczyk, *Phys. Rev. B* **28**, 1965 (1983).
¹¹J. R. Chelikowsky and M. L. Cohen, *Phys. Rev. B* **14**, 556 (1976).
¹²P. K. Larsen, J. F. van der Veen, A. Mazur, J. Pollmann, J. H. Neave, and B. A. Joyce, *Phys. Rev. B* **26**, 3222 (1982).

APPENDIX 5

Finite-size effects in two-dimensional continuum percolation

W. J. Boudville and T. C. McGill

California Institute of Technology, Pasadena, California 91125

(Received 17 June 1988)

We have investigated the finite-size effects of anisotropic continuum percolation in two dimensions. The elements that percolate are widthless sticks. We have developed a simple theory to explain the dependence of longitudinal and transverse critical lengths on anisotropy and the finite number of sticks in the sample. By comparing the theory to simulations, we find good agreement.

I. INTRODUCTION

In recent years there has been interest in the electrical properties of composite materials consisting of conducting fibers or sticks, embedded in an insulating polymer matrix. Typically, the composites are prepared by mixing the fibers and polymer in a liquid state and letting the result cool while being poured. This leads to an angular distribution of the fibers in the solid state, about the flow direction. Experimentally, such composites are found to have a threshold dependence of the electrical conductivity on the fiber length.¹ Various models have been tried to explain such behavior. These include the effective medium theory.² This has not been very successful as there is a large difference between the conductivities of the fibers and the insulating polymer.³

More promising are percolation simulations. The first was done by Pike and Seager.⁴ They considered widthless (one-dimensional) sticks of constant length, in a two-dimensional medium, isotropic on a macroscopic scale. Their work was considerably extended by Balberg and Binenbaum⁵ to the case of anisotropic systems where, as mentioned above, the fibers have an average preferred orientation. They also considered various distributions of stick length. From their simulations, the critical stick lengths for percolation along the average stick orientation and transverse to this were found as functions of anisotropy (defined in Sec. II) and the number of sticks in the sample. However, due to computing constraints, they only considered a few random configurations of sticks. They showed that in the limit of an infinite ensemble of sticks, the longitudinal and transverse percolation thresholds converge to a common function. In this paper we wish to extend their work by considering more thoroughly the finite-size effects on the percolation thresholds of ensembles with small numbers of sticks. In Ref. 5 and other papers^{6,7} on continuum percolation this appears to have been a neglected point of interest. We will derive a simple model for the dependences of the thresholds on anisotropy and numbers of sticks and compare this to the results of extensive simulations.

Our paper is arranged as follows. Section II describes the simulations. Section III contains the model of the percolation thresholds. Section IV compares the model with the simulations. Finally, we give a conclusion in Sec. V.

II. SIMULATIONS

In this section we outline a method of performing simulations to find the critical lengths. (This is based on the procedure by Balberg and Binenbaum.⁵) First, we define the basic terms. Then, we give the procedure for obtaining the critical lengths.

To start, let us define some quantities. Consider a set of N widthless sticks. We place the centers of the sticks uniformly in the unit square, $[0,1] \times [0,1]$. The sticks have some angular probability distribution $f(\theta)$ about the y axis, where θ is the angle between a stick and the y direction. The angular distributions we consider all have the feature that

$$f(\theta) = f(-\theta), \quad \theta \in (0, \pi/2) \quad (1)$$

and that the average angle is $E[\theta] = 0$. The sticks' lengths are given by another probability distribution, $g(L)$. We assume θ and L to be independent. Given a random configuration of N sticks with lengths and angles $\{(L_i, \theta_i)\}$, the following quantities may be defined:

$$P_l \equiv \frac{1}{N} \sum_{i=1}^N L_i |\cos \theta_i| \quad (2a)$$

and

$$P_t \equiv \frac{1}{N} \sum_{i=1}^N L_i |\sin \theta_i|. \quad (2b)$$

These are the average longitudinal and transverse stick components with respect to the y direction, respectively. From these we define the macroscopic anisotropy as

$$P \equiv \frac{P_l}{P_t}. \quad (2c)$$

For an isotropic sample, we have $P = 1$. The larger P is, the more oriented the sticks are along the y direction. A given sample of sticks is considered to be percolating along the y direction if a continuous path can be traced between intersecting sticks from $y = 0$ to $y = 1$. Similarly for the x direction. The longitudinal critical length, L_{cl} is the lowest average length that gives the onset of y percolation. The transverse critical length, L_{ct} is likewise defined for x percolation.

We wish to investigate the dependences of L_{cl} and L_{ct}

on the anisotropy, P , and on the number of sticks in the system, N . First, consider systems with a given N . To vary the anisotropy, we change the variance of $f(\theta)$. For example, for a normal distribution of angles f is $N(0, \theta_d)$, where θ_d is the standard deviation. By progressively reducing θ_d from some initial value, we can correspondingly increase the anisotropy. Consider now that we have selected a variance of $f(\theta)$. We start with some small average value of L , $E[L]$. With the parameters of f and g chosen, 20 random configurations of sticks are generated, each with N sticks. We look for any percolation. Twenty random configurations at each value of anisotropy and $E[L]$ were made to increase the statistical reliability of finding accurate critical lengths. This is an improvement over Balberg and Binenbaum who presented critical lengths found from three to five configurations per value of anisotropy. Note that for sufficiently small $E[L]$, few of the sticks will overlap. Systematically, $E[L]$ is incremented until percolation is found. Often this is longitudinal percolation. This should be expected, as it is easier to percolate along a preferred direction than normal to it. (Occasionally, at low anisotropy, $P \leq 1.4$, we may first encounter transverse percolation.) By further incrementing $E[L]$, we eventually come upon transverse percolation. During the varying of $E[L]$ we record P for each random configuration. It is found that to good approximation, P is independent of $E[L]$. Our results and a comparison with the theory of Sec. III will be presented in Sec. IV.

III. THEORY

Here we present a simple model that attempts to explain the dependence of the longitudinal and transverse critical lengths on the anisotropy and the number of sticks in the ensemble. As before, let there be N sticks in the ensemble, with an angular distribution $f(\theta)$ and a stick length distribution $g(L)$. Our first approximation is to replace all the stick lengths L_i with the average length $L_0 \equiv \sum_i L_i / N$. Next, let us replace the angular distribution $f(\theta)$ by one in which half the sticks are oriented at θ' and the other half at $-\theta'$ with respect to the y axis, where θ' is defined by

$$\tan \theta' \equiv \frac{\langle |\sin \theta| \rangle}{\langle |\cos \theta| \rangle} = \frac{P_t}{P_l} \quad (3)$$

For definitiveness, we now look at longitudinal percolation. That is, we wish to find a set of overlapping sticks that goes from $y=0$ to $y=1$. Consider a stick at an angle θ' , labeled \overline{AC} in Fig. 1, where B is the center of the stick. The only sticks which can intersect \overline{AC} with nonzero probability are oriented at $-\theta'$. Furthermore, the centers of these sticks must lie in the parallelogram shown in Fig. 1. (Balberg *et al.*⁸ define this as the excluded area of the two sticks.) Suppose, in tracing out a possible cluster, that we started at $y=0$ and that \overline{AC} is the highest stick in the cluster, thus far. Let \overline{AC} be the j th stick in the cluster. To make progress towards $y=1$ we ask for the probability that a stick has a center in ΔHFG and is oriented at $-\theta'$. Remembering that the sticks are distributed uniformly, the probability is given by the

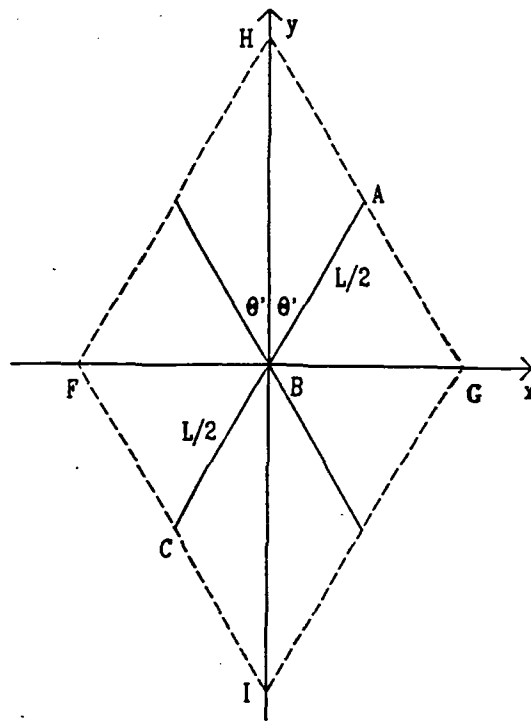


FIG. 1. A stick \overline{AC} of length L is at an angle θ' with respect to the y axis, where θ' is defined in Eq. (3). Sticks at an angle $-\theta'$, with centers inside the parallelogram $HFIG$ will intersect \overline{AC} .

product of the probability of one stick intersecting \overline{AC} with a higher y center times the number of such sticks. Thus we have

$$P_{j/2} \equiv A(\Delta HFG) \left[\frac{N}{2} - \frac{j}{2} \right] = P_l P_t \left[\frac{N}{2} - \frac{j}{2} \right], \quad (4)$$

where A is the area. [Since $P_{j/2}$ is a probability, if the right-hand side of Eq. (4) is greater than 1, we set $P_{j/2} = 1$.] Furthermore, if such an intersection occurs we see that the average y coordinate of the intersecting stick will be at a distance $P_t/3$ higher than the y coordinate of \overline{AC} 's center. Thus, the average number of intersections for y percolation is

$$n \equiv \frac{3}{P_l} \quad (5)$$

The probability of finding one percolating cluster in the y direction is given by the product of n terms of the form of Eq. (4), which we can write as

$$P_{\text{cluster}}^y = \prod_{j=1}^{n/2} P_j^2, \quad (6)$$

where from Eq. (4), P_j is defined as

$$P_j \equiv \begin{cases} a_j, & a_j \leq 1 \\ 1, & a_j > 1 \end{cases} \quad (7)$$

and

$$a_j \equiv P_i P_l \left[\frac{N}{2} - j \right]. \quad (8)$$

Note that in Eq. (6) we have assumed that n is even. If n is odd, Eq. (6) is multiplied by $P_{n/2+1}$.

Equation (6) gives the probability of forming one cluster. However, it may be possible for several clusters to form, especially for longitudinal percolation in highly anisotropic samples. As mentioned above, the y coordinate of the intersecting stick in the cluster is at an average distance of $P_l/3$ higher. For the x coordinate of the intersecting stick, averaging over ΔHFG gives 0. This comes from

$$P(x < x_B) = P(x > x_B) = \frac{1}{2},$$

where P is the probability function. But, we see that the average x coordinate of the interesting stick is $P_l/3$, assuming that $x > x_B$, and it is $-P_l/3$ if $x < x_B$. Hence, for longitudinal percolation we have a random walk in the x direction, of average step size $P_l/3$ and equal probability of stepping positive or negative. From Eq. (5), it takes n steps to percolate in the y direction. During these steps, the cluster will span an approximate distance⁹ in the x direction of

$$v_0 \equiv \sqrt{n} \frac{P_l}{3}. \quad (9)$$

Since we are bounded by 0 and 1 in the x direction, let

$$v = \begin{cases} v_0, & v_0 \leq 1 \\ 1, & v_0 > 1 \end{cases} \quad (10)$$

Then v is the fractional transverse distance covered when we are looking at longitudinal percolation. Therefore, the total probability for a longitudinal percolating cluster is given by dividing Eq. (6) by v to give

$$P_{\text{tot}} = \frac{1}{v} P_{\text{cluster}}^l. \quad (11)$$

To find transverse percolation, we merely interchange P_l and P_i in the above equations. Given values for $\langle |\sin\theta| \rangle$ and $\langle |\cos\theta| \rangle$, we can use the above equations to find the critical lengths and the anisotropy.

One further matter needs to be addressed. Given a $\langle |\cos\theta| \rangle$, which is defined by a particular $f(\theta)$ and a choice of variance of f , there corresponds a unique $\langle |\sin\theta| \rangle$. But for the set of arbitrary probability distributions f , subject to the constraints of Eq. (1), there will be no unique relation between $\langle |\cos\theta| \rangle$ and $\langle |\sin\theta| \rangle$. How can we find an anisotropy that is in some sense independent of a particular f ? To answer this, note that we have the following inequalities:

$$0 \leq \langle |\cos\theta| \rangle, \quad \langle |\sin\theta| \rangle \leq 1 \quad (12a)$$

and

$$1 \leq d \leq 2, \quad (12b)$$

where

$$d \equiv \langle |\cos\theta| \rangle + \langle |\sin\theta| \rangle, \quad (12c)$$

and the triangle inequality was used to get the lower bound of Eq. (12b). We do the following. A value of d is chosen to satisfy Eq. (12b). We then vary $\langle |\sin\theta| \rangle$ in steps, starting from $d/2$ and decrementing to 0 (though not going all the way). Then $\langle |\cos\theta| \rangle$ is given by

$$\langle |\sin\theta| \rangle = \begin{cases} d - \langle |\sin\theta| \rangle, & d - \langle |\sin\theta| \rangle \leq 1 \\ 1, & d - \langle |\sin\theta| \rangle > 1. \end{cases} \quad (13)$$

With these values, we can find the anisotropy and use Eq. (11) to obtain the critical lengths. We choose 1.5, the midpoint of Eq. (12b), as the most reasonable value of d . It should be realized that the procedure of using Eqs. (12c) and (13) is an approximation. In general, a given f will not yield $\langle |\cos\theta| \rangle$ and $\langle |\sin\theta| \rangle$ satisfying the linear relationship of Eq. (12c) over a range of values of the variance.

A program was written to find the lowest lengths that set $P_{\text{tot}} \geq$ in Eq. (11) as a function of anisotropy, for both longitudinal and transverse percolation. These are the critical lengths. The number of sticks in the sample was a parameter in this calculation.

IV. RESULTS

Here we present and compare the results of Sec. II and III. First, let us consider the predictions of the model of the preceding section. The values of critical lengths from Eq. (11) are displayed in Figs. 2 and 3 for 100 and 500 sticks, respectively. In each figure, the solid line is for longitudinal percolation while the dashed line is for transverse percolation. Following Balberg and Binenbaum,⁵ we have normalized the critical lengths in units of the average interstick separation, r , where

$$r \equiv \frac{1}{\sqrt{\pi N}}. \quad (14)$$

From the simulations we have found the critical lengths L_{cl} , L_{ct} as functions of anisotropy, for ensembles of 100 and 500 sticks. These are displayed in Figs. 2 and 3, respectively. For Fig. 2, we have found the critical lengths for three types of ensembles: Those with normal distributions for f and g ; with a uniform f and a normal g ; and with constant absolute angle and a δ function for g (i.e., all the sticks in an ensemble are the same length). This last pair of distributions corresponds to the simplified choices of distributions made in Sec. III. Similar remarks hold for Fig. 3. The solid objects in the figures are the critical longitudinal lengths. The hollow objects are the critical transverse lengths.

We see from Figs. 2 and 3 that for both the simulations and the theory the transverse critical lengths lie distinctly above the longitudinal critical lengths. Considering separately the transverse and longitudinal results, we see that the simulations with constant length and absolute angle tend to yield larger critical lengths than the other simulations. This is expected,⁵ as a distribution of lengths will cause the sticks with lengths greater than the mean length to contribute preferentially to the percolation. Hence percolation will start sooner than if all the lengths in a sample are constant. Nonetheless, the simulation re-

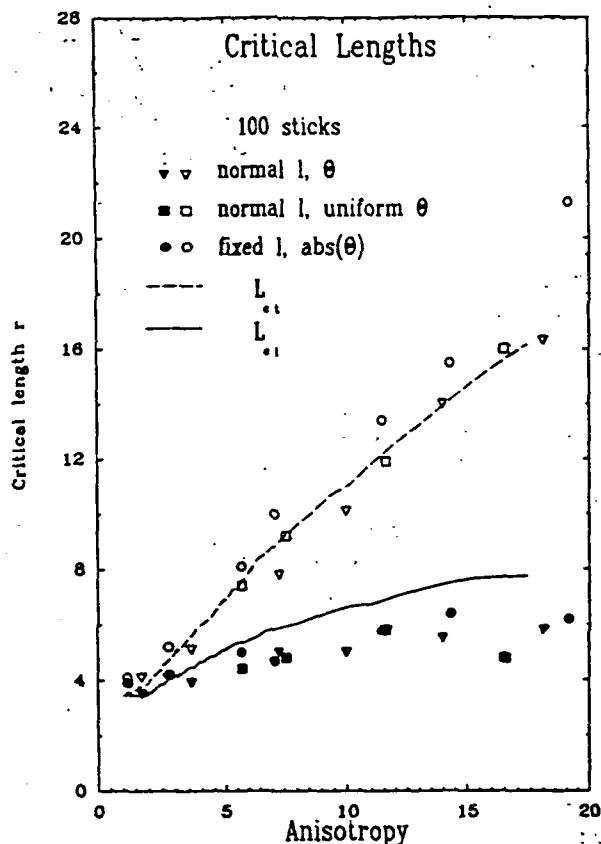


FIG. 2. The critical lengths as a function of anisotropy for samples of 100 sticks. The anisotropy is defined in Eq. (2). The solid and open symbols are from simulations for longitudinal and transverse percolation, respectively. The lines are from Eq. (11).

sults for transverse percolation are clustered close enough, and likewise for longitudinal percolation, that we find a universal behavior of the critical lengths on the anisotropy that is largely independent of the choice of distributions. Comparing the theory with the simulations, we see good agreement for both 100 and 500 sticks. The largest disagreement is for the longitudinal percolation of 100 sticks, with the theory lying above the simulations. But even here, the theoretical curve exhibits the same trends as the simulations and the disagreement is only semiquantitative.

Note that in comparing Figs. 2 and 3, the longitudinal and transverse results tend to converge together as we go from 100 sticks to 500 sticks. This is in accordance with Balberg and Binenbaum⁷ who showed by a topological argument that in the limit of infinite N , the two types of critical lengths coincide.

Let us add a comment about the midrange choice of $d=1.5$ made in Eqs. (12) and (13) in the preceding section. This was done to give a definite prescription for the anisotropy. If we set d equal to the lower limit, 1, we get curves that start at a critical length around 5 at isotropy, and remain above the displayed curves as we increase the anisotropy. This was found for both longitudinal and

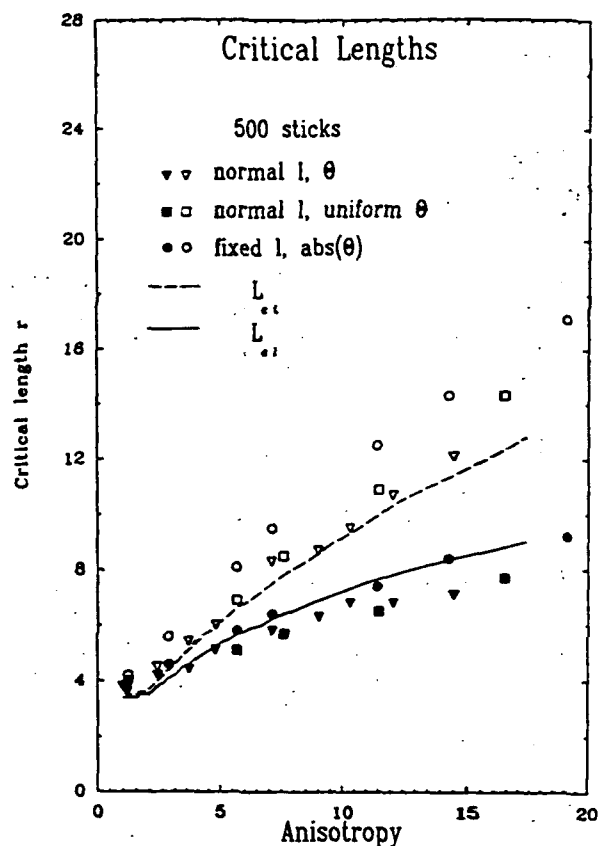


FIG. 3. The critical lengths as a function of anisotropy for samples of 500 sticks. The anisotropy is defined in Eq. (2). The solid and open symbols are from simulations for longitudinal and transverse percolation, respectively. The lines are from Eq. (11).

transverse percolation. The agreement between the (undisplayed) $d=1$ curves and the simulations is not as good as for the $d=1.5$ curves shown here in Figs. 2 and 3. Alternatively, choosing d equal to the upper limit of 2 gives curves that start and remain slightly lower than the displayed curves. Hence, we believe our choice of $d=1.5$ to be a reasonable one.

Therefore, we suggest that our theory of Sec. III gives good predictions of critical length. The theory also has the computational advantage of being much faster to run. The curves in Figs. 2 and 3 took less than a minute of CPU (central-processing-unit) time each to find, on a VAX 11/785. By contrast, the CPU time for the simulations is measured in hours. This is especially true for the simulations of 500 sticks. The CPU time required scales roughly as the square of the number of sticks, as the most intensive task is to find the possible intersections amongst N sticks.

V. CONCLUSION

We have investigated the finite-size effects of anisotropic continuum percolation in two dimensions. The elements that percolate are widthless sticks. We have

developed a simple theory to explain the dependence of longitudinal and transverse critical lengths on anisotropy and the finite number of sticks in the sample. By comparing the theory to simulations, we find good agreement. It also affords significant computational advantages over performing simulations. We believe that our theory is the first to explain the finite-size simulation results for anisotropic continuum percolation in two dimensions.

Thus, we suggest that the theory offers a useful complement to the running of simulations.

ACKNOWLEDGMENTS

We would like to gratefully acknowledge the support of the Office of Naval Research under Contract No. N00014-84-K-0501. One of us (W.J.B) is the recipient of support from the IBM Corporation.

¹D. M. Bigg, *Polym. Eng. Sci.* 19, 1188 (1979).

²H. Hatta and M. Taya, *J. Appl. Phys.* 58, 2478 (1985).

³N. Ueda and M. Taya, *J. Appl. Phys.* 60, 459 (1986).

⁴G. E. Pike and C. H. Seager, *Phys. Rev. B* 10, 1421 (1974).

⁵I. Balberg and N. Binenbaum, *Phys. Rev. B* 28, 3799 (1983).

⁶I. Balberg, *Phys. Rev. B* 31, 4053 (1985).

⁷L. W. Noh, S. Lee, Y. Song, and J. R. Gaines, *Phys. Lett.* 114A, 207 (1986).

⁸I. Balberg, C. H. Anderson, S. Alexander, and N. Wagner, *Phys. Rev. B* 30, 3933 (1984).

⁹R. Reif, *Fundamentals of Statistical and Thermal Physics* (McGraw-Hill, New York, 1965).

APPENDIX 6

Electron tunneling time measured by photoluminescence excitation correlation spectroscopy

M. K. Jackson, M. B. Johnson, D. H. Chow, and T. C. McGill
T. J. Watson, Sr., Laboratory of Applied Physics, California Institute of Technology, Pasadena,
California 91125

C. W. Nieh
Keck Laboratory of Materials Engineering, California Institute of Technology, Pasadena, California 91125

(Received 16 September 1988; accepted for publication 22 November 1988)

The tunneling time for electrons to escape from the lowest quasibound state in the quantum wells of GaAs/AlAs/GaAs/AlAs/GaAs double-barrier heterostructures with barriers between 16 and 62 Å has been measured at 80 K using photoluminescence excitation correlation spectroscopy. The decay time for samples with barrier thicknesses from 16 Å (≈ 12 ps) to 34 Å (≈ 800 ps) depends exponentially on barrier thickness, in good agreement with calculations of electron tunneling time derived from the energy width of the resonance. Electron and heavy hole carrier densities are observed to decay at the same rate, indicating a coupling between the two decay processes.

The electrical properties of the double-barrier (DB) heterostructure have been of great interest since its proposal by Tsu and Esaki.¹ The desire to characterize the high-frequency behavior of the DB stems from interest in its use as an oscillator² and as a switching element.^{3,4} However, the time associated with the tunneling of electrons has been the subject of more than 20 years of discussion.⁵⁻⁹ Experimental measurements of tunneling times have required the development of high-speed measurement techniques. Recently, two groups have reported experimental studies of the temporal response of DB structures. Whitaker *et al.*¹⁰ have used electro-optic sampling measurements to study a single tunnel device. Tsuchiya *et al.*¹¹ used the photoluminescence (PL) from carriers in the quasibound states in the quantum well to study the decay of the electron population in the quantum well as a function of the barrier thickness. However, the experiments of Ref. 11 were limited to times greater than 60 ps, and Guo *et al.*⁹ have raised some serious questions about the theoretical calculations that were used for comparison with experimental results.

In this letter we report a study of the decay of photoexcited carriers in double-barrier heterostructures as a function of the thickness of the barrier layers. By employing an excitation correlation method¹² we have extended the results of Tsuchiya *et al.*¹¹ to significantly shorter times and are comparing our data with results of corrected calculations of the tunneling times.

Double-barrier (DB) structures were grown on (100) GaAs substrates by molecular beam epitaxy in a Perkin-Elmer 430 system at 600 °C. After growth of 0.5 μm of GaAs, a superlattice buffer layer consisting of five periods of 50 Å $\text{Al}_{0.35}\text{Ga}_{0.65}\text{As}/500$ Å GaAs was grown. This was followed by growth of a 0.7 μm layer of GaAs, which provided a high quality layer on which to grow the DB and eliminated any optical effects from the superlattice. Then a symmetrical GaAs/AlAs/GaAs/AlAs/GaAs DB was grown, with a well thickness of 58 Å. The final layer was a 300 Å GaAs cap. All layers were nominally undoped with an estimated residual carbon acceptor concentration of 10^{14} cm^{-3} . Seven samples were studied, with bulk growth rate information pre-

dicting barrier thicknesses of 16, 22, 28, 34, 34, 48, and 62 Å. High-resolution transmission electron microscopy confirmed the barrier thicknesses of the 16 Å sample and one of the 34 Å samples, within an uncertainty of two monolayers. We estimate an uncertainty in barrier thickness of two monolayers for all of the samples.

The experimental technique has been described previously.¹² A colliding pulse mode-locked ring dye laser is used to generate a train of pulses 200 fs full width at half maximum (FWHM), at a repetition frequency of 120 MHz. The laser output is centered at 6200 Å and has a spectral width of 20 Å FWHM. The pulse train is equally divided into two separate beams which are independently chopped at $f_1 = 1600$ Hz and $f_2 = 2100$ Hz, and delayed with respect to one another by time γ ($-500 < \gamma < 500$ ps) before being recombined and focused to a 25- μm -diam spot on the surface of the sample. The typical average power used was 1 mW per beam before chopping. The PL is spectrally resolved, and detected by a GaAs photomultiplier tube (PMT). After amplification, the PMT signal is synchronously detected by a lock-in amplifier at either the fundamental frequency f_1 or at the sum frequency $f_{\text{sum}} = f_1 + f_2$. All of the results reported here were taken with the sample at 80 K.

In Fig. 1 we present a schematic diagram of the pro-

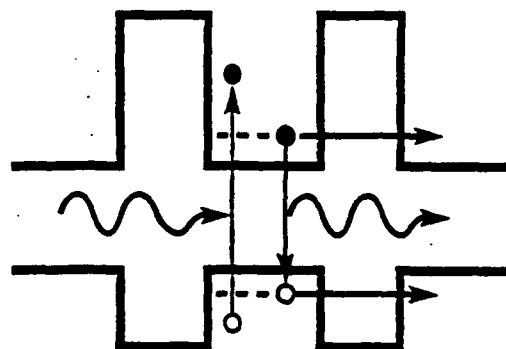


FIG. 1. Schematic diagram of relevant carrier processes involved in the double-barrier samples during the experiment. Shown are photoexcitation of carriers in the well, tunneling of carriers out of the well, and recombination of carriers in the well.

cesses of excitation, tunneling from the well, and the radiative recombination of carriers within the well. Recent observations of the thermalization times of electrons between subbands have given times less than 200 fs.¹³ Hence we will assume that the thermalization of electrons and holes to the lowest subband to be fast compared to the times of interest here. A model of the measurement process has been given in Ref. 12. We will simply sketch the important results. If the electron and hole populations created by an optical pulse are $n(t)$ and $p(t)$, and the populations created by two optical pulses are independent, then the sum frequency signal I_{sum} is proportional to the cross correlation

$$I_{\text{sum}}(\gamma) \propto \int [n(t)p(t-\gamma) + n(t-\gamma)p(t)] dt.$$

This signal is due to the recombination of electrons created by the first pulse with holes created by the second pulse, and vice versa. If we assume that the electron and heavy hole densities decay exponentially⁷ with time constants τ_e and τ_{hh} , respectively, then the sum frequency signal is proportional to the sum of two exponentials

$$I_{\text{sum}}(\gamma) \propto [\exp(-|\gamma|/\tau_e) + \exp(-|\gamma|/\tau_{hh})]. \quad (1)$$

We have used this result as the basis for interpreting our data.

In Fig. 2 we present typical photoluminescence spectra taken at 80 K at the fundamental and sum chopping frequencies. The spectrum at the fundamental frequency consists of a single distinguishable feature centered at 7650 Å. The wavelength of the feature in the fundamental frequency spectrum is in approximate agreement with the calculated position of 7730 Å for transition from the lowest electron subband to the lowest heavy hole subband in a 58 Å quantum well. The peak of the corresponding feature in the sum frequency spectrum is shifted slightly to longer wavelengths. We do not, at present, have an explanation for this shift.

In Fig. 3 we present a semilogarithmic plot of a typical scan of the photoluminescence at the sum chopping frequency as a function of the time delay between the two pulses. The scan was taken at 80 K, at a wavelength of 7665 Å, the peak of the sum PL spectrum shown in Fig. 2. This delay scan consists of a peak at zero delay with wings extending to much longer times. The peak at $\gamma = 0$ is a coherence peak due to

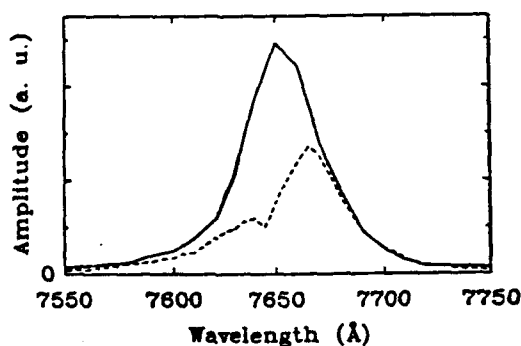


FIG. 2. Typical excitation correlated luminescence for 28 Å barrier sample at 80 K. Shown are luminescence signals at the fundamental chopping frequency (solid line) and the sum frequency (dashed line). Both scans were taken with delay $\gamma = 0$. The sum frequency spectrum has been multiplied by 2.

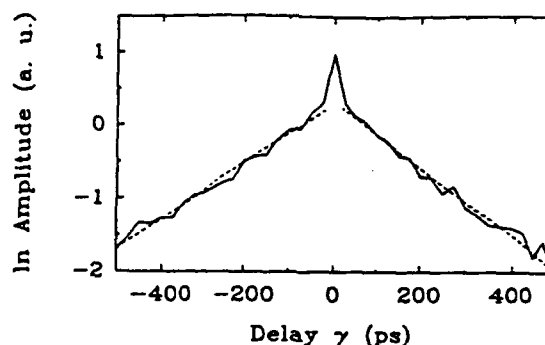


FIG. 3. Semilogarithmic plot of the variation of the sum frequency luminescence signal (solid line) with delay γ . The sample is the same as in Fig. 2. The scan was taken at 7665 Å, the peak of the sum frequency spectrum. The coherence peak at $\gamma = 0$ is not resolved in this scan. The dashed lines are the fits discussed in the text, which give a decay time of 236 ± 20 ps.

the optical interference of the two incident pulses on the sample and is not resolved in this scan. A single exponential fits the wings in the sum frequency delay scan shown in Fig. 3. Delay scans for one sample, taken at 4 K, show evidence of a second exponential with a faster decay. Fits to the sum frequency delay data at 80 K using a single exponential are shown as dashed lines in Fig. 3. The coherence peak is not included in fitting the delay scans.

In Fig. 4 we have plotted the exponential decay time at 80 K as a function of barrier thickness for the seven samples described above. The decay time depends exponentially on barrier thickness for barriers up to approximately 34 Å. Over this range of exponential dependence the decay time varies by two orders of magnitude. For thicker barriers the decay time seems to approach a value that is independent of the barrier thickness. With the 120 MHz repetition rate of the excitation pulses, there is an upper limit on the order of 2 ns to the decay times that can be measured accurately with our technique. Consequently, the result for the sample with a barrier thickness of 62 Å should be viewed with some cau-

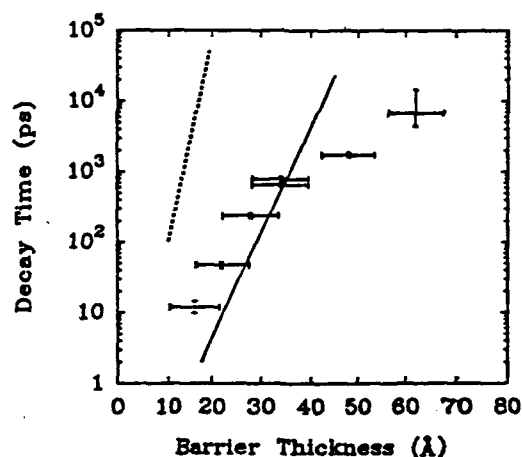


FIG. 4. Measured decay times as a function of barrier thickness. The data points are the measured decay times, with error bars on the thickness based on uncertainty in the barrier thickness and error bars on the decay times from uncertainties in the fits to the delay scans. The solid line is the electron tunneling time calculated from the width of the lowest conduction-band transmission resonance, using a two-band expression for the wave vector in AlAs barriers. The dashed line shows the tunneling time for heavy holes and was calculated using a one-band expression for the barrier wave vector.

tion. Our measured decay times are about a factor of 4 longer than those of Tsuchiya *et al.*¹¹

In Fig. 4 we have also plotted the time calculated for electrons and heavy holes to tunnel out of the quantum well. The solid line is the electron tunneling time, and the dashed line is the heavy hole tunneling time. We will assume that the light holes thermalize to become heavy holes on a time scale short compared to times of interest here. From Ref. 7 the time for a particle to tunnel out of a quasibound state in the quantum well is related to the energy width of the corresponding resonance in the transmission probability by $\tau = \hbar/\Delta E_{\text{FWHM}}$. The transmission probability is calculated using the transfer matrix approach of Kane,¹⁴ modified to account for the different effective masses of the particle in the quantum well and in the barrier.

For electrons, we have considered only Γ -point barriers. It is appropriate to use a simple one-band expression for the wave vector in the well, $k = (2m_w^* m_e E / \hbar^2)^{1/2}$, where m_w^* is the effective mass in the GaAs well, m_e is the free-electron mass, and E is the energy of the particle with respect to the GaAs band edge. With the pure AlAs barriers in our samples, the lowest quasibound electron state has an energy far from the band edge in the AlAs barriers. Hence we have used a two-band model¹⁵ to calculate the wave vector in the barriers. The barrier height used in these calculations was 1.07 eV, corresponding to a valence-band offset of 0.55 eV¹⁶ and an AlAs band gap of 3.13 eV. The effective masses in the well and the barriers were taken to be $0.067m_e$ and $0.15m_e$, respectively.¹⁷ For the heavy holes, we used a one-band expression to estimate the wave vector in the barriers. From the theoretical curves in Fig. 4, we can see that the tunneling time for electrons is much shorter than that for heavy holes.

Comparing these theoretical estimates of the tunneling times with the decay times observed experimentally, we note that the decay times agree well with the shorter tunneling time of the electrons. In contrast, if we expected Eq. (1) to explain the data, then we should observe two decay times, a short one near zero delay and a longer time at much longer delays. We might expect the longer decay time to be that for the heavy holes. There are a number of phenomena that could contribute to the observation of a single time that is close to the electron tunneling time. First, with the widely differing decay rates for electrons and heavy holes, it is very likely that the quantum well becomes charged. Rapidly escaping electrons could leave slowly decaying holes behind. The areal densities of holes and electrons produced in our experiment are roughly 10^{11} cm^{-2} , which are high compared to the background doping of 10^8 cm^{-2} . These areal densities produced by the photoexcitation could result in very substantial amounts of band bending. We would expect the potential across the barriers due to charging created by the differences in escape rates to increase the tunneling escape rate for holes. This effect would tend to make the electron and hole densities in the well follow each other and produce a decrease in the tunneling time for holes. Second, at higher temperatures, we would expect significant occupancy of the lowest light hole subband. The tunneling time for the

light holes is even shorter than that for electrons and, hence, could offer an escape channel for the heavy holes. This phenomenon could be responsible for the changes in the observed delay scans with temperature. Finally, if we couple the finite spot size of the laser with the variations in decay rates, we might expect density gradients and electric fields to develop in the plane of the quantum wells. These density gradients and electric fields could act to make the hole density follow the electron density by inducing hole transport in the plane of the quantum well. We are attempting to carry out a detailed numerical simulation of this complex problem which will be important in understanding the results of any of the measurements reported to date that are based on optical excitation.

In summary, the tunneling time for electrons to escape from the lowest quasibound state in the quantum wells of GaAs/AlAs/GaAs/AlAs/GaAs double-barrier heterostructures has been measured at 80 K using the technique of photoluminescence excitation correlation spectroscopy. Results are in good agreement with calculations of electron tunneling time based on the energy width of the resonance in the transmission coefficient.

The authors would like to thank R. Miles, Y. Rajakarunanyake, D. Ting, E. Yu, and A. T. Hunter for helpful discussions. This work was supported in part by the Office of Naval Research under contract No. N00014-84-K-0501, the Defense Advanced Research Projects Agency under contract No. N00014-84-C-0083, and the National Science Foundation under grant No. NMR8421119. Two of us (M. K. J. and D. H. C.) would like to acknowledge financial support from the Natural Sciences and Engineering Research Council of Canada, and International Business Machines Corporation, respectively.

¹R. Tsu and L. Esaki, *Appl. Phys. Lett.* **22**, 562 (1973).

²T. C. L. G. Sollner, W. D. Goodhue, P. E. Tannenwald, C. D. Parker, and D. D. Peck, *Appl. Phys. Lett.* **43**, 588 (1983).

³T. K. Woodward, T. C. McGill, H. F. Chung, and R. D. Burnham, *IEEE Electron Device Lett.* **9**, 122 (1988).

⁴F. Capasso, K. Mohammed, and A. Y. Cho, *IEEE J. Quantum Electron.* **QE-22**, 1853 (1986).

⁵K. K. Thornber, T. C. McGill, and C. A. Mead, *J. Appl. Phys.* **38**, 2384 (1967).

⁶M. Büttiker and R. Landauer, *Phys. Rev. Lett.* **49**, 1739 (1982).

⁷N. Harada and S. Kuroda, *Jpn. J. Appl. Phys.*, Pt. 2 **25**, L871 (1986).

⁸S. Collins, D. Lowe, and J. R. Barker, *J. Phys. C* **20**, 6213 (1987).

⁹H. Guo, K. Diff, G. Neofotistos, and J. D. Gunton, *Appl. Phys. Lett.* **53**, 131 (1988).

¹⁰J. F. Whitaker, G. A. Mourou, T. C. L. G. Sollner, and W. D. Goodhue, *Appl. Phys. Lett.* **53**, 385 (1988).

¹¹M. Tsuchiya, T. Matsusue, and H. Sakaki, *Phys. Rev. Lett.* **59**, 2356 (1987).

¹²M. B. Johnson, T. C. McGill, and A. T. Hunter, *J. Appl. Phys.* **63**, 2077 (1988).

¹³K.-K. Choi, B. F. Levine, C. G. Bethea, J. Walker, and R. J. Malik, *Appl. Phys. Lett.* **50**, 1814 (1987).

¹⁴E. O. Kane, in *Tunneling Phenomena in Solids*, edited by E. Burstein and S. Lundqvist (Plenum, New York, 1969), p. 1.

¹⁵E. O. Kane, in *Physics of III-V Compounds*, edited by A. C. Beer and R. K. Willardson (Academic, New York, 1966), Vol. 1, p. 75.

¹⁶J. Batey and S. L. Wright, *J. Appl. Phys.* **59**, 200 (1986).

¹⁷S. Adachi, *J. Appl. Phys.* **58**, R1 (1985).

APPENDIX 7

Theoretical investigation of the effect of strain on phase separation in epitaxial layers

A. Zur and T. C. McGill

The T. J. Watson Sr. Laboratory of Applied Physics, California Institute of Technology, Pasadena, California 91125

(Received 14 February 1985; accepted 18 April 1985)

We have theoretically investigated the phenomenon of alloy clustering in epitaxial films and, in particular, the case of $\text{Al}_x\text{Ga}_{1-x}\text{As}$ grown epitaxially on GaAs. We show in the general case that the elastic strain in the film, caused by the finite mismatch between the lattice parameters of the film and the substrate, may change the miscibility properties of the film. A miscibility gap could be opened in the material composing the film, even if there is no such gap in the bulk material. Conversely, the strain could stabilize a solid solution in the film in cases where there is a miscibility gap in the bulk material of which the film is composed. We estimate that these effects are too small to account for phase separation in the case of $\text{Al}_x\text{Ga}_{1-x}\text{As}$ on GaAs, but could be important in other systems, such as $\text{In}(\text{As}, \text{Sb})$.

I. INTRODUCTION

Devices consisting of epitaxial layers of $\text{Al}_x\text{Ga}_{1-x}\text{As}$ grown on GaAs substrate have gained prominence in electronic and optoelectronic research.¹ In many cases, the performance of such devices depends on controlling the composition of the epitaxial layer (the x in $\text{Al}_x\text{Ga}_{1-x}\text{As}$). In recent years, several experimental papers have been published, indicating that under certain growth conditions, the composition of the epitaxial layer is not uniform. Holonyak *et al.*² observed photoluminescence features that were compatible with alloy clustering in MOCVD samples of $\text{Al}_x\text{Ga}_{1-x}\text{As}$ grown on GaAs. Petroff *et al.*³ have observed alternating layers of Al- and Ga-rich $\text{Al}_x\text{Ga}_{1-x}\text{As}$ in MBE samples grown on GaAs(110). These layers were parallel to the interface, about 100 Å thick, and the variation in composition was estimated by Petroff *et al.* to be at least 5%. These results are somewhat surprising in light of the fact that bulk $\text{Al}_x\text{Ga}_{1-x}\text{As}$ is known not to have a miscibility gap.⁴

Several possible mechanisms could lead to the clustering in the epitaxial layer. First, the relatively low growth temperature suggests that the observed clustering could be metastable; that would not explain how the clustering forms, only why it is observed. Second, the observed clustering could be stable in bulk $\text{Al}_x\text{Ga}_{1-x}\text{As}$ at low temperatures, and the thermodynamical data (obtained from high temperature experiments) should be reevaluated for low temperatures. Third, the clustering was only observed in thin films grown epitaxially on a GaAs substrate; the clustering may, therefore, be induced by substrate

In this paper we examine this third possibility, namely, that the substrate induces the clustering. We investigate the effects of the strain in the film, induced by the substrate, on the miscibility properties of the film. (This mechanism was proposed by Maximov⁵ to explain clustering effects in $\text{GaAs}_x\text{P}_{1-x}$.) We conclude that the strain term could, in general, change these miscibility properties, i.e., a miscibility gap could be either opened or closed by the strain. To be more specific, in the case of a particular system like $\text{Al}_x\text{Ga}_{1-x}\text{As}$ on GaAs, we have to know the elastic constants of the film over the entire composition range. So far,

these elastic constants have not been measured for any of the III-V ternary systems.

This paper is organized as follows. In Sec. II, following this introduction, we discuss the effects of strain on phase separation in the epitaxial layer. The treatment is rather general in that section. In Sec. III, we consider some III-V systems in which the strain in the film (induced by the substrate) may change the miscibility properties of the film. In Sec. IV, we attempt to estimate the relevant parameters for the particular case of $\text{Al}_x\text{Ga}_{1-x}\text{As}$ on GaAs. Our estimates of the relevant parameters would indicate that the strain term is too small to open a miscibility gap in the $\text{Al}_x\text{Ga}_{1-x}\text{As}$ film, suggesting that the observed clustering is metastable. In Sec. V, we draw conclusions based on our study.

II. EFFECTS OF STRAIN ON PHASE SEPARATION

In this section we estimate the excess free energy of an epitaxial film due to the induced elastic strain. We will show that this excess free energy may have both positive and negative second derivatives with respect to the alloy composition (in the general case of a film composed of a binary or a pseudobinary alloy). This would imply that the strain in the epitaxial layer may in some cases stabilize and in others destabilize clustering. The magnitude of this excess free energy depends on the elastic constants of the alloy, as well as on the lattice mismatch. If the lattice mismatch is too small, the extra stabilization (or destabilization) of the clustering, resulting from the elastic strain, could be negligible compared to the enthalpy and entropy of mixing. In Sec. IV, we will estimate that this is the case in $\text{Al}_x\text{Ga}_{1-x}\text{As}$ grown on GaAs.

When there is a mismatch between the lattice parameters of the substrate and the film, strain effects are observed in the crystal. When the epitaxial film is very thin, it is energetically favorable for the film to be strained uniformly, such that it adopts the lattice parameters of the substrate parallel to the interface. No bonds have to be broken in this case, but the elastic strain energy accumulates as the film grows thicker and thicker. At some critical thickness, misfit dislocations

would relieve part of this strain (see, for example, van der Merwe and Ball⁶ and references therein). In our treatment here, we should only treat the case of a thin film, having no misfit dislocations.

When the film adopts the lattice parameters of the substrate, its elastic strain energy is given by Hook's law

$$\Delta E = \frac{1}{2} V C f^2, \quad (1)$$

where V is the volume of the film, C is some elastic constant of the film, and f is the strain in the film. The strain energy ΔE in Eq. (1) could depend on the composition x of the alloy. For discussing phase separation, we have to consider only the second derivative of the energy with respect to composition. Constant and linear terms in composition would not alter the total energy of the system upon either separation or mixing. If the second derivative of the strain energy with respect to x is positive, the strain would drive the system toward mixing, if it is negative, toward phase separation. The strain energy is only part of the total free energy, which also includes enthalpy of formation (the linear part of the enthalpy), enthalpy of mixing (the nonlinear part), and entropy of mixing terms. Consequently, the driving toward phase separation or mixing due to strain competes with the driving toward separation or mixing due to the other terms. One can see, however, that the sign of the curvature of the free energy could sometimes be reversed by the strain term. For example, in the vicinity of coexistence points, where the curvature of the bulk free energy is zero, it is the elastic strain term that could make the difference.

In our treatment, we assume a general model of a binary, or a pseudobinary alloy, say $A_{1-x}B_x$. We further assume that this alloy is grown on a substrate consisting of one of the two materials that form the alloy (say A). In our notation, therefore, when $x = 0$ the film composition is identical to that of the substrate. The composition dependence of the strain energy comes, in this case, from the composition dependence of the three terms in Eq. (1), namely V , C , and f . Usually, the materials in question are nearly lattice matched, and, therefore, the specific volume is almost independent of composition. We shall assume, therefore, that the film volume V in Eq. (1) is independent of composition. The second term in Eq. (1), C , can be expressed in terms of the usual elastic constants of the film and depends on the crystal direction of the epitaxy. In the case of a cubic film grown on a cubic substrate, C is given by⁵

$$C = \begin{cases} 2C_{11} + 2C_{12} - \frac{4C_{12}^2}{C_{11}} & \text{for (100)/(100)} \\ \frac{12C_{44}(C_{11} + 2C_{12})}{C_{11} + 2C_{12} + 4C_{44}} & \text{for (111)/(111)} \end{cases} \quad (2)$$

The composition dependence of C can be calculated from the composition dependence of C_{11} , C_{12} , and C_{44} . Finally, the composition dependence of the strain is linear, according to Vegard's law. Therefore, if Δa is the difference between the lattice parameters of the two end materials which form the alloy, then

$$\Delta E = V \left(\frac{\Delta a}{a} \right)^2 \cdot \frac{1}{2} C(x) x^2. \quad (3)$$

In Eq. (3), the compositional dependence of the strain energy

is lumped in the term $C(x)x^2$. It should be emphasized here that this term may have a second derivative with respect to x of both positive and negative sign. To demonstrate this, assume that $C(x)$ is a linear function of the composition

$$C(x) = C_0(1 - x) + C_1x. \quad (4)$$

In that case, the second derivative of $C(x)x^2$ is also a linear function of x :

$$\frac{\partial^2}{\partial x^2} [C(x)x^2] = 2C_0(1 - x) + (6C_1 - 4C_0)x. \quad (5)$$

Therefore, in this example, $C(x)x^2$ always curves upward for small values of x but may curve downward near $x = 1$ if the slope of $C(x)$ is negative enough ($C_1 < \frac{2}{3}C_0$).

III. TERNARY III-V SYSTEMS

As we have mentioned in the previous section, the energy term due to strain in the film has to compete with the bulk terms (enthalpy and entropy of mixing) in the film material. While exact numbers are not available in most cases, we would like to estimate the order of magnitude of each of these terms.

The entropy-of-mixing term dominates the free energy at high temperatures. In many of the III-V ternary systems, the entropy of mixing can be approximated by assuming that the solution is ideal:

$$S_m = -Nk [x \log x + (1 - x) \log(1 - x)], \quad (6)$$

where N is the number of formula units. Taking the second derivative of Eq. (6) with respect to concentration

$$\frac{\partial^2 S_m}{\partial x^2} = -Nk \left[\frac{1}{x} + \frac{1}{1-x} \right] < -4Nk. \quad (7)$$

$4kT$ is approximately 300 meV at 600 °C. This term is, therefore, quite large at normal growth temperatures.

We would like to comment on the correction of Eq. (6) if the solid solution is not ideal. In that case, different arrangements of the atoms would have slightly different energies. Since the number of different arrangements of atoms (configurations) is very large, we may assume that it has a Gaussian energy distribution, with average μ and standard deviation σ , which depend on the composition. Now, it is rather straightforward to use this Gaussian distribution to obtain both μ and S as functions of temperature:

$$\mu(T) = \mu(T = \infty) - \frac{\sigma^2}{kT}, \quad (8)$$

and

$$S(T) = S_{\text{ideal}} - \frac{1}{2} k \left(\frac{\sigma}{kT} \right)^2, \quad (9)$$

where S_{ideal} is given by Eq. (6). It should be noted here that the expressions (8) and (9) should be viewed as asymptotic expansions, correct only in the limit of high temperature. Expressions such as Eqs. (8) and (9), as well as higher order terms, were given by Hildebrand and Scott.⁷ It should be noted that σ vanishes at the endpoints of the composition range ($x = 0$ or $x = 1$) and attains a maximum in between. At this maximum $\partial^2(\sigma^2)/\partial x^2 < 0$. Therefore, the correction to the free energy of mixing due to finite temperatures in Eqs. (8) and (9) has a positive curvature, thus enhancing mixing

TABLE I. Elastic constants times the volume of a formula unit for various III-V semiconductors (in units of eV). $C_{(100)}$ and $C_{(111)}$ were defined in Eq. (2). From this table it seems that a value of 100 eV has the right order of magnitude for the III-V semiconductors.

Material	$C_{(100)}$	$C_{(111)}$
GaP	74.9	103.7
InP	59.9	94.4
GaAs	69.6	97.6
InAs	53.2	83.5
AlSb	60.6	87.0
GaSb	62.0	86.5
InSb	53.7	82.5

rather than separation. The magnitude of these correction terms is usually small.⁷

The enthalpy of mixing term is the one that poses the main difficulty. It has to have a magnitude of more than a few tens of meV to dominate in temperatures of a typical crystal growth. The enthalpy of mixing in most ternary (pseudobinary) III-V alloys is usually approximated⁸ by regular solution theory:

$$\Delta H^m = \alpha x(1 - x), \quad (10)$$

where α is an interaction parameter. Experimental estimates of α in Eq. (10) for several III-V ternary systems are given by Panish and Ilegems.⁸ Various phenomenological models, using several unknown parameters, were used to obtain these values. The uncertainty in the accuracy of these parameters, therefore, is still unknown. Stringfellow⁹ has observed a scaling of α in Eq. (10) like the square of the mismatch in most III-V alloys. Martins and Zunger¹⁰ showed that such a scaling is expected on theoretical grounds from the strain component of ΔH^m . They have further showed that the chemical effects, due to charge transfer between bonds, do not scale with Δa^2 , but for random alloys this contribution is small.

We shall now discuss the contribution of the elastic strain in the film. The excess energy due to elastic strain in the film, induced by the substrate, is given by Eq. (3). To calculate this term, we have to know the elastic constants of the alloy for the whole composition range. Such a complete set of data has not been measured for any of the III-V ternary systems. We can, however, estimate the magnitude of this term.

We assume that the second derivative of $\frac{1}{2} C(x)x^2$ with respect to x is of the same order of magnitude as $C(x)$. This assumption is equivalent to assuming that there are no "spikes" in $C(x)$. To estimate this value, we present in Table I the relevant elastic constants, $C_{(100)}$ and $C_{(111)}$ for several binary III-V semiconductors. These elastic constants were calculated [using Eq. (2)] and later multiplied by the volume of a formula unit ($a^3/4$) to obtain the value of the elastic constants per formula unit. From Table I, it follows that $C(x)a^3/4$ is on the order of 100 eV per formula unit. Multiplying this value by the square of the strain, we obtain that the elastic strain contribution to the free energy is on the order of 0.1 meV per formula unit when the mismatch is 0.1%, 10 meV per formula unit when it is 1%, and up to 1 eV when the mismatch is 10%.

Only when the mismatch between the film and the substrate is on the order of several percent, the strain term is

Self diffusion of Ga in GaAs

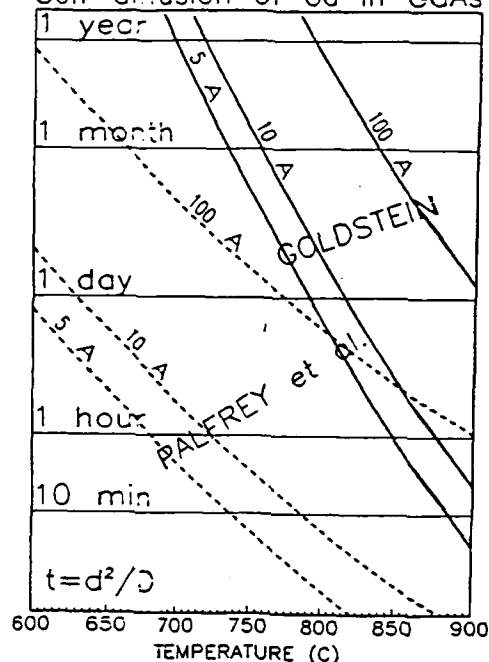


FIG. 1. Characteristic self-diffusion times of Ga in GaAs according to the experimental data of Goldstein (Ref. 13, solid lines) and Palfrey *et al.* (Ref. 14, dashed lines). The time required to diffuse over characteristic distances of 5, 10, and 100 Å is shown vs temperature.

appreciable (on the order of 10–100 meV). It may still be smaller than the entropy-of-mixing term, but when the entropy-of-mixing term is nearly balanced by the enthalpy of mixing, the strain can make the difference.

For a precise calculation, one has to know both the elastic constants of the film material as a function of composition and the thermodynamical data. At present, the elastic constants of the alloys have not been measured, and there is a lot of uncertainty about the thermodynamical functions of these alloys (see our discussion of $\text{Al}_x\text{Ga}_{1-x}\text{As}$, which is one of the best characterized alloys, in the following section). We, therefore, cannot hope at this moment to make any definite statements, only to point at some alloy systems that could prove to be interesting.

We are interested in systems that have a large mismatch (1%–10%), and a large, positive enthalpy of mixing. Among the ternary III-V systems, these two properties are correlated⁹ since the chemical contribution to the enthalpy of mixing is usually small for random alloys.¹¹ The four ternary III-V systems that include InSb are of particular interest, since they all satisfy the large mismatch condition. In addition, In(As, Sb) is a candidate for strained layer superlattices with small band gaps that may be used as IR materials.¹²

IV. $\text{Al}_x\text{Ga}_{1-x}\text{As}$ on GaAs

In this section we estimate the relevant parameters for the $\text{Al}_x\text{Ga}_{1-x}\text{As}$ on GaAs interface. Since the experimental data is incomplete, we have to estimate several parameters based on theoretical considerations.

A. Kinetics

Knowing the kinetics of the system could help clarifying

whether the clustering in $\text{Al}_x\text{Ga}_{1-x}\text{As}$ is stable or metastable. Unfortunately, only partial self-diffusion data are available for the $\text{Al}_x\text{Ga}_{1-x}\text{As}$ system, and they are mainly high temperature data. In Fig. 1, we show characteristic times for self diffusion of Ga in GaAs vs temperature. There are two sets of curves in Fig. 1, corresponding to diffusion data of Goldstein¹³ and of Palfrey *et al.*¹⁴ In each set there are three

curves, corresponding to diffusion over characteristic distances of 5, 10, and 100 Å. The relation between diffusion distance (d) and diffusion time (t) was calculated according to

$$t = d^2/D, \quad (11)$$

where the diffusion coefficient D is given by

$$D = D_0 \exp \left[\frac{-Q}{kT} \right], \quad \begin{array}{l} D_0 = 1 \times 10^7 \text{ cm}^2 \text{ s}^{-1}, \quad Q = 5.6 \text{ eV, (Goldstein}^{13}) \\ D_0 = 3.9 \times 10^{-5} \text{ cm}^2 \text{ s}^{-1}, \quad Q = 2.6 \text{ eV, (Palfrey } et al.^{14}). \end{array} \quad (12)$$

(The discrepancy between the two sets of data was attributed by Palfrey *et al.* to the difference in As overpressure during growth.) One can easily see in Fig. 1, that nonequilibrium features as narrow as 5 Å would require about a day of anneal at 800 °C to dissipate, if we take Goldstein's data as representing the actual diffusion rates. This would imply that the features as large as those observed by Petroff *et al.*³ do not have enough time to equilibrate. On the other hand, if Palfrey's data represent the actual diffusion rates, then at 800 °C it will take only few minutes to establish quasiequilibrium on a 5 Å scale and several hours to establish quasiequilibrium on a 100 Å scale. In that case the features observed by Petroff *et al.* could be formed spontaneously from a uniform alloy if they are more stable.

The large discrepancy between the two sets of self-diffusion data, as well as lack of self-diffusion data of $\text{Al}_x\text{Ga}_{1-x}\text{As}$, does not enable us to determine whether thermal equilibrium was established based on annealing time. We, therefore, have to determine if the clustered alloy is more stable than the uniform alloy, based on energy considerations.

B. Thermodynamics

In our treatment we would like to use the ideal-solution expression for the entropy of mixing. Recent experimental¹⁵ and theoretical¹¹ papers have questioned the ideality of $\text{Al}_x\text{Ga}_{1-x}\text{As}$ as grown at the 600–800 °C range. We may have to correct the entropy of mixing to account for nonideality, but it was shown in the previous section that such a correction, at least to first order in $1/T$, would enhance mixing rather than separation. Assuming that the $\text{Al}_x\text{Ga}_{1-x}\text{As}$ solid is an ideal solution,¹⁶ the entropy of mixing was given in Eq. (6). The entropy contribution to the second derivative of the free energy is at least $4NkT$, which is 300 meV per formula unit at 600 °C. We will show that it is almost an order of magnitude larger (in absolute value) than the contributions of the enthalpy of mixing, hence, dominating the mixing properties of $\text{Al}_x\text{Ga}_{1-x}\text{As}$ above 600 °C.

The enthalpy of mixing of random $\text{Al}_x\text{Ga}_{1-x}\text{As}$ has been estimated to be zero, or very close to zero. These estimates were, however, based on high-temperature measurements. Foster *et al.*¹⁶ have investigated the solidus line of the $\text{Al}_x\text{Ga}_{1-x}\text{As}$ system and concluded that this system is ideal [i.e., $\alpha = 0$ in Eq. (10)]. Stringfellow⁹ also concluded that $\alpha = 0$ in the $\text{Al}_x\text{Ga}_{1-x}\text{As}$ system. Other figures quoted in the literature are $\alpha = -500 \text{ cal/mol}^8$ at 1000 °C, $\alpha = +400 \text{ cal/mol}^1$ at 700 °C, and $\alpha = -3892 + 4T \text{ cal/mol}^1$ for $1073 \text{ K} < T < 1273 \text{ K}$. (1 kcal/mol = 43.3 meV/

formula unit). The experimental figures, therefore, are somewhere in the range

$$|\alpha| = < 25 \text{ meV/formula unit}, \quad (13)$$

and were obtained by fitting the phase diagram of $\text{Al}_x\text{Ga}_{1-x}\text{As}$. To obtain yet another estimate of α , we have performed *ab initio* self-consistent calculations on $\text{As}(\text{Ga}, \text{Al})_4\text{H}_{12}^{3-}$ clusters. Our calculations (to be described below) give an estimate of α which is included in the experimental range given in Eq. (13) in the separating region ($\alpha > 0$), but extends beyond the experimental range in the mixing region ($\alpha < 0$).

Our calculations were performed as follows. Self-consistent generalized-valence-bond¹⁷ formalism was used to calculate the total energy of $\text{AsGa}_4\text{H}_{12}^{3-}$, $\text{AsGa}_2\text{Al}_2\text{H}_{12}^{3-}$, and $\text{AsAl}_4\text{H}_{12}^{3-}$ clusters. The quasichemical interaction was calculated according to

$$\Omega = E_{\text{AsGa}_2\text{Al}_2} - \frac{E_{\text{AsGa}_4} + E_{\text{AsAl}_4}}{2}. \quad (14)$$

In Eq. (14), $E_{\text{AsGa}_2\text{Al}_2}$ is the total energy of the $\text{AsGa}_2\text{Al}_2\text{H}_{12}^{3-}$ cluster, etc.

All the clusters in our calculations consisted of a central arsenic atom surrounded by a shell of four cations (either gallium or aluminium atoms), which was in turn surrounded by a shell of 12 hydrogen atoms. The hydrogen atoms were used to terminate the dangling bonds of the cations. The angles between the bonds formed by each atom and its nearest neighbors were kept tetrahedral (109.47°) throughout the calculation. The clusters had a net charge of 3- to ensure covalent bonding similar to that in the crystal. The aluminium, gallium, and arsenic atoms were represented by a double- ζ basis set, containing s - and p -like wave functions. The hydrogen atoms were represented by a single, s -like wave function (a minimal basis set). The distances between the hydrogen atoms and their neighbor cation atoms were kept at a prescribed value of $d_m = 2.35 \text{ Å}$, rather than at the optimal distance, and the hydrogenic wave functions were inflated by a factor of $r_H = 2.5$. These two parameters, r_H and d_m , were used to control the electronegativity of the hydrogenic shell¹⁸ (that was used to mimic the bulk $\text{Al}_x\text{Ga}_{1-x}\text{As}$).

The value of Ω in Eq. (14) depends on the individual Ga-As and Al-As bond lengths. In Fig. 2 we show the total energy of the $\text{AsGa}_2\text{Al}_2\text{H}_{12}$ cluster (dashed curves) and Ω of Eq. (14) (continuous curves) as contour maps in the plane of Ga-As vs Al-As bond lengths. One can observe in Fig. 2 that a value of

$$-0.020 < \Omega < +0.004 \text{ eV} \quad (15)$$

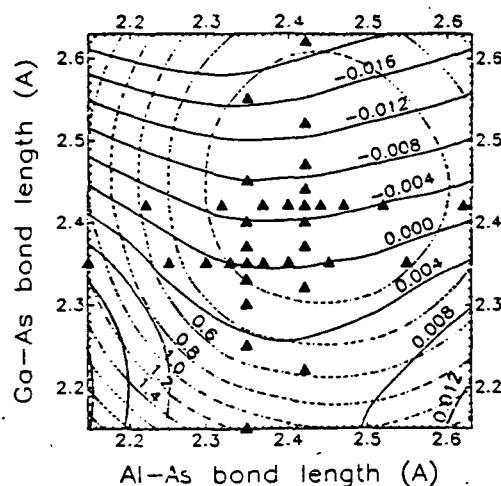


FIG. 2. Total energy of the $\text{AsAl}_2\text{Ga}_2\text{H}_{12}^-$ cluster (dashed lines), and the quasichemical interactions, (Ω) (solid lines) as a function of the Ga-As and Al-As bond lengths. The interaction parameter Ω was calculated using Eq. (14). It is acting toward phase separation when positive and toward phase mixing or compound formation when negative. Its value is rather small for all reasonable values of the bond lengths, in good agreement with Eq. (13). Solid triangles represent the values that were actually calculated (using generalized valence bond method). The values between the triangles were interpolated.

is obtained for all reasonable values of the Ga-As and Al-As distance. The Ω calculated in Eq. (14) include all the bonds between one anion and its neighboring cations. The relation between Ω in Eq. (14) and α in Eq. (10), was calculated using the quasichemical model.⁷ We assume that the contribution to the excess enthalpy of mixing is given by Ω from each arsenic atom that is bonded to two gallium and two aluminum atoms; $\Omega/2$ from each arsenic atom that is bonded to one cation of one kind, and three of the other kind, and 0 from each arsenic atom that is bonded to four cations of the same kind. If we further assume that all the configurations of cations are equally probable [$T = \infty$ in Eq. (8)], then the enthalpy of mixing per formula unit for the random alloy is given by

$$\begin{aligned} \Delta H^m &= \binom{4}{0} x^4 \cdot 0 + \binom{4}{1} x^3(1-x) \frac{\Omega}{2} + \binom{4}{2} x^2(1-x)^2 \Omega \\ &+ \binom{4}{3} x(1-x)^3 \frac{\Omega}{2} + \binom{4}{4} (1-x)x^4 \cdot 0 \\ &= 2\Omega \cdot x(1-x)(1+x-x^2). \end{aligned} \quad (16)$$

The polynomial $(1+x-x^2)$ varies between 1 and 1.25 in the range $0 < x < 1$. Therefore, by comparing Eqs. (16) to (10), it follows that α ranges between 2 and 2.5 Ω , using this model. Therefore, our calculations yield a value of α in the range $-50 < \alpha < +10$ meV per formula unit. This estimate is included in the experimental estimate given in Eq. (13) in the separating ($\alpha > 0$) range, but extends it somewhat in the mixing ($\alpha < 0$) range.

We now take the second derivative of the enthalpy of mixing in Eq. (10) with respect to the concentration x to obtain a value of -2α per formula unit, which is more than -50 meV per formula unit, using both our calculations and the experimental data. This is almost an order of magnitude

smaller than the 300 meV contributed by the entropy of mixing. Our calculations, therefore, suggest that there is no miscibility gap in the $\text{Al}_x\text{Ga}_{1-x}\text{As}$.

We would also like to comment here about the formation of an ordered compound ($\text{Al}_{0.5}\text{Ga}_{0.5}\text{As}$) as was reported recently by Kuan *et al.*¹⁵ Such a compound will be thermodynamically stable if the gain in enthalpy of mixing more than offsets the loss in entropy of mixing. According to the quasichemical model described above, the enthalpy of mixing of such an ordered compound is Ω per formula unit, compared to $\frac{1}{2}\Omega$ of the random alloy of the same composition. [$\frac{1}{2}\Omega$ is the value of Eq. (16) at $x = \frac{1}{2}$]. The gain in enthalpy of mixing is, therefore, $\frac{1}{2}\Omega$ per formula unit, according to this model. The entropy of mixing of the compound vanishes due to the ordering, while the entropy of mixing of the alloy equals $-k \log \frac{1}{2}$, representing a free energy loss of about $0.7kT$, which is approximately 50 meV per formula unit at 600 °C, compared to enthalpy gain of $\frac{1}{2}\Omega$ which is at most 7.5 meV according to our calculations. Srivastva *et al.*¹¹ have suggested that charge transfer from the weaker Ga-As bonds to the stronger Al-As bonds may result in a negative enthalpy of mixing, which in turn results in compound formation at low temperatures. Our calculation of Ω described above agree with the sign of the enthalpy suggested by Srivastva *et al.*, but the critical temperature required for such compound formation is, according to our calculations, much lower than 600 °C. Our calculations, therefore, suggest that the ordered structure observed by Kuan *et al.*¹⁵ may not be the equilibrium state of $\text{Al}_x\text{Ga}_{1-x}\text{As}$.

Finally, the elastic constants of $\text{Al}_x\text{Ga}_{1-x}\text{As}$ as a function of x have not been measured experimentally. Fortunately, the strain in an $\text{Al}_x\text{Ga}_{1-x}\text{As}$ film grown on GaAs is so small that we can easily establish the fact that the strain contributes less than 1 meV/formula unit to the total free energy. The difference in lattice parameters between GaAs and AlAs is extensively documented in the literature. Ettenberg and Paff¹⁹ showed that the mismatch varies between 0.14% at room temperature, to 0.0% at approximately 950 °C. We can, therefore, assume that above 600 °C,

$$\left(\frac{\Delta a}{a}\right)^2 < 10^{-6}. \quad (17)$$

The contribution of the strain for such a small mismatch was estimated in the previous section to be on the order of 0.1 meV per formula unit. Even if we allow an order of magnitude error in the estimate of the second derivative of $C(x) \cdot x^2$, the contribution of the strain is still at most 1 meV. Such a small contribution cannot affect the miscibility properties, unless the enthalpy of mixing and the entropy-of-mixing terms exactly cancel. This was shown not to be the case.

V. SUMMARY AND CONCLUSIONS

In this paper we have investigated the effect of substrate-induced strain on the miscibility properties of an epitaxial film consisting of an alloy. This investigation was motivated by the observed alloy clustering in $\text{Al}_x\text{Ga}_{1-x}\text{As}$ grown epitaxially on GaAs. We have shown that in some cases the miscibility properties of the film can be reversed by the strain induced by the substrate. A miscibility gap could be opened

in the film even if no such gap exists in the bulk alloy, and conversely, a miscibility gap in the bulk alloy could be closed by the strain.

The substrate-induced strain in the film is small for alloys that are closely matched to the substrate. For a mismatch of 0.1%, for example, we have estimated the strain effect to be only a fraction of a meV per atom (in the case of III-V ternary alloys). For a larger mismatch, say 1%, the contribution to the free energy is on the order of 10 meV/molecule. This contribution is still too small to offset the entropy of mixing at typical epitaxial growth temperatures. In cases in which the entropy of mixing is nearly balanced by the enthalpy of mixing, however, the strain term could tip the balance. We have suggested that this effect may be important in strained layer superlattices based on In(As, Sb). Since strained-layer superlattices are grown at relatively low temperatures, miscibility gaps may be present in In(As, Sb) alloys. It would be of great technological interest to find whether the strain can lower the critical temperature of the miscibility gap, or alternatively, enhance directional phase separation. Currently, lack of elastic data regarding these alloys as well as uncertainty about the thermodynamical data prohibit any serious attempt to calculate these effects.

We have also investigated the $\text{Al}_x\text{Ga}_{1-x}\text{As}$ on GaAs system. In that case we have concluded that the strain is too small to affect the miscibility. Since clustering was observed in this system, and we concluded that strain effects could not have caused it, we have examined the thermodynamical data in more detail. We have performed *ab initio* calculations of the enthalpy of mixing $\text{Al}_x\text{Ga}_{1-x}\text{As}$ and concluded that $\partial^2 H_m / \partial x^2$ is about an order of magnitude smaller than $\partial^2 TS_m / \partial x^2$ at the normal growth temperature ($T > 600^\circ\text{C}$). Our calculations are supported by the experimental data of Foster *et al.*¹⁶ which indicate that the $\text{Al}_x\text{Ga}_{1-x}\text{As}$ system behaves as a nearly ideal solution. In light of this big difference between the contributions of the enthalpy and entropy of mixing, the very small additional term due to strain cannot open a miscibility gap. It seems likely, therefore, that the uniform random alloy is the most stable state of the $\text{Al}_x\text{Ga}_{1-x}\text{As}$ system at temperatures above 600°C . We attribute the fact that clustering was observed in that system to

the slow kinetics at $600\text{--}800^\circ\text{C}$.

ACKNOWLEDGMENTS

The authors gratefully acknowledge the support of the Office of Naval Research under Contract No. N-00014-84-K-0501. Discussions with P. Petroff of Bell Laboratories and T. S. Kuan of IBM T. J. Watson Research Center were very helpful in clarifying the experimental situation. We would also like to acknowledge useful discussions with W. L. Johnson and A. Zunger.

- ¹H. C. Casey, Jr. and M. B. Panish, *Heterostructure Lasers* (Academic, New York, 1978).
- ²N. Holonyak, Jr., W. D. Laidig, B. A. Vojak, K. Hess, J. J. Coleman, P. D. Dapkus, and J. Bardem, *Phys. Rev. Lett.* **45**, 1703 (1980).
- ³P. M. Petroff, A. Y. Cho, F. K. Reinhart, A. C. Gossard, and W. Wiegmann, *Phys. Rev. Lett.* **48**, 170 (1982).
- ⁴N. A. Goryunova, F. P. Kesamanly, and D. N. Nasledov, in *Semiconductors and Semimetals, Vol. 4*, Physics of III-V Compounds, edited by R. K. Willardson and A. C. Beer (Academic, New York, 1968), p. 416.
- ⁵S. K. Maximov, *Phys. Status Solidi A* **83**, 685 (1984).
- ⁶J. H. van der Merwe and C. A. B. Ball, in *Epitaxial Growth, Part B*, edited by J. W. Matthews (Academic, New York, 1975), Chap. 6.
- ⁷J. H. Hildebrand and R. L. Scott, *The Solubility of Nonelectrolytes* (Reinhold, New York, 1950), p. 146.
- ⁸M. B. Panish and M. Legems, *Progress in Solid State Chemistry*, edited by H. Reiss and J. O. McCaldin (Pergamon, New York, 1972), Vol. 7.
- ⁹G. B. Strinifellow, *J. Phys. Chem. Solids* **34**, 1749 (1973).
- ¹⁰J. L. Martins and A. Zunger, *Phys. Rev. B* **30**, 6217 (1984).
- ¹¹G. P. Srivastava, J. L. Martins, and A. Zunger, *Phys. Rev. B* **31**, 2561 (1985).
- ¹²G. C. Osbourn, *J. Vac. Sci. Technol. B* **2**, 176 (1984).
- ¹³B. Goldstein, *Phys. Rev.* **121**, 1305 (1961).
- ¹⁴H. D. Palfrey, M. Brown, and A. F. W. Willoughby, *J. Electrochem. Soc.* **128**, 2224 (1981).
- ¹⁵T. S. Kuan, T. F. Kueh, W. I. Wang, and E. L. Wilkie, *Phys. Rev. Lett.* **54**, 201 (1985).
- ¹⁶L. M. Foster, J. E. Scardefield, and J. F. Woods, *J. Electrochem. Soc.* **119**, 765 (1972).
- ¹⁷F. W. Bobrowicz and W. A. Goddard, III, in *Modern Theoretical Chemistry: Methods of Electronic Structure Theory*, edited by H. F. Schaefer III (Plenum, New York, 1977), Vol. III, p. 79.
- ¹⁸A. Redondo, W. A. Goddard, III, C. A. Swarts, and T. C. McGill, *J. Vac. Sci. Technol.* **19**, 498 (1981).
- ¹⁹M. Ettenberg and R. I. Paff, *J. Appl. Phys.* **41**, 3926 (1970).

APPENDIX 8

Growth of superconducting V_3Si on Si by molecular beam epitaxial techniques

E. T. Croke, R. J. Hauenstein,^{a)} and T. C. McGill
California Institute of Technology, Pasadena, California 91125

(Received 26 April 1988; accepted for publication 6 June 1988)

Superconducting thin films (500–1000 Å in thickness) of $A 15 V_3Si$ have been grown on (111)Si substrates through molecular beam epitaxial techniques. V and Si are codeposited in a feedback-stabilized, 3:1 flux ratio from dual *e*-beam evaporators onto clean, heated Si substrates in an ultrahigh vacuum chamber. For the first time, the superconducting $A 15 V_3Si$ phase is metastably fabricated directly on a crystalline Si substrate without the formation of thermodynamically favored Si-rich V_xSi_y phases. Our films exhibit superconductivity only within a narrow range of intermediate growth temperatures (centered near 400 °C), with an optimum T_c of 12.5 K. X-ray diffraction shows the superconducting films to be polycrystalline $A 15 V_3Si$. For slightly higher growth temperatures (≈ 530 °C), Auger profile, x-ray, and transmission electron microscopy measurements indicate the appearance of an intermediate layer of roughly 1:1 V:Si composition. Our observations demonstrate that a growth temperature near 400 °C results in successful nucleation of the superconducting $A 15$ phase while minimizing solid phase reaction with the substrate during V_3Si growth.

Materials which crystallize in the $A 15$ structure have long been of interest for their superconducting properties. Recently, one of these $A 15$ materials, V_3Si , has been shown to exhibit a close geometrical lattice match to (111)Si.¹ The lattice match between V_3Si and Si is shown in Fig. 1. There we see that the (1×1) surface unit cell of (111) V_3Si coincides in size almost exactly ($< 0.4\%$) with a $(\sqrt{3} \times \sqrt{3})R 30^\circ$ surface cell of (111)Si.² The nature of the chemical bonds at such an interface appears favorable to epitaxy, although a significant amount of reconstruction may be necessary. This lattice match, along with the recent advances in Si molecular beam epitaxy (MBE) which have made possible the fabrication of epitaxial, single-crystal metal³ (NiSi₂ and CoSi₂) and insulating⁴ (CaF₂) films on Si, invites the possibility of growth of multilayered device structures based on various combinations of epitaxial superconductors, semiconductors, normal metals, and insulators, on Si.

Unfortunately, it has previously been impossible to stabilize growth of V_3Si films directly on crystalline Si. Studies have shown that the thermodynamics^{5–8} and (in some cases) kinetics⁶ instead favor the formation of the most Si-rich vanadium silicide phase, VSi₂, on a crystalline Si substrate. In particular, the V-Si phase diagram contains several V_xSi_y compounds, none of which exhibits superconductivity except V_3Si , the most V-rich (and in the presence of excess Si, the least stable) phase.⁹ This previous work was based on solid phase reaction (SPR) of thin V films with Si substrates^{5,8} and also on SPR of sequentially deposited Si-V diffusion couples onto SiO₂ or Al₂O₃ substrates.^{6,7}

In this letter, we report the first successful fabrication of superconducting V_3Si films directly on a crystalline Si substrate. Our V_3Si films were fabricated by molecular beam codeposition of V and Si (3:1 flux ratio) directly onto heated substrates in an ultrahigh vacuum (UHV) chamber. Growth temperatures significantly lower than those re-

quired for SPR silicide formation^{5–8} were used, thereby avoiding the problem of reaction with the substrate while retaining sufficient surface mobilities to allow formation of the $A 15$ structure. For an appropriate choice of growth parameters, our V_3Si films consistently exhibit superconductivity with T_c 's as high as 12.5 K with sharp transitions ($\Delta T_c \approx 0.2$ K). While all the films studied here proved to be polycrystalline, we believe that this work takes the first step toward achieving an epitaxial superconductor on Si.

The thin films studied here were grown in a custom-built UHV system specifically designed for silicide growth.¹⁰ Silicon and a transition metal (in this case, V) are codeposited at a predetermined flux ratio from dual *e*-beam sources onto heated substrates. A tungsten heater filament is used to

V_3Si -Si Lattice Match

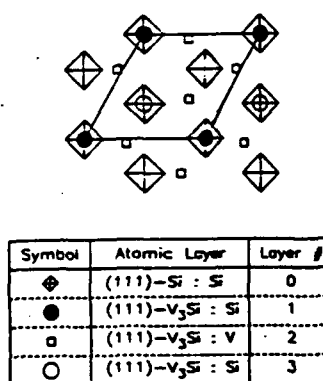


FIG. 1. Illustration of the lattice match between (111) V_3Si and (111)Si structures. For clarity, only one atomic layer of the Si and three of the V_3Si are shown. The fundamental surface unit cell of V_3Si is almost exactly the same size as the $(\sqrt{3} \times \sqrt{3})R 30^\circ$ surface cell on (111)Si. However, since only 1/3 of the Si atoms lie under the Si atoms in V_3Si (corners of the rhombus), there are three translationally equivalent lattice matches and, for each of these, a pair of 180° rotation twins, making a total of six possible epitaxial matches of V_3Si to a given (111)Si surface.

^{a)} Present address: Hughes Research Laboratories, Malibu, CA 90265.

radiatively heat the substrate. Substrate temperatures were calibrated to the heater power level through observation of Au/Si and Al/Si eutectics, giving reasonably accurate temperature-power level correlation in the range 363–577 °C.

Nominally, 500–1000 Å films consisting of a 3:1 ratio of V:Si were codeposited on (111)Si and (1102)Al₂O₃ substrates at a rate of 2.6 Å/s. The fluxes from the dual *e*-beam sources were closed-loop controlled using two quartz crystal sensors and monitors (Inficon model XTC) working in parallel. A 3:1 V:Si flux ratio was calculated to result from a 2.07:1 V:Si deposition rate ratio. Our growth rate for V₃Si of 2.6 Å/s was calculated assuming that the V and Si deposition rates were 2.1 and 1.0 Å/s, respectively. Prior to deposition, Si and Al₂O₃ substrates were degreased in trichloroethylene, acetone, methanol, and de-ionized water. Si substrates were dipped in a 50% by volume solution of HF and de-ionized water in order to remove the oxide layer. The substrates were outgassed at approximately 750 °C, and Si substrates were also exposed to a 0.5 Å/s Si flux in order to assist in the removal of the oxide^{11,12} and to ensure an atomically clean Si starting surface. Depositions were made in a low-hydrocarbon UHV environment with a base pressure of 8×10^{-11} Torr and with typical pressures during growth of approximately 5×10^{-9} Torr (dominated by H₂). Following each codeposition sequence, the substrate was immediately allowed to cool in order to minimize the amount of time that the films were held at elevated temperature.

Our films were codeposited on Si substrates at temperatures between room temperature and approximately 600 °C. For comparison, similar codepositions were also carried out on "inert" Al₂O₃ substrates. The films grown at room temperature appear mirror smooth, yet show no evidence of superconductivity on either substrate. Depositions made on Al₂O₃ at higher temperatures also appear mirror smooth and show increasing *T_c* approaching bulk values for V₃Si (≈ 17 K). Films grown on Si at temperatures in excess of 550 °C have a cloudy appearance and show no evidence of superconductivity. Growths on Si at lower temperatures have surfaces that appear mirror smooth and have superconducting transition temperatures closer to 10 K. Figure 2 shows the ρ vs *T* profile for our highest *T_c* sample on Si. This film was grown at approximately 400 °C to a final thickness of 1000 Å. The data indicate that the sample undergoes a superconducting transition at *T_c* = 12.5 K with a transition width of about 0.2 K. A more detailed presentation of the effect of the growth conditions on the resultant material and electrical properties of vanadium silicide films on Si and Al₂O₃ will be given elsewhere.¹³

Seemann-Bohlin x-ray diffraction measurements on two similar, 500-Å-thick superconducting samples, one grown at 400 °C and the other grown at 530 °C, indicate in both cases the presence of a polycrystalline film of *A*15, V₃Si. This is confirmed by cross-sectional transmission electron microscopy (TEM) measurements which reveal a columnar polycrystalline grain structure with a grain size of approximately 100–200 Å. Composition versus depth information for these two samples was obtained with the use of Auger sputter depth profiling. Figure 3(a) shows the composition profile for the sample grown at 400 °C. As can be seen from

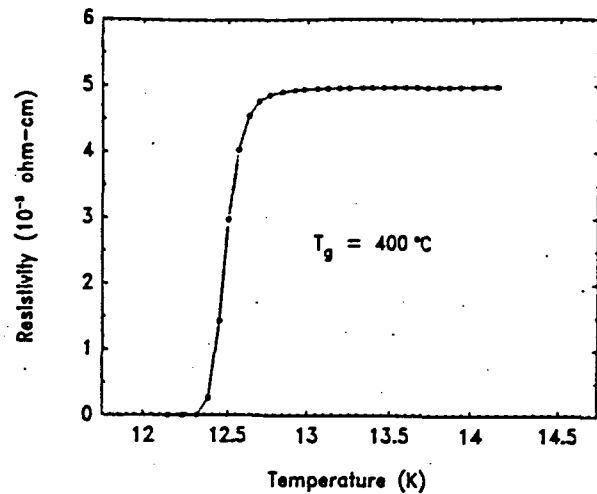


FIG. 2. Resistivity vs temperature data for a superconducting V₃Si film on (111)Si. The film shown becomes superconducting at *T_c* = 12.5 K, with a transition width (10%–90%) of approximately 0.2 K. Resistivity was measured using the van der Pauw method and calculated assuming a film thickness of 1000 Å.

the figure, the compositional profile of the film consists of a single V₃Si layer on Si, despite a somewhat broad interface. Assuming the V₃Si film thickness to be 500 Å, we estimate the interface width, after taking instrumental resolution into account, to be approximately 140 Å. In contrast, Fig. 3(b) shows the compositional profile of the sample grown at

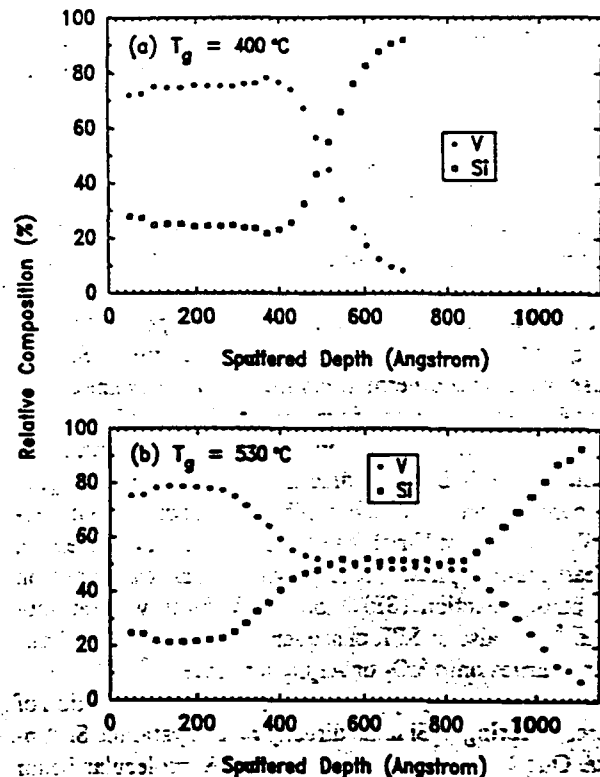


FIG. 3. Auger compositional profiles for two V₃Si films, each nominally 500 Å in thickness. The films were grown at (a) 400 °C and (b) approximately 530 °C. Compositional calibration is achieved by defining the film in (a) to be accurately V₃Si. The broad interfaces result primarily from interfacial roughness (~ 100 Å) in these samples.

slightly higher temperature (530 °C). If we take the composition of the top layer to be V_3Si , as suggested by our x-ray and electrical measurements, we see the formation of an intermediate layer having a V:Si composition of approximately 1:1. This intermediate layer is evidently due to a solid phase reaction between the depositing V_3Si film and the Si substrate. It is interesting to note that no "VSi" compound is present in the V-Si binary phase diagram,⁹ and while a V_6Si_5 phase does occur, this phase is not stable below 1160 °C. Hence the chemical identity of the intermediate layer is unclear at present, though it conceivably could be metastable V_6Si_5 .

The intermediate layer is also clearly evident in cross-sectional TEM images, which reveal that the boundaries between it and the substrate on one side and the V_3Si overlayer on the other are quite rough (~ 100 Å). This interfacial roughness (rather than interdiffusion) is probably the origin of the broad interfacial transitions observed in the Auger profiles shown in Fig. 3. Thus, from the above results, we see that a growth temperature of 400 °C minimizes the reaction with the substrate, yet ensures nucleation of the superconducting $A15$ V_3Si phase on Si.

In summary, with the use of modern molecular beam epitaxial growth techniques and through a careful choice of growth conditions, we have successfully fabricated the metastable $A15$ V_3Si phase on a crystalline Si substrate. Our study demonstrates that the $A15$ V_3Si structure will nucleate at unusually low temperatures during molecular beam co-deposition onto a clean, heated substrate. Too low a growth temperature results in the failure to form the superconducting $A15$ structure, while growth at higher temperatures results in a reaction between the depositing film and the Si substrate. Although we have not yet been able to achieve epitaxy, the results obtained here suggest that the appropriate growth template coupled with the appropriate substrate surface preparation may result in epitaxial growth of (111) V_3Si on (111)Si in the future.

The authors gratefully acknowledge C. W. Nieh for performing the TEM studies, P. J. Ireland for making the Auger profile measurements, K. Miller for obtaining the x-ray diffraction data, and H. V. Rudolph for assistance with the ρ vs T measurements. Also, we wish to thank O. J. Marsh and A. T. Hunter for valuable discussions and assistance. Finally, the authors wish to acknowledge the partial support of the Defense Advanced Research Projects Agency monitored by the Office of Naval Research under contract No. N00014-84-C-0083 and the Office of Naval Research under contract No. N00014-84-K-0501.

¹A. Zur, T. C. McGill, and M.-A. Nicolet, *J. Appl. Phys.* **57**, 600 (1985).

²A more detailed discussion of the possibilities for a (111) V_3Si /(111)Si lattice match are given in E. T. Croke, R. J. Hauenstein, C. W. Nieh, and T. C. McGill, to be presented at the Electronic Materials Conference, Boulder, CO, 22-24 June 1988.

³R. T. Tung, J. M. Gibson, and J. M. Poate, *Appl. Phys. Lett.* **42**, 888 (1983).

⁴R. W. Fathauer and L. J. Schowalter, *Appl. Phys. Lett.* **45**, 519 (1984).

⁵H. Kräutle, M.-A. Nicolet, and J. W. Mayer, *J. Appl. Phys.* **45**, 3304 (1974).

⁶R. J. Schutz and L. R. Testardi, *J. Appl. Phys.* **50**, 5773 (1979).

⁷P. A. Psaras, M. Eizenberg, and K. N. Tu, *Mater. Res. Soc. Symp. Proc.* **37**, 585 (1985).

⁸K. N. Tu, J. F. Ziegler, and C. J. Kircher, *Appl. Phys. Lett.* **23**, 493 (1973).

⁹Thaddeus B. Massalski, Joanne L. Murray, Lawrence H. Bennett, and Hugh Baker, eds., *Binary Alloy Phase Diagrams*, (American Society for Metals, Metals Park, 1986), Vol. 2, p. 2061.

¹⁰R. J. Hauenstein, Ph.D. thesis, California Institute of Technology, 1987.

¹¹M. Tabe, *Jpn. J. Appl. Phys.* **21**, 534 (1982); K. Kugimiya, Y. Hirofuji, and N. Matsuo, *ibid.* **24**, 564 (1985).

¹²C. F. Huang, R. P. G. Karunasiri, K. L. Wang, and T. W. Kang, in *Proceedings of the 2nd International Symposium on Silicon Molecular Beam Epitaxy*, edited by John C. Bean and Leo J. Schowalter (The Electrochemical Society, Pennington, 1988), p. 501.

¹³E. T. Croke, R. J. Hauenstein, C. W. Nieh, and T. C. McGill, to be presented at the Electronic Materials Conference, Boulder, CO, 22-24 June 1988.

APPENDIX 9

Growth and Characterization of Superconducting V_3Si on Si and Al_2O_3 by Molecular Beam Epitaxial Techniques

E. T. CROKE, R. J. HAUSTEIN,* C. W. NIEH and T. C. MCGILL

California Institute of Technology
Pasadena, California 91125

A study of the growth parameters governing the nucleation of metastable superconducting $Al_{15}V_3Si$ on Si and Al_2O_3 is presented. Nominally, 500Å films of $V_{1-x}Si_x$ were produced through codeposition of V and Si onto heated (111) Si and (1102) Al_2O_3 substrates. Samples were prepared in a custom-built ultrahigh vacuum (UHV) chamber containing dual e -beam evaporation sources and a high temperature substrate heater. V and Si fluxes were adjusted to result in the desired average film composition. $V_{0.75}Si_{0.25}$ films prepared at temperatures in excess of 550° C on Si show significant reaction with the substrate and are nonsuperconducting while similar films grown on Al_2O_3 exhibit superconducting transition temperatures (T_c) approaching bulk values for V_3Si (16.6–17.1 K). Codeposition at temperatures between 350 and 550° C results in superconducting films on Si substrates while growth at lower temperatures results in nonsuperconducting films. Lowering the growth temperature to 400° C has been shown through *ex situ* transmission electron microscopy (TEM) and Auger compositional profiling to minimize the reaction with the Si substrate while still activating the surface migration processes needed to nucleate $Al_{15}V_3Si$. Variation of film composition about $x = 0.25$ is shown to result in nonsuperconducting films for high x and superconducting films with T_c approaching the bulk V value (5.4 K) for low x . Finally, lowering the $V_{0.75}Si_{0.25}$ deposition rate is shown to raise T_c .

Key words: Silicide, superconductor, V_3Si , codeposition, epitaxy, UHV, MBE

I. INTRODUCTION

Recently, much excitement has been generated in the scientific community due to the discovery of materials which exhibit high superconducting transition temperatures. It is now well known that these materials possess a highly layered structure resembling, to a certain extent, a superconductor/insulator superlattice. Our work with the V_3Si/Si system¹ has been motivated by the possibility of fabricating such a structure and, perhaps, gaining control over the structural considerations governing T_c in the new superconductors. In addition, superconductor/semiconductor epitaxial structures may be of considerable interest in novel electronic device applications.

Besides being a simple binary system, V_3Si/Si also has been shown to have a very close lattice match on the (111) surface. Successful epitaxial growth of V_3Si on Si would greatly enhance the chances of growing layered superconductor/semiconductor structures. Zur *et al.*² have shown that (111) V_3Si matches to (111) Si to better than 0.4%; however, the two-dimensional unit cell size on the (111) Si surface is relatively large (three times the area of the fundamental unit cell) since the edges of the cell connect second nearest neighbor atoms as opposed to first nearest neighbors. As a result, the question of whether or not V_3Si can be grown epitaxially on Si is important from both a physical as well as a technological point of view.

Unfortunately, previous work on solid phase reaction (SPR) of V-Si diffusion couples^{3,4} and SPR of thin V films on Si substrates^{5,6} has demonstrated that V_3Si is unstable on crystalline Si as samples have a tendency to react further, resulting in growth of the nonsuperconducting phase, VSi_2 . In view of these results, our experiments have included the use of Al_2O_3 substrates in addition to Si substrates since we can safely assume that the depositing $V_{1-x}Si_x$ film will not react with the Al_2O_3 .

In this paper, molecular beam epitaxial (MBE) growth techniques were used to produce superconducting $Al_{15}V_3Si$ films directly on a crystalline Si substrate. Simultaneous growth on Si and Al_2O_3 substrates at temperatures in excess of 550° C result in nonsuperconducting films on Si while the corresponding films on Al_2O_3 exhibit superconductivity with T_c approaching the bulk value for V_3Si (16.6–17.1 K⁷). Further analysis of the growth temperature dependence of T_c for depositions on Si indicate the presence of a plateau region of superconductivity between 350 and 550° C. Auger compositional profiling and transmission electron microscopy (TEM) have been used to characterize the quality of the films and identify the superconducting material. Studies of the dependence of T_c on Si concentration, x , reveal that a maximum occurs near $x = 0.25$. In addition, for high x , films prepared on Si are nonsuperconducting and for low x , T_c approaches the bulk value for pure V (5.4 K). Finally, decreasing the growth rate is shown to result in improved film quality and the highest T_c observed for a 500Å V_3Si film on Si (13.5 K).

*Permanent Address: Hughes Research Laboratories, Malibu, CA 90265.

(Received May 1, 1989; revised August 14, 1989)

II. EXPERIMENTAL

The samples prepared for this study were codeposited from a Thermionics dual *e*-beam source in a custom-built ultrahigh vacuum (UHV) chamber with a base pressure $< 8 \times 10^{-11}$ Torr and typical growth pressures of approximately 5×10^{-9} Torr. The growth system has been adequately described elsewhere.⁸ Two Inficon (model XTC) controllers were independently used to maintain closed-loop control over the V and Si deposition rates. Rates were calibrated using a Tencor Instruments alpha-step 200 stylus profiler. Nominally, 1000Å V or Si were deposited on Al₂O₃ substrates and the thicknesses were measured at four different spots on the wafer. The spread in the measurements indicated an uncertainty of about 5 percent in the final thicknesses. The deposition rate ratio, r_v/r_{Si} , was calculated from the expression

$$\frac{r_v}{r_{Si}} = \frac{1 - x}{x} \frac{\rho_{Si} M_V}{\rho_V M_{Si}} \quad (1)$$

where x is the molar fraction in $V_{1-x}Si_x$, ρ_{Si} and ρ_V are the densities, and M_{Si} and M_V are the molecular weights of Si and V, respectively. For $x = 0.25$ (the Si concentration appropriate for V₃Si growth), the ratio, $r_v/r_{Si} = 2.07$, was calculated from Eq. (1). This ratio changed, of course, when we varied the Si concentration in the depositing film. In practice, accurate rate control over a few angstroms was difficult to achieve, especially at low deposition rates since instantaneous rate fluctuations in the *e*-beam process could be as large as 0.3Å/sec; however, at the growth temperatures used in this study, the atoms have sufficient thermal energy to blur the effect of these fluctuations. As a result, we have chosen to calculate our compositions using the final thicknesses of the constituents in Eq. (1) instead of the rates. Propagating the uncertainty in the thicknesses through the calculation results in an uncertainty in average Si concentration of about 1%.

Depositions were made onto heated (111) Si and (1102) Al₂O₃ substrates which had been first degreased in trichloroethylene, acetone, methanol, and then rinsed in de-ionized water. After this degreasing procedure, the Si substrates were etched in a 50% HF solution to remove SiO₂, rinsed once again in de-ionized water, and immediately loaded into the UHV chamber. Samples prepared for the study of growth temperature versus T_c were outgassed *in situ* at approximately 800° C. Growth temperatures were calibrated through observation of Au/Si and Al/Si eutectic reactions *in situ*, and correlated to heater power levels, assuming a T^4 dependence. At the eutectic points, the calibration is exact, assuming the eutectic reactions occurred at the correct temperatures (363° C for Au/Si and 577° C for Al/Si). Still, we estimate our substrate temperature calibration to be accurate only to within 25° C. Other factors are also present which may affect actual substrate temperature. For instance, thermal drift due to heating of the substrate heater itself could cause

the wafer temperature to change during deposition. We have attempted to address these factors by carefully reproducing heater power levels and temperature ramping times from run to run.

Once we determined that we could consistently grow superconducting V₃Si on Si, we discontinued use of the Al₂O₃ substrates. The study of the effect of Si concentration on T_c used a modified substrate cleaning procedure and employed the growth of a 100Å Si buffer layer at approximately 760° C instead of the high temperature outgassing. Prior to growth of the samples used in the study of growth rate versus T_c , the substrates were heated to approximately 860° C and were exposed to a 0.1Å/sec Si flux for 30 sec.^{9,10} Subsequently, a 200Å Si buffer layer was grown at 760° C. Changes in substrate cleaning procedure were intended to improve the Si starting surface, with the objective of obtaining an atomically clean surface. At present, we do not have the capability of characterizing this surface *in situ* aside from visual inspection. Fortunately, subsequent TEM was able to show that most of the SiO₂ was indeed removed. The sample set described in this study is presented in Table I.

III. RESULTS AND DISCUSSION

Our initial attempts at growing V₃Si involved simultaneous deposition onto (111) Si and (1102) Al₂O₃ substrates which had been first outgassed *in situ* at approximately 800° C. V and Si were codeposited in

Table I. V_{1-x}Si_x/Si sample characteristics. Samples 1-9 were used in the study of T_c vs. T_g . The dependence of T_c on composition x was determined through a study of samples 5 and 10-13, and samples 14 and 15 were used to investigate the effect of deposition rate on T_c .

Sample ^a	Substrate(s)	Thickness (Å)	x (%Si)	T_g (°C)	T_c (K)
1(a)	(111) Si	5000	0.25	25	—
1(b)	(1102) Al ₂ O ₃	5000	0.25	25	—
2	(111) Si	500	0.25	305	—
3	(111) Si	500	0.25	350	8.4
4	(111) Si	500	0.25	380	9.8
5	(111) Si	500	0.25	400	9.8
6(a)	(111) Si	500	0.25	500	9.6
6(b)	(1102) Al ₂ O ₃	500	0.25	500	10.6
7(a)	(111) Si	500	0.25	530	9.9
7(b)	(1102) Al ₂ O ₃	500	0.25	530	9.8
8(a)	(111) Si	500	0.25	565	—
8(b)	(1102) Al ₂ O ₃	500	0.25	565	13.1
9(a)	(111) Si	525	0.25	640	—
9(b)	(1102) Al ₂ O ₃	525	0.25	640	14.6
10	(111) Si	500	0.20	400	5.4
11	(111) Si	500	0.22	400	7.0
12	(111) Si	500	0.27	400	11.1
13	(111) Si	500	0.30	400	—
14	(111) Si	500	0.25	400	12.2
15	(111) Si	500	0.25	400	13.5

^aSample pairs denoted by (a) and (b) involve simultaneous deposition onto Si and Al₂O₃ substrates.

a 3:1 flux ratio at various growth temperatures and T_c was measured with a germanium-diode thermometer while the sample was held over liquid He. Growth rates and final thicknesses were chosen to result in the growth of a 500Å V_3Si film at a rate of about 2.6Å/sec. Figure 1 shows the dependence of T_c on T_g observed in this study. Samples prepared at temperatures in excess of 550° C are non-superconducting on Si and have T_c approaching the bulk value for V_3Si (16.6–17.1 K) on Al_2O_3 substrates. (Presumably we might obtain a higher T_c on Al_2O_3 if we had chosen to investigate growth at higher temperatures. Higher growth temperature would give the depositing atoms more energy and freedom to nucleate larger grains. Our purpose here, however, is to study growth on Si.) Films grown on Si do not superconduct unless the growth temperature is between 350 and 550° C. Room temperature depositions do not superconduct on either substrate, presumably because the surface migration of the depositing atoms is insufficient to form the A15 structure. Therefore, we find a plateau region between 350 and 550° C where A15 V_3Si can be grown directly on a (111) Si substrate with T_c near 10 K.

Transmission electron diffraction (TED) and plan view TEM have confirmed the presence of polycrystalline A15 V_3Si in our samples. Figure 2(a) is a plan view TEM of a 500Å film grown at 400° C (sample 5). The polycrystalline nature of the surface layer is clearly evident in the image and the

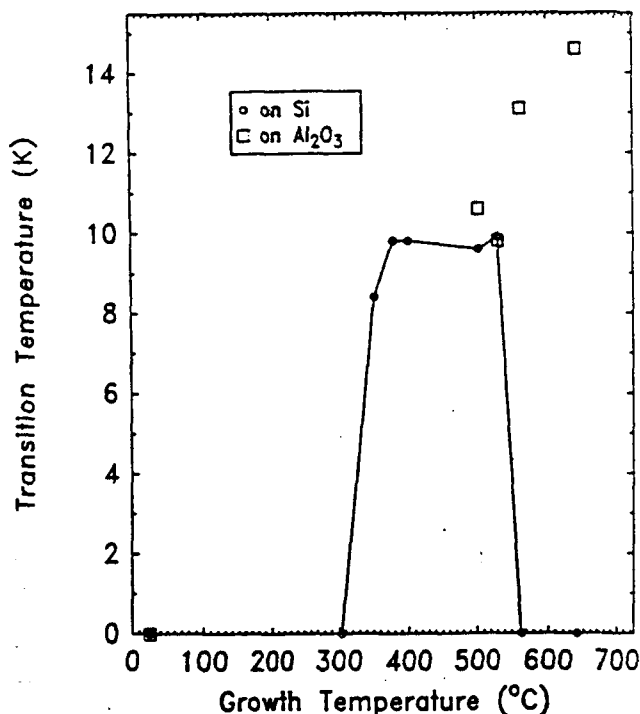
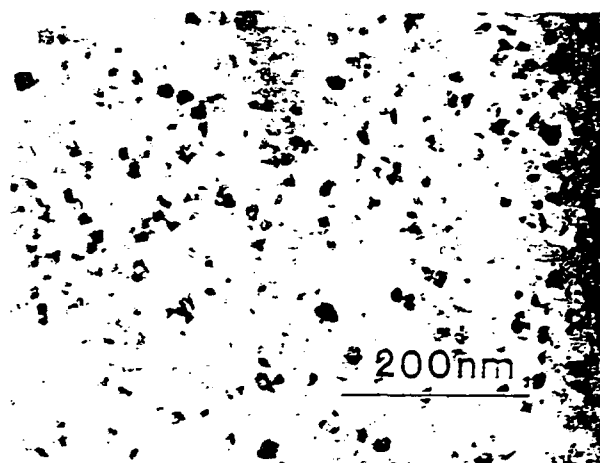
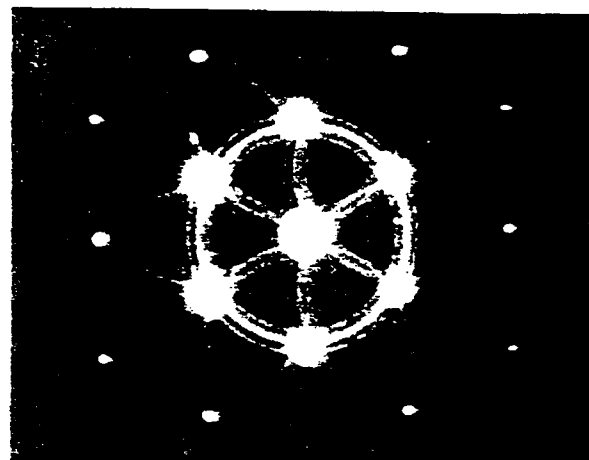


Fig. 1 — Results from T_c measurements on 500Å $V_{0.75}Si_{0.25}$ films grown on (111) Si and (1102) Al_2O_3 substrates. Samples grown on Al_2O_3 at high temperature have T_c approaching the bulk value for V_3Si (16.6–17.1 K). Growths on Si react considerably with the substrate at growth temperatures in excess of 550° C, yet, between 350 and 550° C, superconducting A15 V_3Si is nucleated with a T_c typically near 10 K. Films grown at room temperature do not superconduct on either substrate.



(a)



(b)

Fig. 2 — (a) Plan view TEM showing randomly oriented grains from a 500Å V_3Si film grown on (111) Si at 400° C (sample 5). The grain size is estimated to range between 100 and 200Å in the plane of the interface. (b) Transmission electron diffraction pattern along the (111) zone axis normal to the surface of the sample studied in (a). Rings surrounding the transmitted beam (central spot) were indexed and are due to polycrystalline A15 V_3Si . Rings surrounding diffraction spots due to the substrate result from multiple scattering from the film and the substrate.

grain diameter is estimated to range from 100–200Å. Further evidence of the presence of polycrystalline V_3Si is presented in Fig. 2(b). This image is the electron diffraction pattern from the sample analyzed for Fig. 2(a) with the electron beam aligned along the (111) zone axis normal to the surface. The rings surrounding the transmitted beam (central spot) have been indexed and are due to V_3Si . Multiple diffraction is responsible for the rings observed around the Si substrate diffraction spots. It is apparent from this pattern that the V_3Si grains are randomly oriented with respect to the substrate.

Two 500Å V_3Si samples grown on (111) Si (samples 5 and 7) were selected for further analysis using Auger compositional profiling. Calibration was achieved by defining the surface layer to be accurately V_3Si . The results are presented in Fig. 3. In

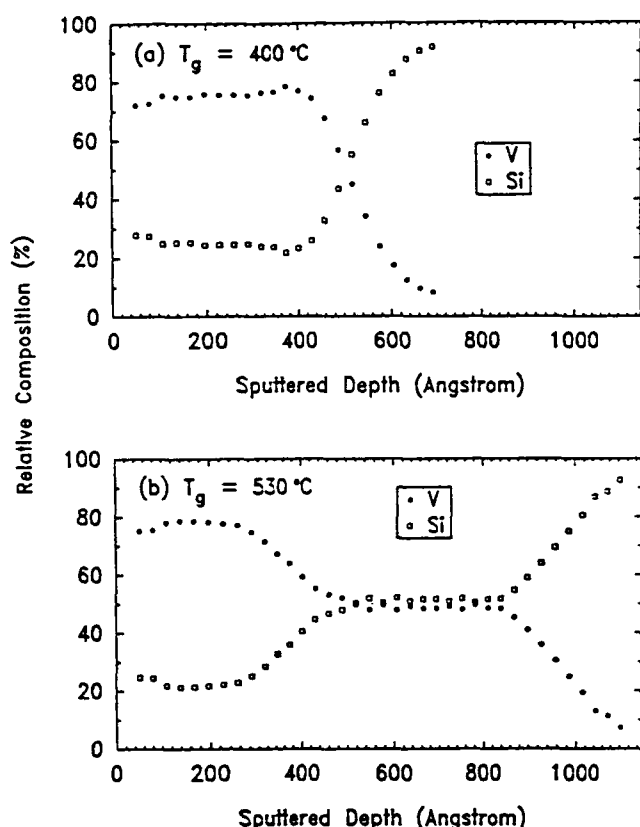


Fig. 3 — Auger compositional profiles from two nominally 500 Å V_3Si samples grown on (111) Si (samples 5 and 7(a)). (a) The sample grown at 400°C has a sharp interface with the Si substrate indicating that minimal reaction has taken place. The diffuse nature of the interface is due entirely to limitations associated with instrumental resolution. (b) A growth temperature of 530°C is shown to result in significant reaction with the substrate producing an intermediate layer with a 1:1 V:Si average composition.

Fig. 3(a), a film grown at 400°C is shown to be composed entirely of V_3Si . The diffuse nature of the interface with the Si substrate is due to instrumental broadening. Figure 3(b) suggests that significant reaction with the substrate has occurred for a sample grown at 530°C producing an intermediate layer composed of V and Si in a 1:1 average composition. It is interesting to note that the binary phase diagram¹¹ for the V-Si system does not include a "VSi" phase and that although a V_6Si_5 phase does exist, it is not stable below 1160°C . Unfortunately, a plan view TEM specimen was not prepared for this sample so it was not possible to identify the composition of this intermediate layer although it could conceivably be metastable V_6Si_5 .

Cross-sectional TEM was also performed on these samples and the results are presented in Fig. 4. In Fig. 4(a), the Si buffer layer and the polycrystalline V_3Si overlayer from the sample grown at 400°C are clearly visible. The buffer layer is indeed epitaxial despite the contrast present in the image. Unfortunately, it appears to contain a higher than desired density of extended defects (spaced by several thousand Å). However, since the V_3Si grain size is

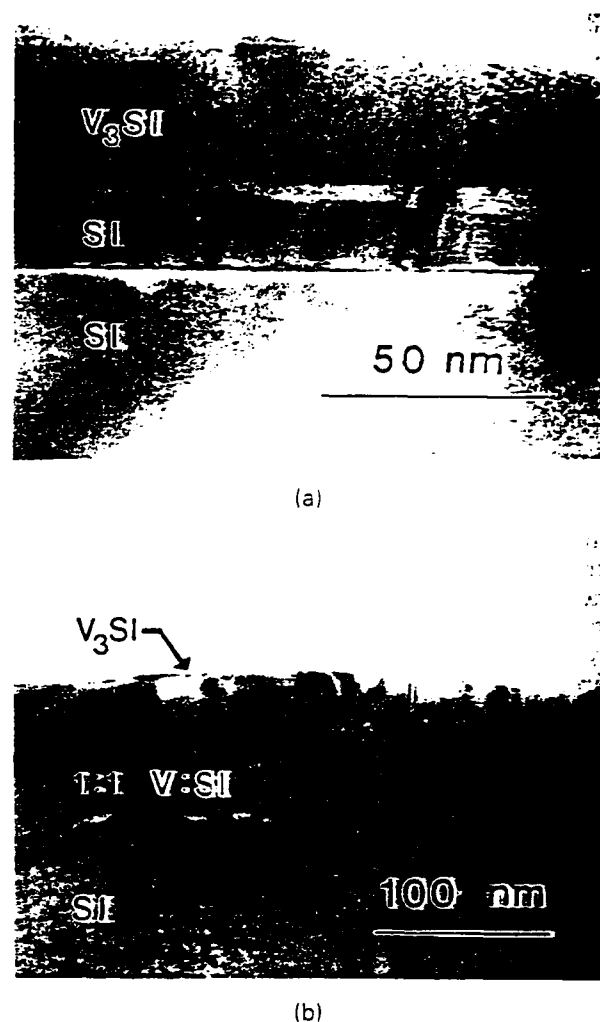


Fig. 4 — Cross-sectional TEM performed on the two samples described in Fig. 3. (a) A crystalline Si buffer layer and a polycrystalline V_3Si overlayer is shown to form a sharp interface in the sample grown at 400°C . (b) For a growth temperature of 530°C reaction with the Si substrate produced a polycrystalline intermediate layer. Grains appear to be columnar in both (a) and (b) with typical diameters ranging from 100–200 Å.

only about 100 Å, we can safely assume that buffer layer quality is not the limiting factor in our attempt to obtain epitaxial V_3Si . In addition, the image shows no evidence of reaction with the substrate since the interface appears very sharp. The 530°C sample shown in Fig. 4(b) has obviously reacted with the Si substrate. One can clearly distinguish two polycrystalline layers in this image, thereby corroborating the result presented in Fig. 3(b). The crystallites appear columnar in these images with typical grain diameters between 100 and 200 Å in agreement with our plan view image presented in Fig. 2(a). Therefore, we conclude that, by lowering the growth temperature to about 400°C , a polycrystalline, superconducting V_3Si film can be grown metastably directly on crystalline Si with minimal reaction with the substrate.

In addition to studying the dependence of T_c on growth temperature, we also investigated the effect

of film composition on T_c . Depositions were made at our previously determined optimal growth temperature of 400° C and deposition rates were modified to provide a V:Si flux ratio that varied from 4:1 to 7:3 (20% to 30% Si). Figure 5 shows that, for high V concentrations, T_c drops to about 5.4 K, the accepted value for pure V, suggesting that pure V has segregated out of the depositing layer. As the Si concentration is increased, we see a maximum in the T_c occurring near $x = 0.25$ as might be expected. For $x \geq 0.30$, samples are typically non-superconducting, indicating that a non-superconducting $V_{1-x}Si_x$ phase has segregated out of the Si-rich films in the same way that pure V segregated out of the V-rich films. So far, TEM specimens have not been prepared in order to verify this conclusion. This study has shown that a Si composition of approximately $x = 0.25$ results in the highest quality superconducting V_3Si material.

Several 500Å V_3Si samples have been grown at 400° C in an attempt to study the effect of growth rate on T_c but unfortunately have yielded somewhat inconclusive results. Since fluctuations in deposition rate become more significant at lower rates, it becomes increasingly difficult to maintain an exact 3:1 V:Si stoichiometric ratio. Deposition rates for V_3Si growth were varied between 2.6 and 0.8Å/sec. The first few growths at low V_3Si deposition rates have produced samples with higher T_c values. Our best sample shows a T_c of 13.5 K for a 500Å V_3Si film grown at 400° C with a deposition rate of

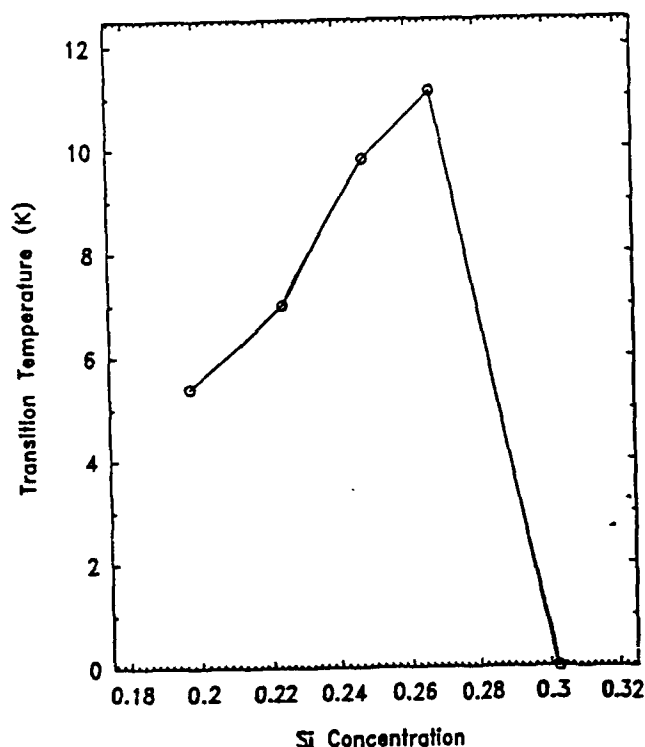


Fig. 5 — Effect of Si concentration, x , on T_c . As x is varied about the value, 0.25, T_c degrades considerably. For V-rich films, V segregates out and the T_c begins to approach the bulk V value (5.4 K). For Si-rich films, nonsuperconducting material segregates out, causing superconductivity to vanish for $x \geq 0.30$.

only about 0.8Å/sec. Although this result is encouraging, further work will be necessary if epitaxial V_3Si on Si is to be realized.

CONCLUSIONS

Through the use of modern molecular beam epitaxial growth techniques, superconducting V_3Si films have been successfully grown directly on a crystalline Si substrate. A study of the growth parameters governing nucleation of V_3Si on (111) Si has also been conducted. Growth temperature has been shown to strongly affect the nature of the deposited film. A temperature of 400° C seems to produce the highest quality V_3Si while minimizing reaction with the Si substrate. Additionally, for Si concentrations different from $x = 0.25$, T_c begins to degrade due to segregation of inferior materials from the Al5 V_3Si . Lowering the growth rate has been shown to increase T_c although strict stoichiometric control has been difficult to obtain. Finally, though our results have not yet indicated epitaxial growth, the use of more refined growth procedures may result in epitaxial (111) V_3Si on (111) Si in the near future.

ACKNOWLEDGMENTS

The authors gratefully acknowledge P. J. Ireland for making the Auger profile measurements. One of us, C. W. Nieh, would like to acknowledge support from the National Science Foundation under Materials Research Group grant No. DMR 8811795. Finally, the authors wish to acknowledge the partial support of the Defense Advanced Research Projects Agency monitored by the Office of Naval Research under Contract No. N00014-84-C-0083 and the Office of Naval Research under Contract No. N00014-84-K-0501.

REFERENCES

1. E. T. Croke, R. J. Hauenstein and T. C. McGill, *Appl. Phys. Lett.* **53**, 514 (1988).
2. A. Zur, T. C. McGill and M.-A. Nicolet, *J. Appl. Phys.* **57**, 600 (1985).
3. R. J. Schutz and L. R. Testardi, *J. Appl. Phys.* **50**, 5773 (1979).
4. P. A. Psaras, M. Eizenberg and K. N. Tu, *Mater. Res. Soc. Symp. Proc.* **37**, 585 (1985).
5. H. Kräutle, M.-A. Nicolet and J. W. Mayer, *J. Appl. Phys.* **45**, 3304 (1974).
6. K. N. Tu, J. F. Ziegler and C. J. Kircher, *Appl. Phys. Lett.* **23**, 493 (1973).
7. B. W. Roberts, *J. Phys. Chem. Ref. Data* **5**, 581 (1976).
8. R. J. Hauenstein, Ph.D. Thesis, California Institute of Technology, 1987.
9. M. Tabe, *Jpn. J. Appl. Phys.* **21**, 534 (1982); K. Kugimiya, Y. Hirofujii, and N. Matsuo, *ibid.* **24**, 564 (1985).
10. C. F. Huang, R. P. G. Karunasiri, K. L. Wang, and T. W. Kang, *Proc. of the 2nd International Symposium on Silicon Molecular Beam Epitaxy*, ed. by John C. Bean and Leo J. Schowalter (The Electrochemical Society, Pennington, 1988), p. 501.
11. *Binary Alloy Phase Diagrams*, ed. by Thaddeus B. Massalski, Joanne L. Murray, Lawrence H. Bennett, and Hugh Baker, Vol. 2 (American Society for Metals, Metals Park, 1986), p. 2061.